**Tropical Cyclone Intensity Analysis Using
Passive Microwave Imager and Sounder Data**

THESIS

David C. Moreno, Captain, USAF

AFIT-ENP-MS-15-M-093

**DEPARTMENT OF THE AIR FORCE
AIR UNIVERSITY**

# AIR FORCE INSTITUTE OF TECHNOLOGY

**Wright-Patterson Air Force Base, Ohio**

AFIT-ENP-MS-15-M-093

TROPICAL CYCLONE INTENSITY AND POSITION ANALYSIS USING

PASSIVE MICROWAVE IMAGER AND SOUNDER DATA

THESIS

Presented to the Faculty

Department of Engineering Physics

Graduate School of Engineering and Management

Air Force Institute of Technology

Air University

Air Education and Training Command

in Partial Fulfillment of the Requirements for the

Degree of Master of Science in Applied Physics

David C. Moreno, B.S.

Captain, USAF

March 13, 2015

AFIT-ENP-MS-15-M-093

TROPICAL CYCLONE INTENSITY AND POSITION ANALYSIS USING

PASSIVE MICROWAVE IMAGER AND SOUNDER DATA

THESIS

David C. Moreno, B.S.
Captain, USAF

Committee Membership:

Lt Col Robert S. Wacker, PhD
Chair

Lt Col Kevin S. Bartlett, PhD
Member

Christoph Borel-Donahue, PhD
Member

AFIT-ENP-MS-15-M-093

# Abstract

Satellite based Tropical Cyclone (TC) intensity estimates are critical for TC warning centers and global Numerical Weather Prediction (NWP) Models due to the lack of in-situ observations of mean sea-level pressure and TC winds. Passive microwave instruments on polar-orbiting weather satellites are useful for estimating the intensity of TCs because upwelling microwave radiation can generally penetrate clouds. The upwelling radiation is converted to brightness temperatures and used to measure the intensity of the TC's warm core, precipitation, and ice particle formation via the emitted radiation absorption and scattering signatures. Currently, operational TC prediction centers rely on intensity estimates derived from Polar-orbiting Operational Environmental Satellite (POES) Advanced Microwave Sounding Unit (AMSU-A) brightness temperatures. This study compares the performance of a variety of TC intensity estimation techniques using both the imaging and sounding channels from AMSU-A, the Defense Meteorological Satellite Program (DMSP) Special Sensor Microwave Imager and Sounder (SSMI/S), and the Suomi-National Polar-orbiting Partnership (S-NPP) Advanced Technology Microwave Sounder (ATMS) for a sample of 28 North Atlantic storms from the 2011 through 2013 TC seasons. Using a stepwise multivariate regression statistical model SSMI/S, AMSU, and ATMS achieve correlation coefficients of 0.89, 0.86, and 0.73 respectively with TC mean sea level pressure (MSLP), and root mean square error (RMSE) of 7.7, 9.3 and 12.8 mb, respectively.

# Acknowledgements

homework assignment less difficult and this thesis possible.

Finally, I dedicate this thesis to my parents; muchas gracias por todo lo que me han brindado en esta vida, especialmente por todos los sacrificios por los cuales hoy nos encontramos aqui. Sin su apoyo y motivacion esto no hubiera sido posible.

David C. Moreno

# Table of Contents

# List of Figures

# List of Tables

TROPICAL CYCLONE INTENSITY AND POSITION ANALYSIS USING

PASSIVE MICROWAVE IMAGER AND SOUNDER DATA

# I. Introduction

## 1.1 Motivation

Analysis of tropical cyclone (TC) position and intensity is inhibited by the lack of in-situ observations over the data-sparse tropical oceans. WC-130 aircraft from the Air Force Reserve's 53rd Weather Reconnaissance Squadron and P-3 aircraft from the National Oceanographic and Atmospheric Administration (NOAA) provide the main source of in-situ measurements of TC intensity, but these observations are not available in the Pacific Ocean or areas of the Atlantic Ocean outside the range of these aircraft. The lack of in-situ observations can be overcome by employing algorithms to estimate intensity and position using visible, infrared (IR), and microwave data from geostationary and polar-orbiting weather satellites.

The analysis of TCs via satellite instrumentation has grown in importance over the last four decades. Since the beginning of satellite meteorology no TC has gone undetected. Table 1 shows that during the period of 1995 to 2010 the average number of TCs increased compared to the average number of TCs from 1851 to 2010 (Blake et al. 2011). Despite this increase, there was a decrease in lives lost and an increase and improvement in preparedness and plans to mitigate infrastructure damage to coastal areas affected by TCs.

1

**Table 1. Average number of TC occurences at different storm categories over five different periods from 1851 to 2010. Data from (Blake et al. 2011).**

| PERIOD | Number of Years | Average number of Tropical Storms | Average number of Hurricanes | Average number of Major Hurricanes |
|---|---|---|---|---|
| 1851-2010 | 160 | 9.0 | 5.4 | 1.9 |
| 1944-2010 | 67 | 10.8 | 6.2 | 2.7 |
| 1966-2010 | 45 | 11.4 | 6.3 | 2.4 |
| 1981-2010 | 30 | 12.1 | 6.4 | 2.7 |
| 1995-2010 | 16 | 14.8 | 7.9 | 3.8 |

Meteorological satellites have helped this effort by providing forecasters with critical information about TC's intensity, location and track. Several methods have been developed to exploit satellite imagery to determine TC position and intensity remotely. However, these methods are subjective and suffer from biases introduced by the human analyst. More recently, data from microwave sounding instruments has enabled characterization of the thermodynamic structure of these storms, improving forecasts of intensification and future track.

The purpose of this research is to develop a TC intensity algorithm using passive microwave satellite instruments and compare performance between instruments to enhance the forecaster's confidence using the algorithm to analyze the intensity of TCs.

## 1.2 Microwave Imagers and Sounders

The microwave portion of the electromagnetic spectrum has proven to be very effective for analyzing TC position and intensity. Microwave imagery from the Defense Meteorological Satellite Program (DMSP) Special Sensor Microwave Imager/Sounder

(SSMI/S) and more recently the Suomi National Polar-orbiting Partnership (S-NPP) Advanced Technology Microwave Sensor (ATMS) are useful for determining TC position and structure because they can map spiral band precipitation through cloud cover via scattering or absorption of the upwelling microwave radiation. Microwave temperature sounder data from SSMI/S, ATMS and the Polar-orbiting Operational Environmental Satellite (POES) Advanced Microwave Sounding Unit (AMSU) are useful for estimating TC intensity via the warming in the upper troposphere above the storm center. Several algorithms have been developed to characterize this warm anomaly and show a correlation with the mean sea level pressure (MSLP).

## 1.3 Problem

In the North Atlantic and Eastern North Pacific basins, the National Hurricane Center (NHC) is responsible for issuing TC forecasts and warnings. The Joint Typhoon Warning Center (JTWC) is a joint Navy and Air Force command that provides TC reconnaissance, forecasting, and warnings to support US government agencies operating in the Western North Pacific and Indian Ocean basins (Air Force Weather Agency accessed 2014). Currently only AMSU sounding data is used operationally by JTWC to derive TC intensity estimates. However, the SSMI/S offers better spatial resolution and constant instrument field of view due to its conical scan geometry. The ATMS is a relatively new instrument that paves the way for future passive microwave instrumentation and will eventually replace NOAA's AMSU. Currently no TC intensity estimation techniques tailored for the strengths of the SSMI/S and ATMS are in operational use, so it is unknown how well these instruments perform in comparison with AMSU-based TC intensity estimation techniques. It may be possible to exploit ATMS and SSMI/S imagery channels, in addition to their sounder data, to aid in TC intensity estimation.

## 1.4 Objective

Several techniques, both objective and subjective, have been developed to characterize the intensity of TCs. The majority of these techniques use passive microwave radiometer data to exploit the capabilities of the AMSU sounding channels. While the AMSU is a practical instrument heavily used in research and operations, the SSMI/S offers better spatial resolution and constant field of view (FOV) geometry across its scanline. The ATMS, which was recently launched, represents the future of TC microwave remote sensing. The objective of this research is to develop a TC intensity algorithm tailored for the SSMI/S and ATMS and to objectively compare AMSU, SSMI/S, and ATMS TC intensity estimates.

This thesis contains five chapters: The introduction chapter presents the reader the problem and objective of this research. The background chapter is a literature review summarizing TC structure, microwave remote sensing, and existing satellite based microwave TC intensity algorithms. The methodology chapter discusses how the data were acquired and analyzed to accomplish the objective. Chapter four provides the reader with the analysis and results. The final chapter summarizes the results and elaborates on possible operational use and future work.

# II. Background

## 2.1 Tropical Cyclones

TCs are warm-core cyclonic circulations with extensive cumulus convection that develop within 30° latitude of the equator. These storms track with the mid-level atmospheric flow and are capable of sustained winds as high as 160 kt (1 kt = 0.51 m/s) and MSLP as low as 880 mb. TCs have the thermodynamic characteristics of a Carnot engine, converting the sensible and latent heat contained in the tropical ocean surface to the kinetic energy of the TC circulation. TC wind and pressure fields are usually in hydrostatic and gradient balance.

TC season in the Northern Hemisphere varies by ocean basin, but in general these systems develop during the summer months when the ocean surface temperature is above 26.5° - 27.0°C (Frank and Roundy 2006). In the Atlantic ocean, Hurricane season officially starts on June 1st, peaks in September and concludes at the end of November. In the Eastern Pacific, the season starts on May 15th, and ends at the same time as the Atlantic season. Over the Western Pacific, Typhoon season lasts year-round, peaking in late August and into September. The naming convention is different for the Atlantic and Western Pacific (WESTPAC): TCs that develop and reach 64 kt are called Hurricanes in the Atlantic and Eastern Pacific basins, but in the WESTPAC, these systems are called Typhoons. Table 2 shows TC classification by basin according to wind speed and MSLP.

**Table 2. TC classification by ocean basin. MSLP and the Saffir-Simpson wind scale are used in the Atlantic Basin, Eastern and Central Pacific**

| MSLP [mb] | Wind Speed [kt] | Atlantic Ocean, Central and East Pacific | Western Pacific |
|---|---|---|---|
| $\geq 1005$ | $\leq 33$ | Tropical depression | Tropical depression |
| 987-1005 | 34 - 63 | Tropical storm | Tropical storm |
| 975-987 | 64 - 82 | Cat 1 Hurricane | Typhoon |
| 965-975 | 83 - 95 | Cat 2 Hurricane | Typhoon |
| 950-965 | 96 - 112 | Cat 3 Hurricane | Typhoon |
| 925-950 | 113 - 136 | Cat 4 Hurricane | Typhoon |
| $\leq 925$ | $\geq 137$ | Cat 5 Hurricane | $\geq 130$ Super Typhoon |

Atlantic TCs generally develop from easterly waves exiting the African continent embedded in the Intertropical Convergence Zone (ITCZ). These disturbances can often organize and form a cluster of thunderstorms. Cyclonic low level relative vorticity and planetary vorticity can help the system organize and develop its own low level cyclonic circulation. If the system of thunderstorms is deep enough and a strong low level circulation is present, latent heat will become trapped in the center of the circulation creating the warm core characteristic of a TC. As the TC gains intensity and the convection wraps around the low level circulation, convective precipitation bands develop and spiral into the center of the storm, creating rainbands or feeder-bands in near-concentric rings. Heavy precipitation concentrates in these rings, where the convection is isolated from any moderate to strong mid to upper level wind shear. The convective updrafts in clouds forming the concentric rings are strong enough to lift water drops beyond the freezing level and produce ice particles in the upper troposphere. As the rainbands spread further from the center of the TC, low

level convergence decreases in magnitude and precipitation becomes more stratiform. The released latent heat induced by precipitation will lower the surface pressure and strengthen the winds at the perimeter of the low pressure system according to Hart (2006). Strengthening winds converging towards the center of the storm will enhance evaporation from the relatively warm ocean surface, moistening the low level environment. The relatively deep layer of warm ocean surface water induces a continuous sensible heat flux providing the thermal energy necessary for self-sustainment and further intensification and counteracting any cooling resulting from evaporation or convective downdrafts. Besides the presence of relatively deep warm ocean temperatures and relative cyclonic vorticity, weak winds and high relative humidity values are required in the mid to upper troposphere for the storm to maintain its strength and autonomy.

The presence of the warm core is imperative for the TC to sustain it self. Its presence allows TC researchers to make the comparison to a Carnot engine, which is a thermodynamic cycle that converts heat to mechanical energy in order to maintain a thermodynamic balance (Emanuel 1986). Thermodynamic disequilibrium develops between the relatively cool atmosphere and the warm ocean surface. With the ocean as a heat source, air-sea interaction brings the system closer to equilibrium. Wind spiraling into the center of the developed low pressure system advects sensible heat from the ocean surface. Air parcels then ascend moist adiabatically to high altitudes (15km) where some heat is lost via radiation to space. The cooled parcels then sink adiabatically far from the center of the TC and close the cycle by converging radially back into the storm, advecting in new sensible heat from the ocean surface (Emanuel 2003).

Figure 1 is a schematic of this Carnot cycle. The first branch of the system, wind is responsible for sensible heat transport (a to b), moist adiabatic ascent is represented in the second branch (b to c), radiative cooling from c to d, and adiabatic descent from d to a.
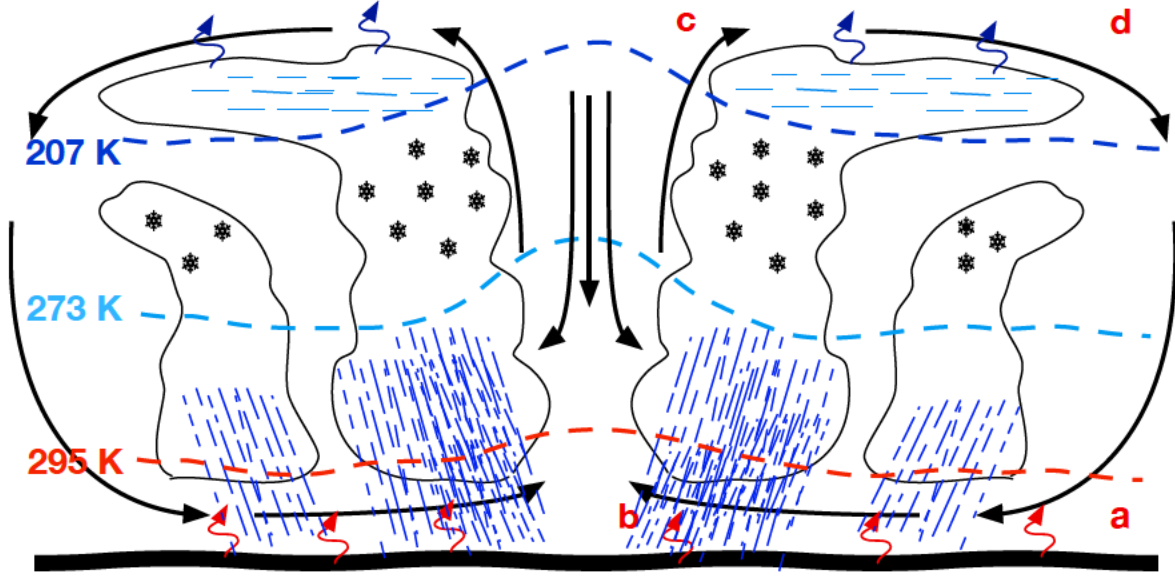


**Figure 1.** The four branches of the Carnot Cycle: Isothermal inflow near the surface draws and transports sensible latent heat from the ocean surface to the the TC core (a-b). Moist adiabatic ascent in the core of the TC and outflow in the upper troposphere (b-c). Air parcels cool down by radiating energy to space (c-d). Cooled air parcels sink adiabatically (d-a) and are assumed to return to the center of the storm to close the cycle.

Because the thermodynamic energy is proportional to the kinetic energy of the system, a relationship between MSLP and the wind speed can be approximated using the hydrostatic (1) and pressure gradient balance equations (7). The warm core of the TC, enhanced by subsidence in the eye of the storm and latent heat released, reduces the density of the air, lowering the heights of the isobaric layers.

$$\frac{dp}{dz} = -\rho g \tag{1}$$

Substituting the ideal gas law (2) and integrating the hydrostatic equation (1) through the depth of the troposphere using the mean temperature of the layer as shown in equation (3), the surface pressure can be computed (4).

$$p(z) = \rho(z)RT(z) \tag{2}$$

$$\int_{P_{bot}}^{P_{top}} \frac{dp}{p} = \frac{g}{R} \int_{Z_{sfc}}^{Z_{top}} \frac{dz}{T(z)} \tag{3}$$

$$p(z) = p_{top} \exp\left(\frac{gz_{top}}{R\overline{T}}\right) \tag{4}$$

Equation (4) then shows the relationship between the layer's mean temperature and the surface pressure of the column of air (Holton and Hakim 2012). In general, the pressure gradient increases as the temperature differential between the core of the storm and the environment increases. The drop of the MSLP at the center of the storm can be correlated to the intensity of the warm core anomaly. TC wind speed is strongly related to the pressure gradient of the TC as the system has to conserve angular momentum (5); cyclonic circulation decreases with radius (Emanuel 1986).

$$M = rV + \frac{1}{2}fr^2 \tag{5}$$

Here $r$ is the radial distance from the center of the storm, $V$ is the wind speed and $f$ is the Coriolis parameter. After algebraic manipulation and using the hydrostatic balance relation (1) to convert to radial coordinates using the geopotential height ($\phi$), the gradient balance equation (7) is resolved and can be used to estimate the wind speed using the radial change in pressure.

$$g\frac{dz}{dp} = \phi \tag{6}$$

$$V = -\frac{fr}{2} \pm \left(\frac{f^2r^2}{4} - r\frac{\partial\phi}{\partial r}\right)^{1/2} \tag{7}$$

The positive root of (7), ( $R > 0$ , $\frac{\partial\phi}{\partial r} < 0$ ), represents the flow around a regular low and is the balance between the Coriolis parameter, the centrifugal force and pressure gradient forces.

Characterizing the warm core has been a challenge because of the lack of in-situ observations. Using the infrared (IR) or microwave spectrum, satellite instruments can measure vertical temperature profiles by using different frequencies. The microwave portion of the electromagnetic spectrum has proven to quantify this feature better than at any other frequencies. In addition, passive microwave imagery of TCs is possible due to interaction of microwaves and precipitation.

## 2.2 Microwave Remote Sensing

At microwave wavelengths (millimeters), cloud droplets (with radii of approximately 10 $\mu$m) absorb and scatter very weakly. This makes clouds effectively transparent to passive microwave instruments. Rain drops (with radii between approximately 100 $\mu$m and 1 mm) are good absorbers at low and high microwave frequencies. Graupel and hail, often present in the upper parts of deep convective clouds, are strong scatterers at higher microwave frequencies. This makes microwave imagers operating between 19 and 91 GHz ideally suited for penetrating high cirrus to detect precipitation and ice particle concentration. Microwave sounders use the molecular oxygen absorption band between 50-70 GHz and the water vapor absorption band from 180 to 190 GHz to make temperature profiles and moisture profiles of the atmosphere.

The microwave portion of the electromagnetic radiation is comprised of two widely utilized atmospheric windows: one at low frequencies, 15-40 GHz, and one at higher frequencies range, 80-90 GHz. The oxygen absorption band is located between the two atmospheric windows and the strong water vapor absorption band resides on the high frequency edge of the spectrum. Figure 2 shows the atmospheric window and absorption bands in the microwave portion of the electromagnetic spectrum.
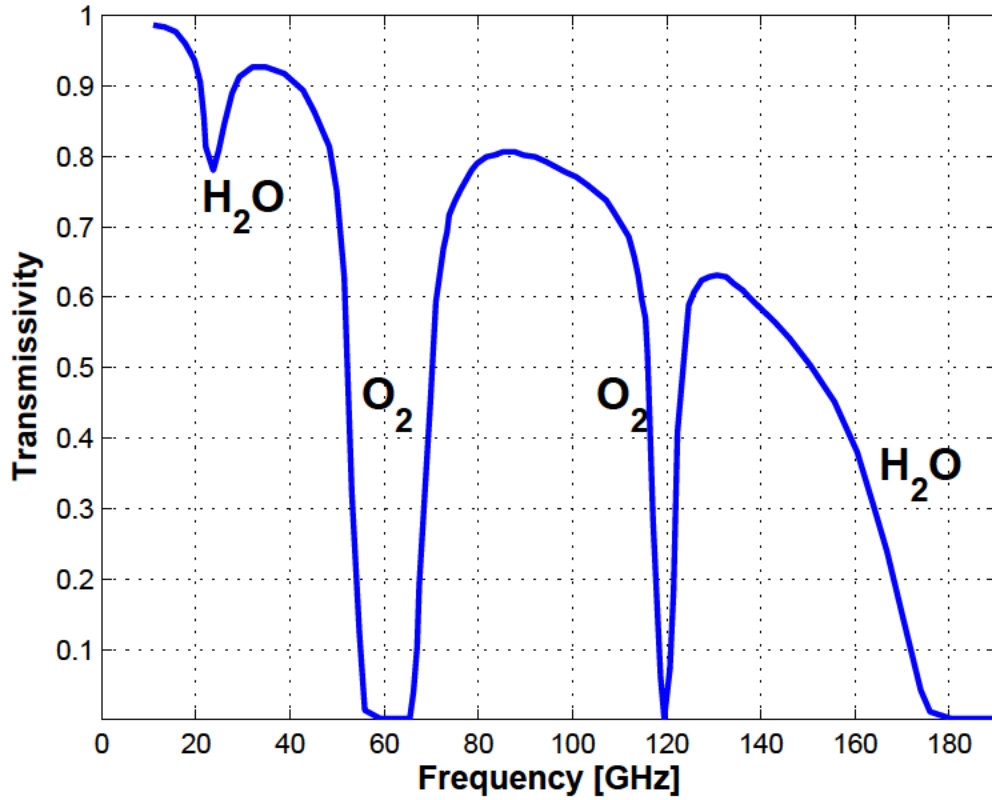


**Figure 2. Temperature and moisture soundings derived from passive microwave radiometers use the $O_2$ and $H_2O$ absorption bands. Imaging channels use channels in close proximity to the two atmospheric windows (15 - 40 GHz & 80 - 90 GHz). Adapted from Cooperative Institute for Research in the Atmosphere (accessed 2014).**

### 2.2.1 Remote Sensing Physics

Radiation emitted by atmospheric features can be classified by wavelength ($\lambda$), frequency ($\nu$), or energy. The electromagnetic (EM) spectrum is classified by how

energetic photons are. The energy a photon is equal to its frequency multiplied by Plank's constant ($h = 6.63\text{E-}34 \ Js$). Plank's Law describes the EM radiation emitted by a blackbody in thermal equilibrium. Equation 8 is obtained by integrating over all the frequencies emitted by the object of interest in thermal equilibrium with its environment.

$$B_\nu(T) = \frac{2h\nu^3}{c^2} \frac{1}{e^{\frac{h\nu}{k_B T}} - 1} \tag{8}$$

Where $B_\nu$ denotes the spectral radiance of the object in question as a function of $\nu$, its temperature $T$, and $k_B$=1.3806E-23 $m^2 kgs^{-2}K^{-1}$, the Boltzmann constant. In remote sensing the spectral radiance is given by the radiance counts measured by the satellite instrument. Taking the inverse of Plank's Law, one can solve for the blackbody's brightness temperature, given by

$$T_b = \frac{h\nu}{k_b} \ln^{-1}\left(1 + \frac{2h\nu^3}{B(\nu)c^2}\right) \tag{9}$$

In the limit of low frequencies, the brightness temperature of the blackbody can be described by Rayleigh-Jeans Law (10), an approximately linear relationship between the radiance and the brightness temperature of the object.

$$T = \frac{B_\nu(T)c^2}{2\nu^2 k_b} \tag{10}$$

In the microwave portion of the EM spectrum the brightness temperature of the object can be approximated by using the Rayleigh-Jeans Law (10).

Figure 3 shows the Rayleigh-Jeans law and Plank's law at different terrestrial temperatures; both curves equal each other at very low frequencies as shown in the graphic. Thus, in the limit of low frequencies, Plank's and Rayleigh-Jeans Law converge to a single brightness temperature for a given radiance value. This relationship allows for the radiance to be used as the blackbody's brightness temperature or vice versa.
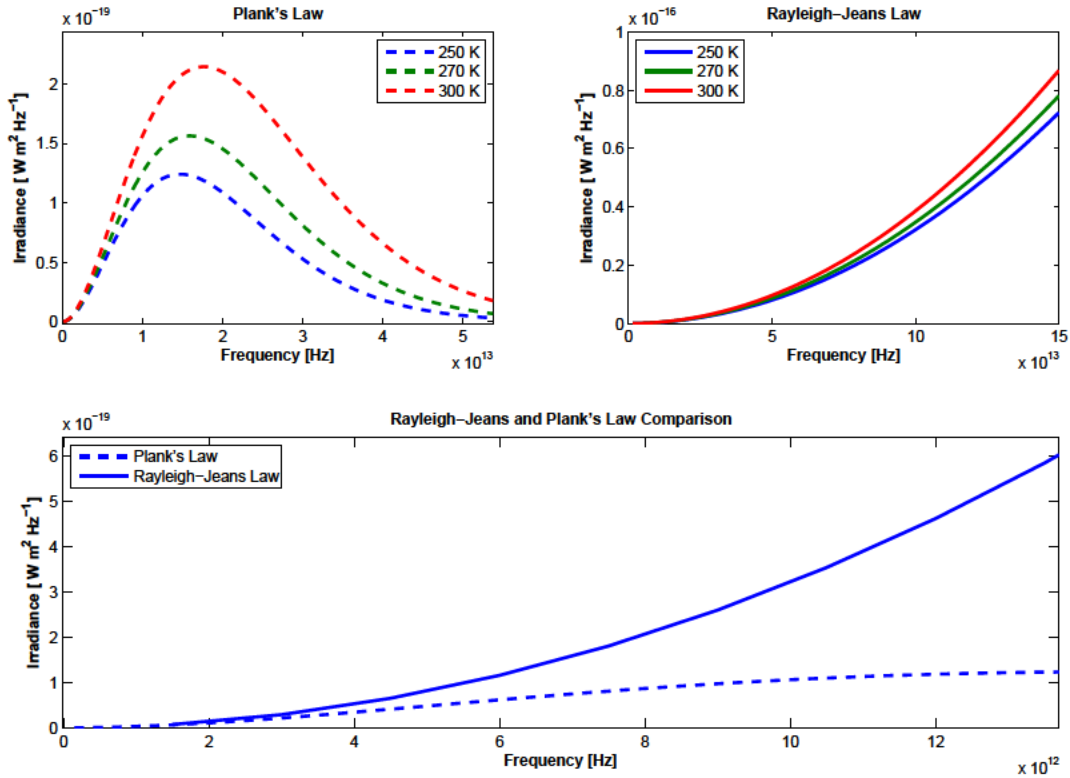


Figure 3. Top Left: Plank curves for three different temperatures; 300 , 270 and 250 K. Top Right: Rayleigh Jean's Law for 300, 270 and 250 K. Bottom: Comparison of Plank's Law to Rayleigh Jean's Law; at very low frequencies [GHz], the Rayleigh Jean's and the Plank curves converge. Radiances in the microwave range can be translated to brightness temperatures using the linear Rayleigh-Jean's Law approximation.

A blackbody is a theoretical perfect absorber and emitter. Emissivity ($\epsilon$) is the ratio of the body's actual temperature and the blackbody's brightness temperature. $T_B = T\epsilon$. The emissivity of the land surface in the microwave portion of the EM spectrum is approximately 0.9 and polarization independent. For water surfaces the

emissivity is highly dependent on the polarization of the radiation and its incidence angle. Figure 4 shows the emissivity for water at various microwave frequencies in the vertical and horizontal polarization. Water's emissivity increases with increasing frequency at nadir; off-nadir, emissivity decreases for horizontally polarized radiation and increases for vertically polarized radiation.
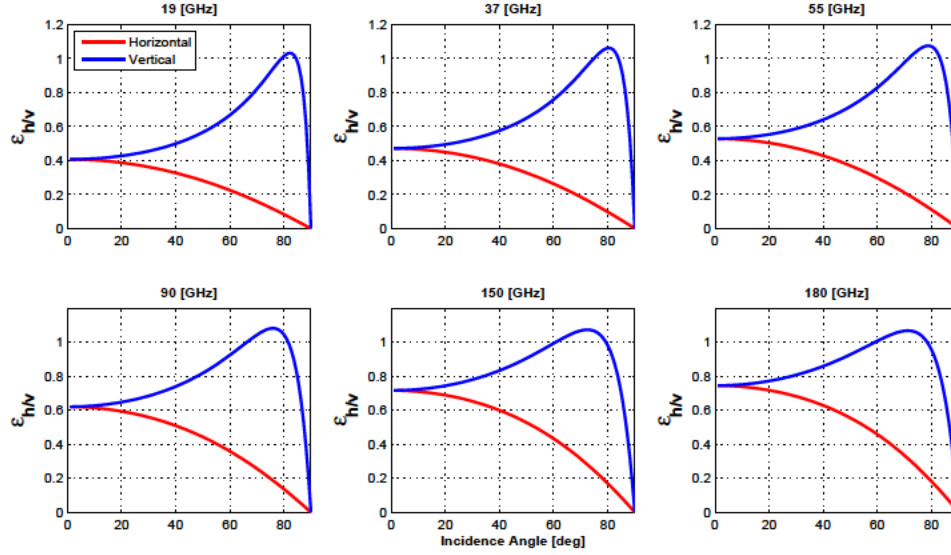


Figure 4. Water surface emissivity ($\epsilon$) at various microwave frequencies; for both **vertical** and **horizontal** polarization. At low frequencies water surface brightness temperature appears much colder than actual temperature due to the low emissivity. Higher frequencies have higher emissivity values. Note the emissivity also changes with respect to incidence angle and polarization.

Upwelling terrestrial radiation can be characterized using Beer's law; the intensity of the radiation decreases as the radiation travels through a medium that absorbs.

$$I_\nu(s_2) = I_\nu(s_1)e^{-\int_{s_1}^{s_2} \beta_a(s)ds} \tag{11}$$

$\beta_a$ is the absorption coefficient of the medium, which is dependent on the radiation frequency and the density of the medium. The medium in this case consists of the atmospheric constituents. The transmittance ($t$) of the radiation through a layer of the atmosphere is dependent on the optical path, $\tau$, which describes the magnitude

14

of attenuation in a layer of the atmosphere from $s_1$ to $s_2$. $\beta$ is distinctive for an atmosphere constituent and it obeys the superposition principle in the layer in question (Petty 2006).

$$\tau(s_1, s_2) = \int_{s_1}^{s_2} \beta_a(s)ds \tag{12}$$

$$t = e^{-\frac{\tau(s_1, s_2)}{\mu}} \tag{13}$$

Transmittance is dependent on the incidence angle $\theta$, the radiation's angle with respect to the vertical plane. We define $\mu = cos(\theta)$. Radiation not transmitted is absorbed; and by Kirchhoff's law, absorptivity ($\alpha$) is equal to emissivity. Under local thermodynamic equilibrium (LTE) the microwave emission of the layer is basically proportional to the temperature of the layer.

$$\epsilon = \alpha \tag{14}$$

The Radiative Transfer model uses Beer's law and Plank's law under LTE conditions to characterize the absorptivity, transmissivity, and emissivity of the medium. A solution to the radiative transfer model for the total radiance sensed from the top of the atmosphere (TOA) is given by the following equation.

$$I_{TOA}(\mu, \infty) = \epsilon B(T_{sfc})t^{\frac{1}{\mu}} + (1 - \epsilon)B(T_{space})t^{\frac{2}{\mu}} + \int_0^{\infty} W^{\uparrow}(z, \mu)B(T)dz \tag{15}$$

I($\mu, \infty$) describes the sum of the upwelling surface radiation after attenuation by the atmosphere constituents and the thermal contribution of each of the atmospheric layers above the surface, weighted by the upwelling weighting function $W^\uparrow(z, \mu)$ at a given frequency.

$$W(z, \mu) = \left[ 1 + (1 - \epsilon_{sfc}) \left( \frac{t_{sfc}}{t} \right)^{\frac{2}{\mu}} \right] \frac{d}{dz} \left( t^{\frac{1}{\mu}} \right) \qquad (16)$$

The weighting function W(z,$\mu$), quantifies the contribution of radiation emitted from given layer of the atmosphere at a specific frequency by measuring the transmissivity's rate of change with respect to height (Petty 2006). In general a frequency's weighting function provides a reference height to the layer providing most of the radiation to the sensor.

Equation (16) is solved for each of the instrument's channels. After the weighting function at each frequency is computed, the radiance measured by the sensor can be translated into a brightness temperature (Rayleigh-Jeans Law) corresponding to a layer in the atmosphere where the weighting function peaks. Contribution from other layers or atmosphere constituents can affect the brightness temperature sensed, especially for channels that are highly susceptible to absorption or scattering when deep convective precipitation is present in the general vicinity of where the weighting function peaks.

Figure 5 shows the AMSU weighting function for channel 7 (54.9 GHz) for both nadir and edge of scan (48.8 °) FOVs. The temperature at 11 km is best represented by the channel 7 brightness temperature. Also note the dependency on the incidence angle $\mu$. At nadir the weighting function peaks near 11 km and at the off nadir position a height gain of almost 2 km is observed. This discrepancy poses a problem when trying to solve for the brightness temperature at nadir level for the entire scanline.
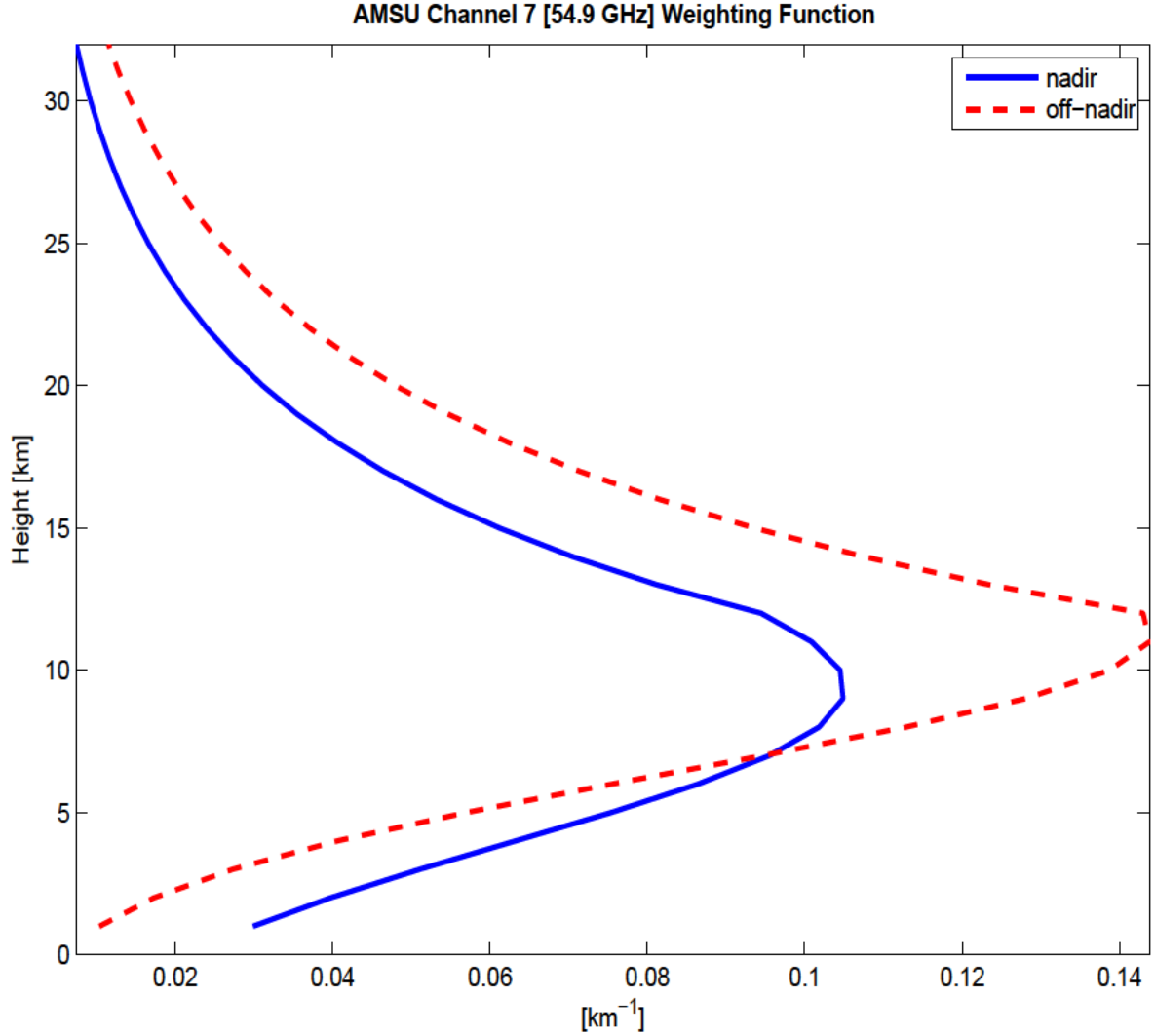
Figure 5. AMSU Channel 7 [54.9 GHz] Weighting Function at nadir and off nadir angles. At an incidence angel of 48.8° the weighting function corresponds to an edge of scan FOV which elevates the peak of the weighting function ≈ 2-3 km and effectively senses a higher level in the atmosphere.

### 2.2.2 Microwave Scattering and Absorption

The microwave portion of the EM spectrum is of special interest because of the scattering and absorption properties of water vapor, liquid cloud droplets, rain drops and ice particles at these frequencies. EM radiation can be transmitted, scattered, or absorbed through a medium or by matter. Scattering and absorption are dependent on the wavelength of radiation (frequency), shape of object, incident angle, and the

17

size of the object (Kidder and Vonder-Haar 1995). Water vapor and oxygen are effective absorbers and negligible scatterers at microwave frequencies due to their size and molecular properties, but water, liquid droplets and rain drops are susceptible to both scattering and absorption. Scattering of microwave radiation falls under three different regimes; Mie scattering, Rayleigh scattering, and geometric optics. The size of the scattering particle determines the scattering regime and also its absorptivity potential.

Water vapor and oxygen are the main two atmospheric absorbers in the microwave portion of the EM spectrum. These two atmospheric constituents absorb at different frequencies. While water vapor absorptivity depends on the water vapor content in the troposphere, oxygen can be assumed to be well mixed throughout A column of the atmosphere. Oxygen absorption of EM radiation at these frequencies is mainly due to molecular rotational transitions; microwave frequencies provide enough energy for these transitions to take place, absorbing radiation. The most important oxygen absorption band is centered at 60 GHz; a second absorption band, though much weaker, is also centered around 118 GHz.

Water vapor contains many more absorption bands that are distributed along the EM spectrum. These spectra of absorption bands are called the water vapor absorption continuum because its not limited to a single absorption band. In the microwave domain, water vapor absorption gets stronger as the frequency increases (Petty 2006). The two important water vapor absorption bands that fall within the microwave portion are at 22 GHz and a 180 GHz. Thus, the atmosphere is more transparent to water vapor at low frequencies with no precipitation.

Liquid water particles are both good absorbers and good scatterers but absorption dominates, while ice particles only scatter. Liquid droplets ($< 1mm$) and rain drops ($> 1mm$) absorb and scatter at both low and high frequencies. Scattering of radiation

can fall into three different regimes according to the size parameter $\chi$, which is defined as:

$$\chi = \frac{2\pi r}{\lambda} \tag{17}$$

Where r is the radius of the water liquid droplet or rain drop and $\lambda$ is the radiation wavelength. Figure 6 shows the different regimes according the values of $\chi$ (Wallace and Hobbs 2006).
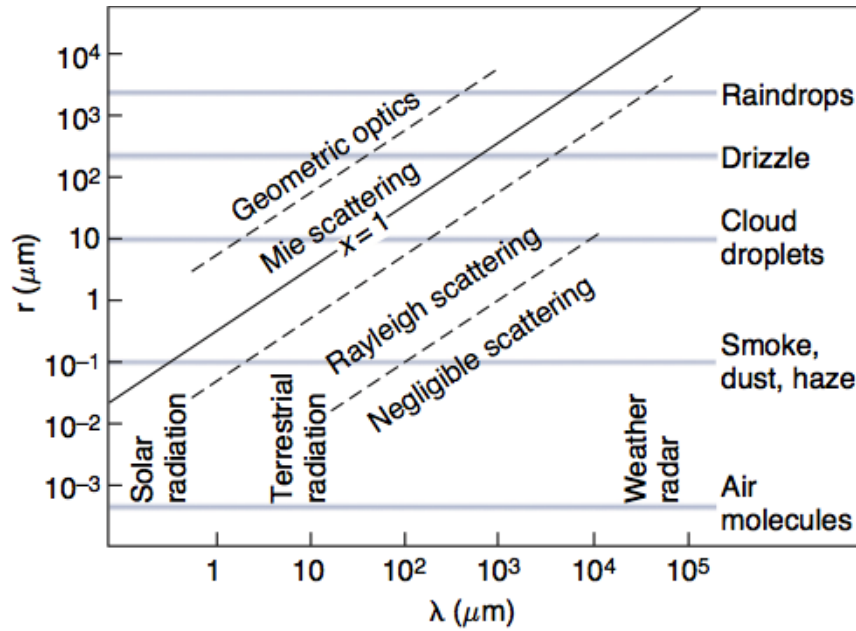


**Figure 6. The size parameter $\chi$ determines the scattering regime for the particle in question. In the microwave region the Mie regime plays a major role. (Wallace and Hobbs 2006). Used with permission.**

In the Mie regime, radiation interacts strongly with the particles, and the full Mie equations have to be solved. The Rayleigh regime is a simplified version of the Mie theory applied to smaller spherical shapes. Both theories are outside the scope of this paper and will not be detailed here, but it suffices to say that particle size determines the fate of the radiation and in the microwave frequencies the following has to be considered:

19

- Ice does not absorb microwave radiation; it only scatters.

- Liquid drops both absorb and scatter, but absorption dominates.

- Scattering and absorption increase with frequency and with rain rate. However ice scattering increases much more rapidly than liquid absorption.

At lower frequencies, $\approx< 60$ GHz, rain drops and water vapor absorption dominates, while scattering is of secondary importance. Above the oxygen absorption band, $\approx> 60$ GHz, microwave radiation is more susceptible to scattering. For frequencies around 60 GHz, both scattering and absorption of water particles is important.

Microwave radiometers can see through ice particles at low frequencies, and via liquid water absorption, map TC precipitation scenes. The low emissivity of ocean surfaces offers good contrast between the radiometrically cold brightness temperature of the ocean surface and the warm brightness temperature signature of the rainy scene. Above 50 GHz, ice particles are no longer transparent to microwave radiation and scatter upwelling radiation from below. Areas with scattering ice particles are mapped as cold brightness temperatures (Kidder and Vonder-Haar 1995; Gunn and East 1954).

Passive microwave radiometers like the AMSU, SSMI/S, and the ATMS fly on polar orbiting satellites. All these instruments are extensively utilized to provide insight into the structure of a TC, its formation, and development.

### 2.2.3  Advanced Microwave Sounding Unit (AMSU)

The AMSU instrument flies on board the NOAA satellites series 15-19 and the European Organization for the Exploitation of Meteorological Satellites (EUMETSAT) Meteorological Operational polar satellites (METOP) A and B. Six out of seven in-

struments are currently carrying out operations; the instrument on board NOAA-17 failed in 2003. AMSU-A and AMSU-B are two subsystems of the AMSU instrument. The AMSU-A is a passive microwave radiometer comprised of 15 channels. For atmospheric temperature soundings, 12 of these channels fall near the oxygen absorption band with quasi-vertical and quasi-horizontal polarizations that vary across a scanline. AMSU-B's five channels are near the 183 GHz water vapor absorption line, all of them vertically polarized and at 89 and 150 GHz. Table 3 shows the AMSU A-B channel and polarization distribution.

The AMSU instrument uses a cross-track scan strategy with 30 fields of view (FOV) per scan line for a total width of 1650 km and an instantaneous field of view (IFOV) size of 48 km at nadir from its altitude of 843 km. At the edge of the scan (FOV=30 or FOV=1, at an angle of ±48.9° off-nadir) the FOV expands to 147 km (Katsaros et al. 2014). See Figure 7.

The last AMSU instrument was launched in 2009 and flies on NOAA-19. One more instrument is expected to be placed in orbit and fly on METOP-C with launch scheduled for 2018. This instrument will be replaced by the ATMS instrument on future NOAA satellites.
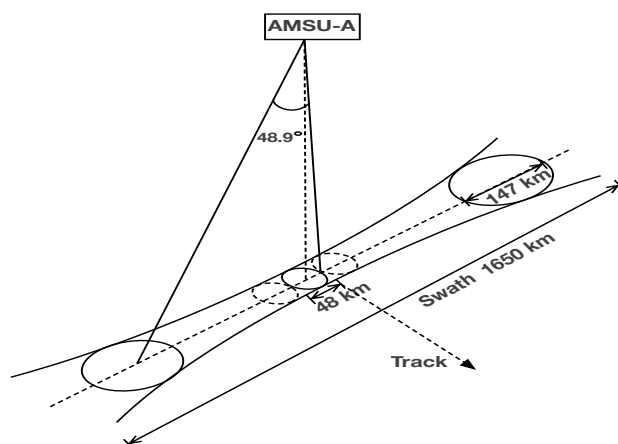


**Figure 7. AMSU Scan Geometry. With a scanline swath of 1650 km wide at 843 km in altitude the AMSU approximately covers the entire Earth surface with 7 full orbits. The edge of scan FOVs have an incidence angle of ±48.9°. The spatial resolution depends on the incidence angle.**

### 2.2.4 Advanced Technology Microwave Sounder (ATMS)

The ATMS is the latest passive microwave instrument in orbit. This instrument currently flies on S-NPP satellite launched October 28, 2011. The ATMS instrument combines the capabilities of both AMSU-A and AMSU-B instruments; with smaller volume, weight, and power consumption. The 22 channels are a combination of the AMSU-A/B frequency range with the addition of 3 channels: 57.76 GHz, 183.31±4.5 GHz, and 183±1.8 GHz. Lastly, the wider swath width of the ATMS allows for relatively smaller gaps between successive orbits with no gaps poleward of 20° latitude (Weng et al. 2012).

The ATMS scans cross-track with 96 FOVs extending 52.73° either direction from nadir yielding a scan line swath width of 2200 km from the satellite orbit altitude of 834 km. This scan geometry is shown in Figure 8. The spatial resolution at nadir for channels 1-2 is 75 km, for channels 3-14 it is 32 km, and for channels 17-22 it is 16 km. Table 4 shows the channel frequencies and polarizations.
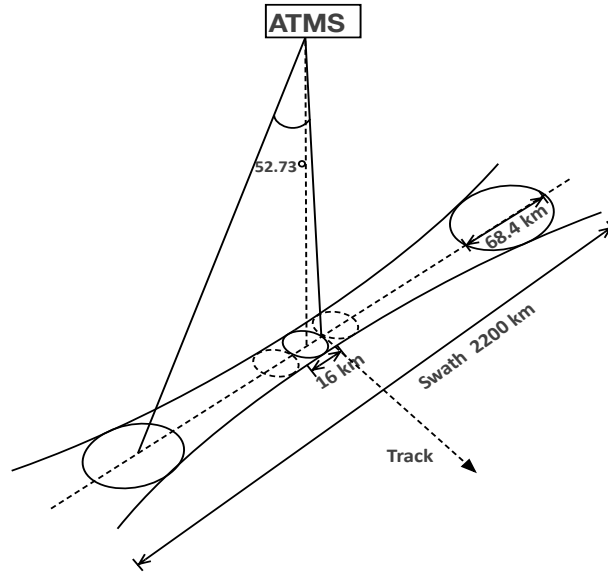


**Figure 8. ATMS Scan Geometry. With a scanline swath of 2200 km wide at 830 km in altitude the ATMS covers the entire Earth surface with 2 orbits leaving no gaps between consecutive scan tracks. The edge of scan FOVs have an incidence angle of ±52.7°. The spatial resolution depends on the beam width which is highly dependent on the incidence angle.**

**Table 3. AMSU-A/B channel list**

| Channel | Central Frequency (GHz) | Bandwidth (MHz) | Polarization |
|---|---|---|---|
| 1 | 23.800 | 270 | V |
| 2 | 31.400 | 180 | V |
| 3 | 50.300 | 180 | V |
| 4 | 52.800 | 400 | V |
| 5 | $53.596 \pm 0.115$ | 170 | H |
| 6 | 54.400 | 400 | H |
| 7 | 54.940 | 400 | V |
| 8 | 55.500 | 330 | H |
| 9 | f0=57.290344 | 330 | H |
| 10 | $f0 \pm 0.217$ | 78 | H |
| 11 | $f0 \pm 0.3222 \pm 0.048$ | 36 | H |
| 12 | $f0 \pm 0.3222 \pm 0.022$ | 16 | H |
| 13 | $f0 \pm 0.3222 \pm 0.010$ | 8 | H |
| 14 | $f0 \pm 0.3222 \pm 0.0045$ | 3 | H |
| 15 | 89.00 | 6000 | V |
| 1 | 89.0 | 1000 | V |
| 2 | 150.0 | 1000 | V |
| 3 | $183.31 \pm 7.0$ | 2000 | V |
| 4 | $183.31 \pm 3.0$ | 1000 | V |
| 5 | $183.31 \pm 1.0$ | 500 | V |

**Table 4. ATMS channel list**

| Channel | Central Frequency (GHz) | Bandwidth (MHz) | Polarization |
|---|---|---|---|
| 1 | 23.800 | 270 | QV |
| 2 | 31.400 | 180 | QV |
| 3 | 50.300 | 180 | QH |
| 4 | 51.760 | 400 | QH |
| 5 | 52.800 | 400 | QH |
| 6 | $53.596 \pm 0.115$ | 170 | QH |
| 7 | 54.400 | 400 | QH |
| 8 | 54.940 | 400 | QH |
| 9 | 55.500 | 330 | QH |
| 10 | f0=57.290344 | 330 | QH |
| 11 | $f0 \pm 0.217$ | 78 | QH |
| 12 | $f0 \pm 0.3222 \pm 0.048$ | 36 | QH |
| 13 | $f0 \pm 0.3222 \pm 0.022$ | 16 | QH |
| 14 | $f0 \pm 0.3222 \pm 0.010$ | 8 | QH |
| 15 | $f0 \pm 0.3222 \pm 0.0045$ | 3 | QH |
| 16 | 89.5 | 5000 | QV |
| 17 | 165.5 | 3000 | QH |
| 18 | $183.31 \pm 7.0$ | 2000 | QH |
| 19 | $183.31 \pm 4.5$ | 2000 | QH |
| 20 | $183.31 \pm 3.0$ | 1000 | QH |
| 21 | $183.31 \pm 1.8$ | 1000 | QH |
| 22 | $183.31 \pm 1.0$ | 500 | QH |

### 2.2.5 Special Sensor Microwave Imager/Sounder (SSMI/S)

The SSMI/S instrument flies on the DoD's DMSP satellite series. It combines the capabilities of all the previous DMSP microwave instruments: the SSM/T-1 temperature sounder, the SSM/T-2 moisture sounder, and the SSM/I imager. The SSMI/S currently flies on DMSP F16 through F19. The first SSMI/S was launched in October of 2003 and the latest launch was in April 2014. The SSMI/S microwave radiometer offers constant FOV throughout its conical scan geometry, and vertical and horizontal polarizations on its imager and environmental channels.

The SSMI/S scan conically at a fixed angle of 45° over a scan line swath width of 1707 km. This feature allows for constant spatial resolution and polarization over its 24 channels (Katsaros et al. 2014). Figure 9 depicts the conical scanning strategy.
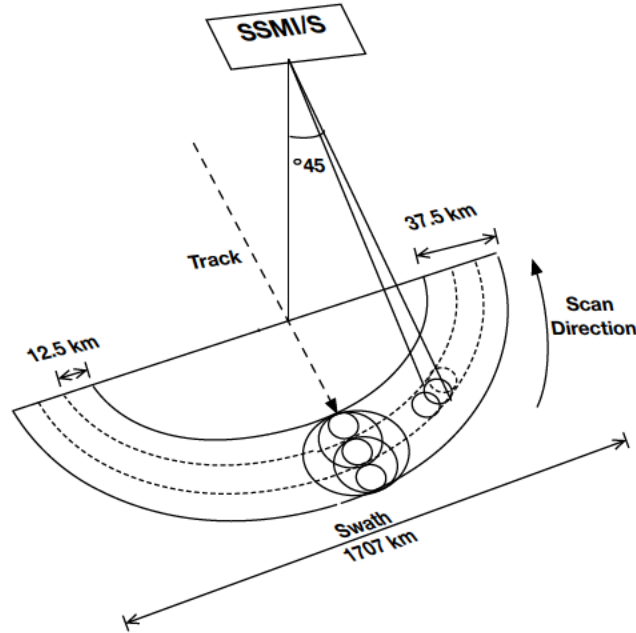


**Figure 9. SSMI/S Scan Geometry. The conical scanning strategy of the SSMI/S allows the FOV to maintain their spatial resolution throughout the scanline. With a constant scan angle of 45° channels retain their polarization. The scan swath covers 1707 km at at altitude of 850 km.**

SSMI/S channels are distributed over a broad range of frequencies from 19 GHz to 183 GHz. Table 5 shows the channels' distribution and their specific resolution and polarization. The channels are characterized by four main categories of measured parameters: Lower Air Sounding (LAS), Upper Air Sounding (UAS), Environmental (ENV) and imaging (IMA) data (Bell et al. 2006).

**Table 5. SSMI/S channel list**

| Channel | Center frequency (GHz) | Polarization | Channel spatial resolution (km) | Channel application |
|---|---|---|---|---|
| 1 | 50.3 | V | 37.5 | LAS |
| 2 | 52.8 | V | 37.5 | LAS |
| 3 | 53.596 | V | 37.5 | LAS |
| 4 | 54.4 | V | 37.5 | LAS |
| 5 | 55.5 | V | 37.5 | LAS |
| 6 | 57.29 | RCP | 37.5 | LAS |
| 7 | 59.4 | RCP | 37.5 | LAS |
| 8 | 150.0 | H | 12.5 | IMA |
| 9 | $183.31 \pm 6.6$ | H | 12.5 | IMA |
| 10 | $183.31 \pm 3$ | H | 12.5 | IMA |
| 11 | $183.31 \pm 1$ | H | 12.5 | IMA |
| 12 | 19.35 | H | 25 | ENV |
| 13 | 19.35 | V | 25 | ENV |
| 14 | 22.235 | V | 25 | ENV |
| 15 | 37.0 | H | 25 | ENV |
| 16 | 37.0 | V | 25 | ENV |
| 17 | 91.655 | V | 12.5 | IMA |
| 18 | 91.655 | H | 12.5 | IMA |
| 19 | $63.283248 \pm 0.285271$ | RCP | 75 | UAS |
| 20 | $60.792668 \pm 0.357892$ | RCP | 75 | UAS |
| 21 | $6.283248 \pm 0.357892 \pm 0.002$ | RCP | 75 | UAS |
| 22 | $6.283248 \pm 0.357892 \pm 0.0055$ | RCP | 75 | UAS |
| 23 | $6.283248 \pm 0.357892 \pm 0.016$ | RCP | 75 | UAS |
| 24 | $6.283248 \pm 0.357892 \pm 0.050$ | RCP | 37.5 | LAS |

## 2.3 Joint Typhoon Warning Center (JTWC) and National Hurricane Center (NHC)

JTWC produces TC warning products for DoD installations in the Western North Pacific, while the NHC produces similar products for the Atlantic and Eastern Pacific Oceans. These products include 6-hourly forecasts of TC track, intensity, and 34-, 50-, and 64-kt wind radii out to 120 hours. The accuracy of JTWC and NHC TC forecasts depends critically on accurate numerical weather prediction (NWP) model forecasts. These models are highly dependent on accurate TC position and intensity analyses to properly initialize and assimilate data.

Forecasters at these two institutions primarily utilize animated visible, water vapor, and infrared imagery from geostationary satellites to identify potential for TC development. When a tropical disturbance with a low level circulation is observed, forecasters begin the process of identifying the center of the low level circulation. This is a time-consuming and laborious process, especially when the center of circulation is covered by anvil clouds or cirrus blow-off associated with the convection from the TC itself. Once the storm matures in its development process, microwave imagery and sounding data are utilized to locate the position of the storm based on the passive microwave warm core signature. Intensity estimates are also obtained using the brightness temperature difference between the warm core and the surrounding environmental brightness temperature.

JTWC and NHC are not only responsible for issuing warning products, but they also contribute to the NWP process. When a storm is fixed and an intensity based on satellite techniques has been estimated, these organizations influence NWP models' forecasts by bogusing the model at initialization. Bogusing is the process of manually placing the coordinates of the TC center and its estimated MSLP in the model's analysis. This process allows the models to ingest the most accurate TC position and

intensity instead of the numerical solution from the previous model run. This method increases the accuracy of the forecast track and intensity.

NHC and JTWC keep records of all the data collected during the life span of TC. At the conclusion of each TC season after a long verification process, a "best track" archive is created for each storm. These best track files contain position, intensity, and wind radii at 6-hour intervals for the duration of the storm. In the case of the Eastern Pacific and WESTPAC, where aircraft reconnaissance is limited, the level of confidence in the verification process is not as high since no in-situ observations are available.

Utilizing passive microwave data to characterize TC position and intensity adds an increased level of certainty to the products issued by NHC and JTWC. multiple passive microwave techniques are available to these organizations, which provide objective intensity and location estimates, thereby helping to lower the burden on human analysts.

## 2.4 Previous Research

Passive microwave remote sensing meteorology is a relatively new field that derived from the need to further exploit satellite meteorology. This section covers previous research in TC passive microwave remote sensing. Brief overviews are presented of previous published work and how those results contribute to the objective of this paper. It is important to note that previous work related to TC intensity estimates involving the SSMI/S is limited, so this section focus in on AMSU and its predecessors.

### 2.4.1 SCAMS-based Warm Anomaly Technique

Using data from the Nimbus 6 Scanning Microwave Spectrometer (SCAMS), Kidder et al. (1978) presented a technique to correlate the warm core temperature

anomaly in the 55.45 GHz channel to TC minimum surface pressure. A correlation coefficient of -0.89 and a best standard deviation from the regression line of $\pm 15$ mb to the MSLP were found. These results then were used to estimate tangential wind speeds using the gradient wind balance. The left plot on Figure 10 shows the brightness temperature anomaly vs the central pressure of 36 different storms; 27 typhoons and 9 hurricanes. The right plot shows the radius of the storm vs the wind speed for four different storms from the bank of data analyzed.
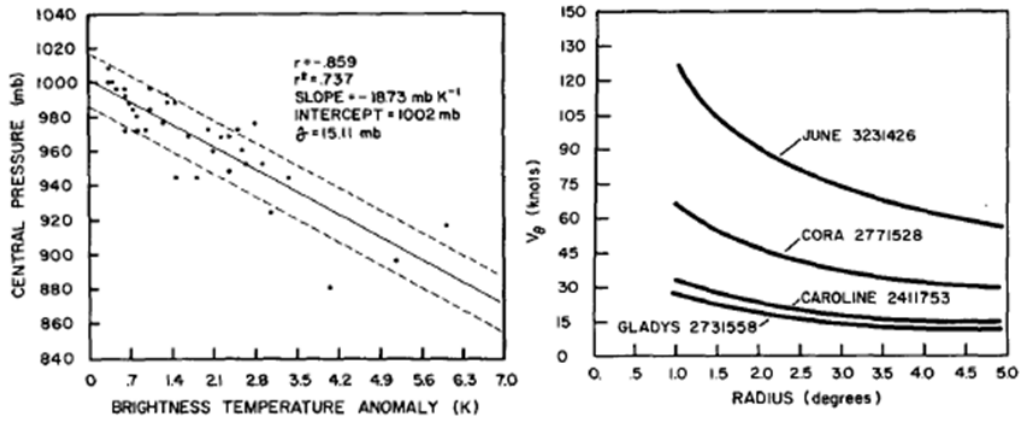


Figure 10. **Temperature anomaly correlation with MSLP at 55.45 GHz and derived wind speed. Left: correlation coefficient of -0.859 and standard deviation of $\pm 15$ mb was found using a linear regression method for 36 storms; 27 typhoons and 9 hurricanes. Right: Wind speed distribution after the gradient wind balanced relation was applied to the MSLPs derived from TC passive microwave brightness temperatures. Kidder et al. (1978). ©American Meteorological Society. Used with permission.**

### 2.4.2 MSU-based Warm Anomaly Technique

Velden and Smith (1982) used the AMSU's predecessor, the Microwave Sounding Unit (MSU) to find a correlation between TC development and the warm core anomaly vertical distribution. In expanding Kidder's work, Velden and Smith (1982)'s technique used a newer and better resolution microwave instrument; NOAA's MSU.

In their study, the 250 mb tropospheric temperature level was used to calculate the Laplacian and gradient of the temperature field. This parameter was tracked to investigate the time evolution of the warm core anomaly in the central column of the storm. Their results show the largest warm core anomaly corresponds to the peak intensity of the TC, and also found correlation coefficients that exceeded 0.90 and standard deviations from the MSLP and wind speeds of 6 mb and 11 kt respectively corresponding to estimates from the NHC. Figure 11 shows the warm core anomaly vertical distribution through the life span of the storms.
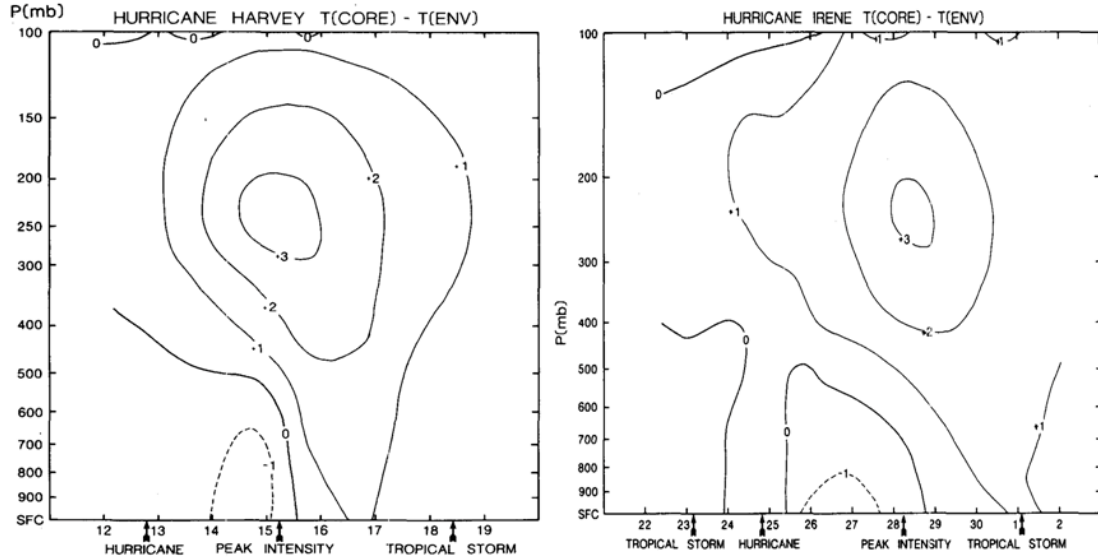


**Figure 11. Left: Hurricane Harvey warm core anomaly. Right: Hurricane Irene warm core anomaly. The warm core anomaly for both storms is at its largest magnitude at the same time as the storm's peak intensity. Note the temperature anomaly area grows and moves lower in height as the TC weakens. Velden and Smith (1982). ©American Meteorological Society. Used with permission.**

### 2.4.3 AMSU-based Warm Anomaly Technique

Brueske and Velden (2003) utilized AMSU's sounding channels near 55 GHz to characterize the temperature field near 250 mb. The AMSU weighting function increases in height at the edge of the scanline due to the dependency on the scan angle.

In order to compensate for the FOV height increase off nadir, they used a limb correction technique. This technique uses adjacent channels with lower weighting functions to correct for the height discrepancy on the weighting function of the 54.94 GHz channel at the edges of the scanline. After limb correction is performed, the adjusted brightness temperatures of all channel 7 FOVs correspond to the same height. Figure 12 shows a schematic of the height gain with off nadir angle increase.
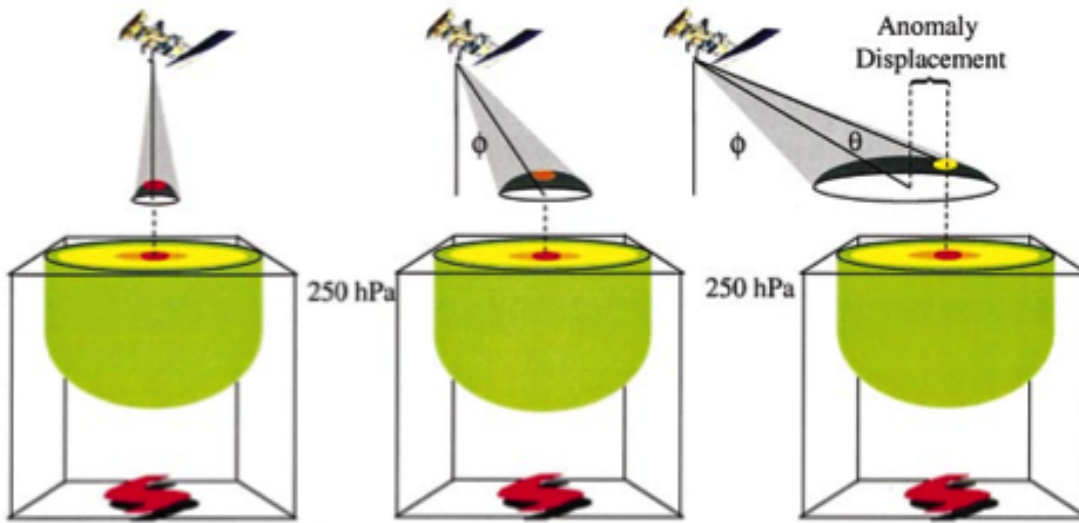


**Figure 12. AMSU's diagram illustrating the footprint interaction with the Upper Tropospheric Warm Anomaly (UTWA) as a function of the scan angle. FOV and height gain at the edge of the scan-line results in anomaly displacement. Brueske and Velden (2003). ©American Meteorological Society. Used with permission.**

A linear regression was then used to correlate brightness temperatures to MSLP. In addition, they also used AMSU-B's 89 GHz channel to infer TC "eye" size by characterizing the moisture field and to more accurately find the position of the storm. In their investigation they discussed out the susceptibility to hydrometeor scattering of the 54.94 GHz frequency and possible brightness temperature contamination when convection extends deep into the troposphere. Additionally, they found that

the size of the storm's warm core in relation to the FOV resolution can impact the reliability of intensity analysis using the warm anomaly, since the size of the storm can be smaller than the IFOV. Figure 13 shows a vertical cross-section of Hurricane Floyd's brightness temperature anomaly derived from NOAA-15 AMSU-A radiance data with limb correction applied. A warm anomaly of 18°C was observed and aircraft reconnaissance observed an MSLP of 924 mb.
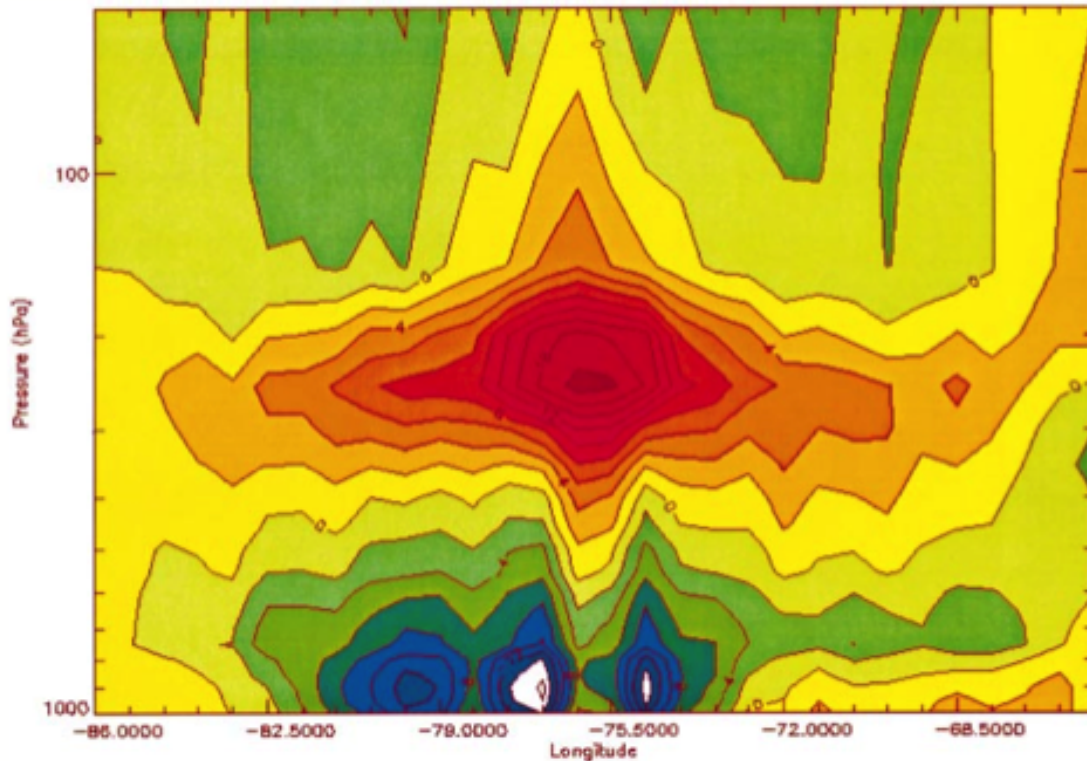


**Figure 13. Hurricane Floyd 1238 UTC 14 Sep 1999. Vertical temperature cross-section, 18°C warm anomaly was observed at 250 mb. Aircraft reconnaissance reported MSLP of 924 mb at 1113 UTC. Brueske and Velden (2003). ©American Meteorological Society. Used with permission.**

### 2.4.4   TC Wind Retrievals from Microwave Imagery

Wind retrievals using passive microwave imager channels is one the most important derived parameters of satellite microwave meteorology. Currently, various algorithms exist that can provide operational forecasters with this information. Unfortunately, algorithms using the imager channels do not work well around precipitation due to the attenuation and scattering by hydrometeors and water vapor (Goodberlet et al. 1990). Algorithms using the sounding channels are better suited to provide TC estimates using the hypsometric and gradient wind balance approach.

Sounding channels are capable of producing temperature profiles of the atmosphere. In TCs the warm anomaly associated with the core of the storm can be retrieved by measuring the brightness temperature of the core and comparing it to the brightness temperature of the surrounding environment. Assuming hydrostatic and gradient balance, the tangential wind speed can be derived to a good approximation; to determine the tangential wind speed, it is necessary to compute the pressure gradient of the cyclone. The first step is to retrieve the radial distribution of the brightness temperatures at different pressure levels. The hydrostatic equation is then integrated to determined the height of the different pressure levels where there are brightness temperature pixels. Once the brightness temperature and pressure fields are known, the gradient wind equation is solved. Results show lower tangential wind speeds than actual tangential wind speeds. These anomalies are attributed to the attenuation of the signal due to water vapor and the averaging of the tangential wind speed over the large instrument FOV (Kidder et al. 2000). Figure 14 shows the temperature anomaly as observed by the AMSU instrument (left figure) and the estimated wind speed using the algorithm (right figure).
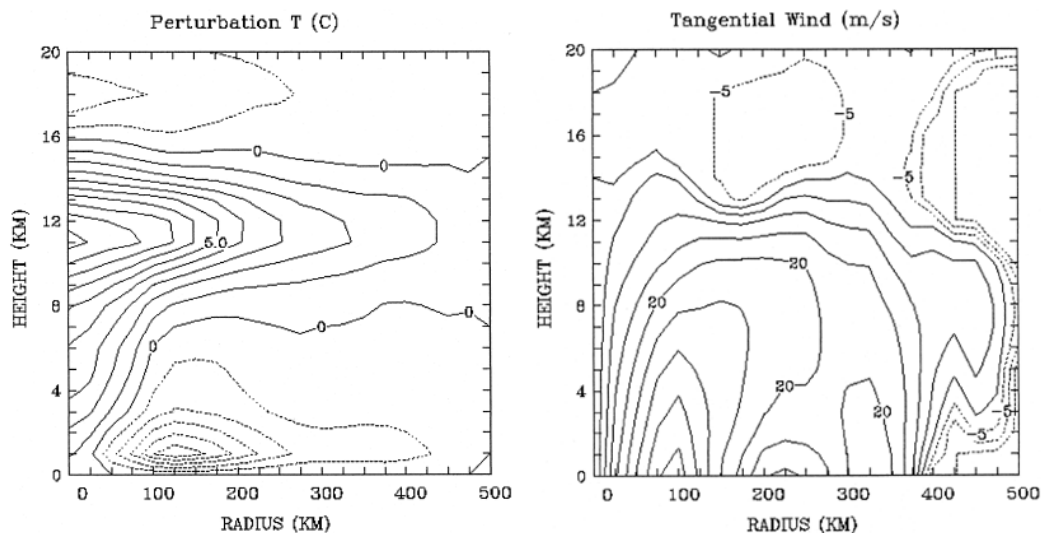
**Figure 14. Tangential average wind speeds derived from the temperature anomaly observed by the AMSU instrument for hurricane Bonnie at 1200 UTC 25 Aug 1998. Kidder et al. (2000). ©American Meteorological Society. Used with permission.**

### 2.4.5 Observations of TCs with Passive Microwave Sensors: Imagery Applications from Naval Research Lab

Passive microwave imagery utilizes atmospheric window frequencies that are sensitive to atmospheric precipitation features. These frequencies are well suited to map TCs due to water vapor, liquid water attenuation, and ice particle scattering, as discussed by Hawkins et al. (2008). The oxygen absorption signature not only measures the warm core magnitude but also provides a somewhat accurate position to the TC core.

The Naval Research Lab (NRL) maintains a web page focusing on TC imagery. Using storm fixes from NHC, CPHC, and JTWC, the web page can accurately track TCs in realtime. Passive microwave data from the SSMI/S, ATMS, and AMSU instruments are available via Fleet Numerical Meteorology and Oceanography Center (FNMOC), the Air Force Weather Agency (AFWA), and NOAA. The entire constellation of DMSP, NOAA, and NPP polar orbiting satellites are available, Reducing the time span between satellite overpasses.

33
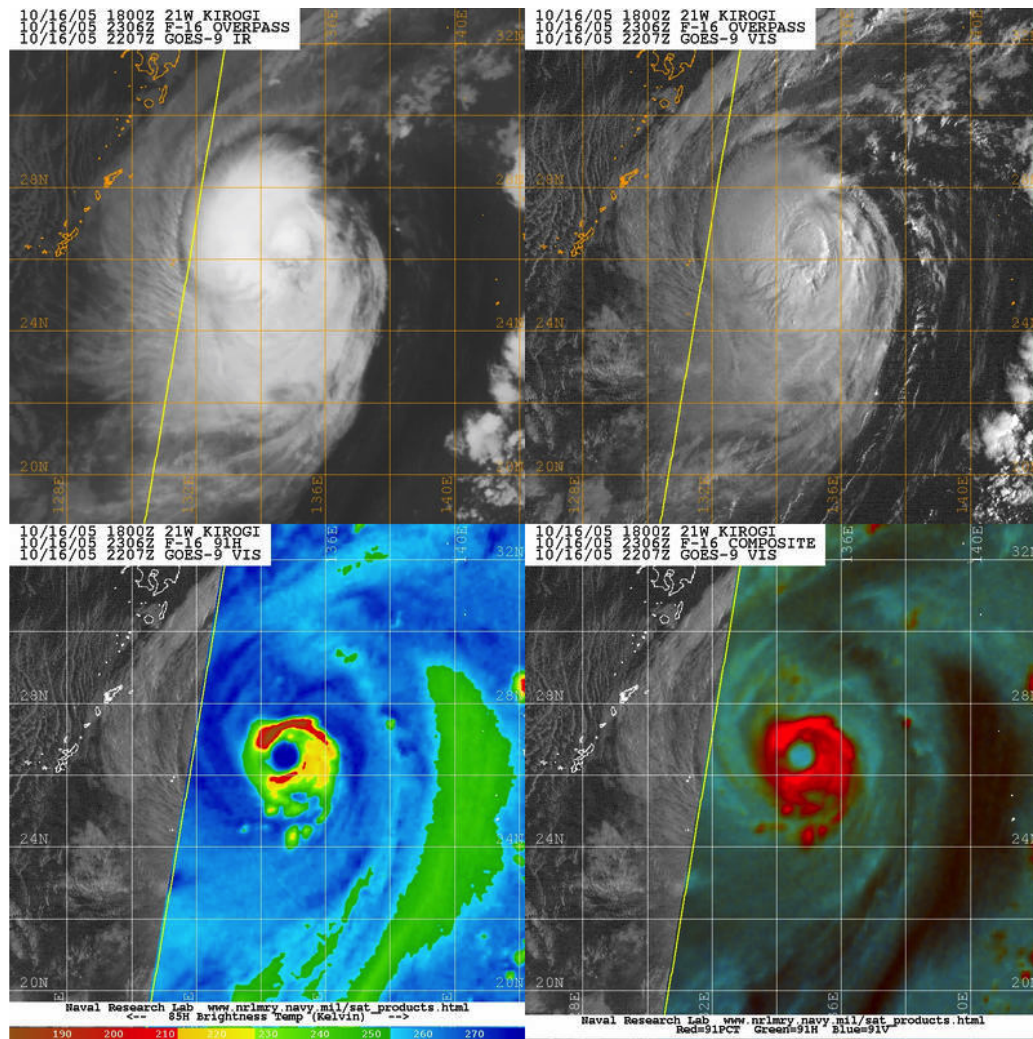
**Figure 15. 16 Oct 2005. Top left: IR image of Typhoon Kirogi, Top right: VIS image of Kirogi. Bottom left: SSMI/S microwave image at 91 GHz H. Bottom right: 91 GHz Polarization Corrected Brightness Temperature (PCT). Note the clearly defined inner-core ( "storm eye") and closed precipitation band with scattering signatures where ice particles are present representative of strong convention in both microwave images. VIS and IR imagery do not show the same level of detail. Hawkins et al. (2008). NRL Tropical Cyclone Page (accessed 2014).**

Figure 15 is an example of an NRL product. Here, visible (VIS) and Infrared (IR) images are taken within a few minutes of the microwave image. The VIS and IR images show an overcast inner-core while the microwave image shows a well defined eye that can provide the forecaster a better storm position and TC intensity estimate based on the magnitude of the warm core anomaly.

# III. Methodology

## 3.1 Storm and Time Selection

Three seasons of TC data over the Northern Atlantic Ocean were collected for this study. All TCs over the Northern Atlantic Ocean from 2011 through 2013 are used to investigate TC intensity predictors as observed by satellite passive microwave imagery and sounding data. The Northern Atlantic ocean basin was chosen because of the extensive aircraft reconnaissance data available for this basin during any given season compared to any other tropical ocean. The North Atlantic basin is shown in
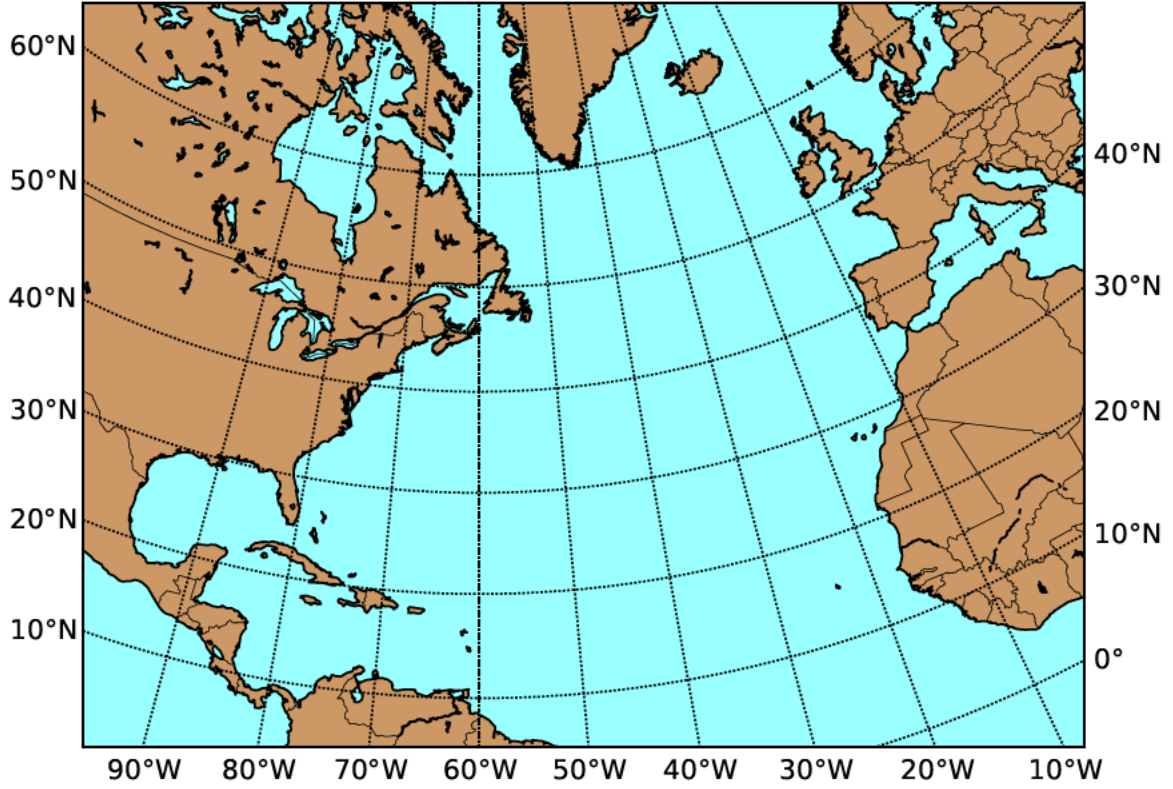


**Figure 16. Northern Atlantic Ocean**

All satellite files from 2011 to 2013 seasons were downloaded from NOAA's Comprehensive Large Array-Data Stewardship System (CLASS) website. Using the best track data from NHC; temporal and spatial information on every TC was used to find SSMI/S, AMSU, and ATMS satellite files that contained passive microwave overpass data corresponding to the TC. In-situ observations were acquired from aircraft reconnaissance vortex bulletins, also available from NHC. These files were used to retrieve the TC's actual location, MSLP, and estimated wind speed.

## 3.2   Data Sources

### 3.2.1   NOAA CLASS

Satellite files were obtained through NOAA CLASS; an online archive that provides access to satellite data from NOAA POES, NPP, and DMSP (CLASS accessed 2014). A search interface provides options for spatial, temporal, and data format/type of the various satellite data available in CLASS. Polar orbiting satellites fly over the same point on the surface of the Earth approximately two times every 24 hours with increasing coverage at higher latitudes; a polar orbiting satellite provides two TC overpasses a day over the tropical latitudes. The satellite files contain a full orbit of information, and by using the NHC best-track spatial and temporal parameters, one can extract the correct orbit containing the TC data.

### 3.2.2   SSMI/S SDRs

The SSMI/S instruments are carried by DMSP F-15 through F-19. TC data was collected from all satellites except F-19, which was recently launched on April 19, 2014. The data type used from the SSMI/S instrument are Sensor Data Records (SDRs). SDRs are files containing brightness temperatures derived from all the channels raw radiances, calibrated, geolocated and antenna pattern corrected. SDRs are derived from the raw instrument counts received at AFWA where they are processed.

### 3.2.3 AMSU Level-1B

The AMSU-A is carried by NOAA-15 through NOAA-19 and METOP-A and B. Data from all these platforms was collected, with the exception of NOAA-17. The Level-1B data type was used for this research. Level-1B data is processed at NOAA's National Environmental Satellite Data and Information Service (NESDIS) ground station after being downloaded from one of its many ground receiving stations. This data format is derived from raw instrument counts; the process involves pixel geolocation, satellite and solar azimuth and zenith estimation, computation of AMSU-A calibration coefficients, AMSU-A brightness temperature calibration, and quality control (NESDIS accessed 2014).

### 3.2.4 ATMS SDRs

SDR files were also collected from the Suomi-NPP ATMS. Similar to AMSU's data, these files are derived from raw instrument counts and downloaded at one of NASA's receiving stations. The raw counts are then processed at NESDIS where the are packed into HDF5 file format. These files contain geolocated and calibrated brightness temperatures for each channel. ATMS data was made available to the public in December 2011.

### 3.2.5 NHC TC Best Track

TC best track data for the North Atlantic basin was obtained from NHC (accessed 2014b). This organization tracks all TCs that develop in its area of responsibility (AOR). Best track files consist of a chronological record of TC category, latitude and longitude of the storm center, estimated maximum sustained winds in knots, minimum sea level pressure in mb, and 34-, 50- and 64-kt wind radii in km for up to four quadrants, at 6 hour intervals.

### 3.2.6   Aircraft Reconnaissance Vortex Bulletins

Aircraft reconnaissance data was obtained from NHC (accessed 2014c). Air Force WC-130J weather reconnaissance aircraft and NOAA's G-IV and WP-3D research aircraft fly missions into storms that pose a threat to the United States and its territories, as well as other nations in North America and the Caribbean. The frequency of missions is dependent on the threat level and proximity of the TC to land (U.S. Department of Commerce 2014). Vortex bulletins disseminated from these missions contain observed information on the storm's center position, TC minimum sea level pressure measured from deployed dropsondes, and estimated maximum wind speed. Aircraft reconnaissance vortex bulletins are not available for all storms since not all storms warrant aircraft missions.

### 3.3   Data Analysis Algorithms

This section discusses the processes used to analyze the data collected. In order to analyze TC structure, intensity, and location, visualization of the TCs brightness temperature is imperative. Passive microwave TC imagery and radial temperature profiles are derived from the satellite files gathered from NOAA CLASS using extraction algorithms developed in MATLAB®. These computer algorithms extract and map the geolocated brightness temperature pixels from each FOV and all scanlines containing the TC to be observed. Analysis and statistical methods are evaluated using these brightness temperatures. Radial brightness temperature profiles are used to look for patterns and passive microwave absorption and scattering signatures through all the channels of the instruments in order to derive intensity predictors that will be used in a statistical model to estimate TC intensity.

### 3.3.1 Terminology

Low frequency channels refers to SSMI/S environmental channels or AMSU and ATMS frequencies less than 37 GHz. High frequency channels refer to SSMI/S imaging channels or AMSU and ATMS frequencies greater than 89 GHz. Sounding channels refer to the frequencies near the 60 GHz oxygen absorption band. Table 6 lists the sounding, low, and high frequency channels by each instrument.

Table 6. **Low frequency, High frequency, and Sounding channels of the SSMI/S, AMSU, and ATMS instruments.**

| Frequency | SSMI/S [GHz] | AMSU [GHz] | ATMS [GHz] |
|-----------|--------------|------------|------------|
| Low | 19V, 19H 22V, 37V, 37H | 23.8, 31.4 | 23.8, 31.4 |
| High | 150H, 91.6V, 91.6H | 89 | 89.5, 165.5 |
| Sounding | 52.8H, 53.5H, 54.4H | 52.8, 53.6 54.4 | 52.8, 53.6, 54.4 |
| | 55.5H | 54.9 | 54.9 |

### 3.3.2 Data Selection

Satellite files corresponding to 52 TCs were downloaded from NOAA CLASS; 19 TCs were from 2011, 19 were from 2012, and 14 were from 2013. Table 7 shows the TC maximum intensity from the NHC best track data. No Tropical Depressions (TDs) are shown as all TCs in the best track archive developed to at least a Tropical Storm (TS) intensity. Also shown in this table are the number of TCs that had aircraft reconnaissance missions. For the three years covered by this study, approximately half of the Atlantic basin TCs had aircraft reconnaissance missions. 2013 was a relatively quiet season for TC formation with only 14 TCs, and consequently aircraft reconnaissance missions were also few; only five TCs had aircraft reconnaissance bulletins.

**Table 7. Number of TCs (Tropical Storms (TS) and Hurricanes (HU)) per season and TCs with aircraft reconnaissance**

| TC Season | 2011 | 2012 | 2013 | Total |
|---|---|---|---|---|
| Number of TCs | 19 TCs | 19 TCs | 14 TCs | 52 TCs |
|  | 7 HU, 12 TS | 10 HU, 9 TS | 2 HU, 12 TS |  |
| TC w/ Aircraft Recon | 14 TCs | 9 TCs | 5 TCs | 28 TCs |
|  | 6 HU, 8 TS | 5 HU, 4 TS | 1 HU, 4 TS |  |

Only the satellite files at times that matched an aircraft reconnaissance vortex bulletin were interrogated. Every TC file that had a vortex bulletin issued within $\pm$ 3 hours of the satellite overpass was kept for this study. Table 8 shows the distribution of satellite and reconnaissance matches by year. A total of 817 file matches were found in the three year study period.

**Table 8. Satellite and aircraft reconnaissance matches**

| 2011 | 2012 | 2013 | Total |
|---|---|---|---|
| 57 TD | 62 TD | 39 TD | 158 TD |
| 154 TS | 174 TS | 65 TS | 393 TS |
| 114 HU | 140 HU | 12 HU | 266 HU |
| 325 | 376 | 116 | 817 |

The matched files were divided into three data sets: testing, training, and validation. The three sets contain approximately equal numbers of TDs, TS, and HUs from all three seasons. Table 9 shows the contents of each data set. The majority of the matched files is composed of TS files, followed by HU, this is due to the recon-

naissance aircraft mission prioritization dictated by the NHC operations plan (U.S. Department of Commerce 2014).

**Table 9. Data set division**

| Testing | Training | Validation | Total |
|---------|----------|------------|-------|
| 53 TD | 53 TD | 52 TD | 158 TD |
| 131 TS | 131 TS | 131 TS | 393 TS |
| 89 HU | 89 HU | 88 HU | 266 HU |
| 273 | 273 | 271 | 817 |

### 3.3.3   TC Passive Microwave Imagery

TC images derived from SDRs or Level-1B data files offer valuable information on the structure and dynamics of the storm. The collection of geolocated passive microwave brightness temperature pixels from a TC provide insightful information on the maturity, physical processes, and strength of such storms based on absorption, scattering, or transmission of passive microwave radiation emitted from the TC. These signatures are enhanced when there is a uniform background with a contrasting brightness temperature like the ocean surface due to its low emissivity.

AMSU and ATMS cross-track scan strategy pose a disadvantage at the edge of the scanline. A TC that is located on the edge of an AMSU or ATMS scanline appears different than a TC at nadir because of the increased absorption along an oblique path compared to nadir. For instance AMSU's channel 7 weighting function peaks at approximately 200 mb at nadir but at the edge of the scanline the brightness temperatures sensed are from higher in the atmosphere, 150-100 mb or even higher depending on the latitude of the storm. To correct for this effect, limb-corrected brightness temperatures are used.

Brightness temperatures are limb-corrected using a statistical algorithm that exploits adjacent channels brightness temperatures (Goldberg et al. 2000). Using linear regressions, channel predictor coefficients are calculated based on the off nadir brightness temperatures correlation to the nadir brightness temperatures of corresponding adjacent channels. A weight is then calculated and applied to the channel's brightness temperatures to correct the limb biased temperatures. In this process, the channels acquire some noise at the expense of the calculated weight, but the resultant limb corrected brightness temperatures are worth this small cost (Goldberg et al. 2000; Liu and Weng 2007). Figure 17 shows AMSU's channel 7 brightness temperature vs the corresponding limb corrected brightness temperature. The correction brings out the TC warm core, but some noise is left behind after the correction.

SSMI/S brightness temperatures do not suffer from limb biases as a result of its conical scan strategy. Therefore, no correction algorithms are required for SSMI/S derived imagery. Any further use of the term brightness temperature will also be used to reference the AMSU and ATMS limb-corrected brightness temperatures.
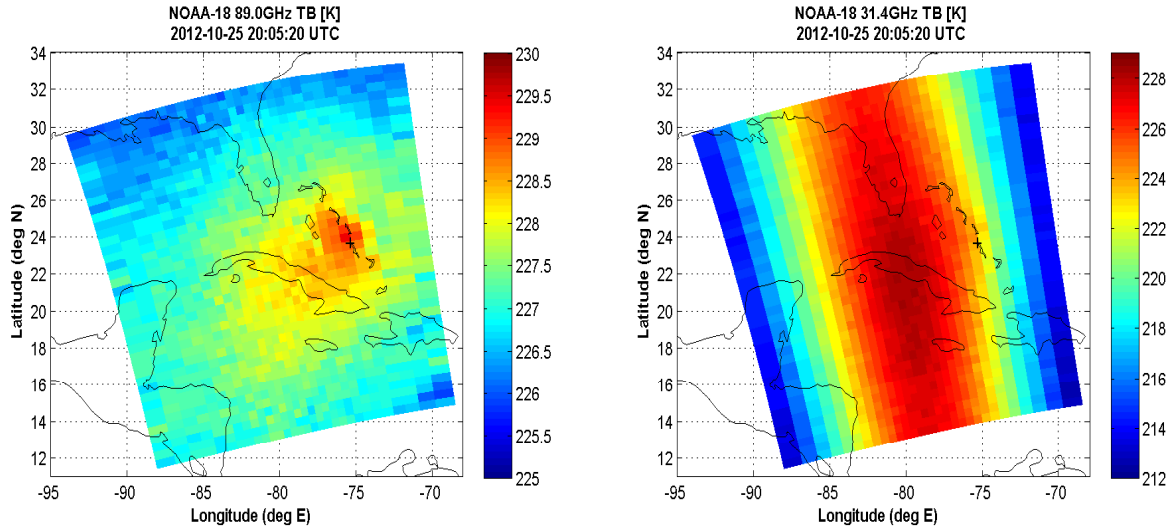
**Figure 17. TC Sandy, 25 Oct 2012. Left: Limb corrected AMSU-A brightness temperature. Right: AMSU-A raw brightness temperatures. Limb-correction brightness temperature algorithm is used to correct the channel's off nadir weighting functions for the AMSU and ATMS.**

### 3.3.4 TC Radial Temperature Profiles

Radial Temperature profiles are computed using evenly spaced concentric count bins from the center of the storm to an outer radius of 750 km radius. The bin sizes were determined by the instrument FOV size; 12 km, 16 km and 48 km are used for the SSMI/S, ATMS, and AMSU, respectively. The average brightness temperature inside each radial bin is calculated and plotted against the radial distance, resulting in the average radial temperature profile.

These TC average radial brightness temperature profiles provide different information depending on the channel being analyzed. Important storm thermodynamic and structure information can be inferred based on the TC warm core brightness temperature and its corresponding radial average brightness temperature profile.

Passive microwave radiation sensed from the low frequency channels is more susceptible to water vapor and liquid water absorption. Areas of higher relative humidity

43

and/or where precipitation corresponding to TC feeder-bands are present will appear warmer than low humidity or no-precipitation scenes due to absorption. The result is a temperature profile that is on average warmer than the environmental brightness temperature of the ocean background.

Higher frequency microwave signatures are more susceptible to scattering by ice particles and larger water drops (Kidder and Vonder-Haar 1995). These hydrometeors can be found in the upper troposphere where strong convective updrafts are responsible for their formation. Generally, stronger convection will be found in the eye wall regions, within a few hundred kilometers of the core. The upwelling radiance from the surface is scattered by the ice particles and replaced by reflected cold space radiance, resulting in much colder brightness temperatures in relation to the ocean and precipitation brightness temperature. The end result is a radial temperature profile that is on average colder in areas of strong convection than the environmental brightness temperature.

To avoid any land surface contamination in these TC radial brightness temperature profiles, the land surface pixels were omitted. Only brightness temperature pixels over the ocean are plotted. Figure 18 shows the SSMI/S radial temperature profiles for TC Irene, from 2023 UTC, 24 Aug 2011.

The sounding channels' radial temperature profiles are used to identify and measure TC warm core anomalies. Warm anomalies correlate to high latent heat concentration in the core of the TC. The stronger the warm anomaly, the more intense the TC (Demuth et al. 2006, 2003; Kidder et al. 2000; Brueske and Velden 2003). The resulting radial temperature profile will be on average warmer at the center of the storm and gradually cool down to the environmental temperature outside the influence of storm.
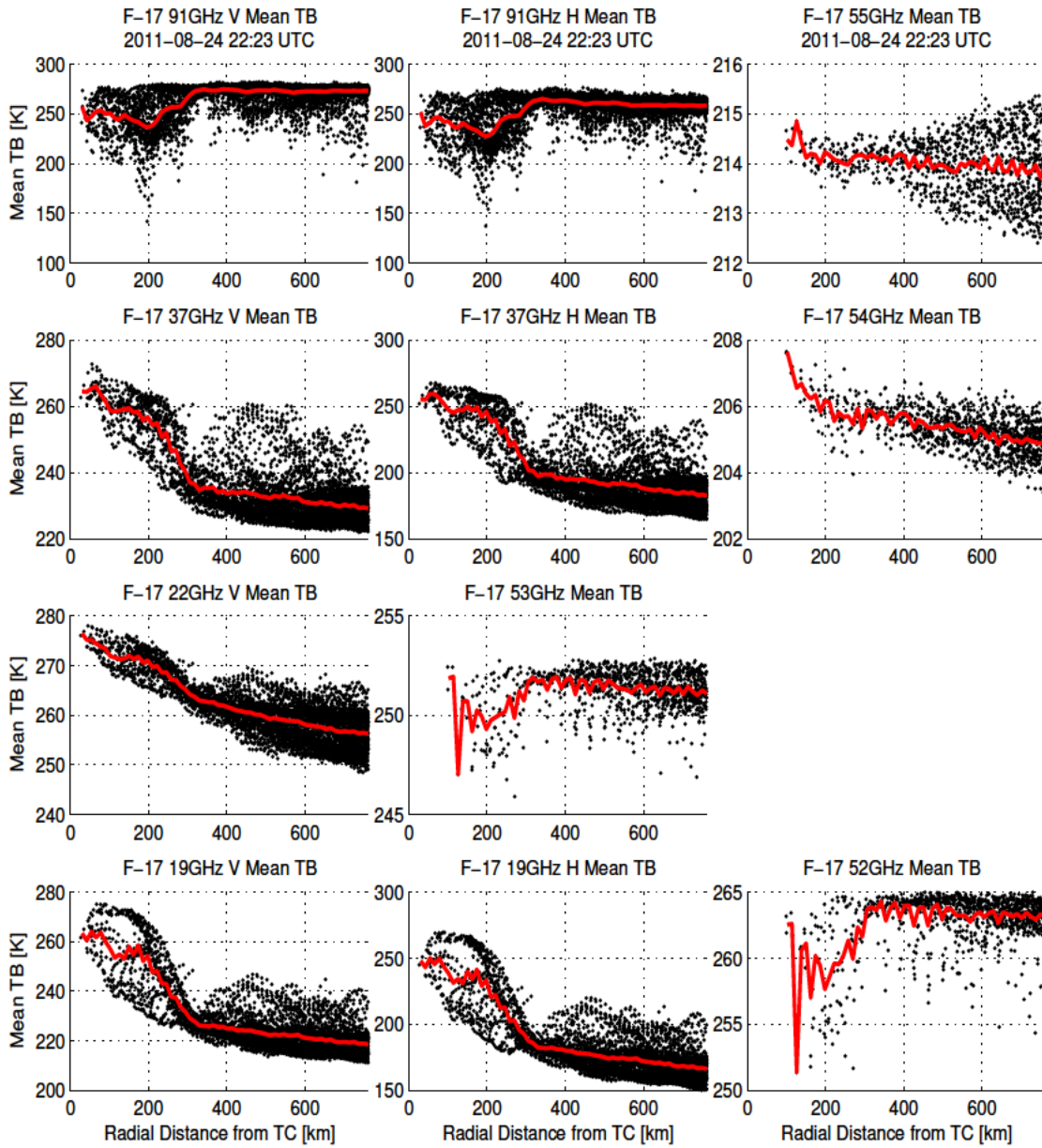
**Figure 18. Mosaic of Radial Temperature Profiles** for selected SSMI/S Channels on 24 Aug 2011 for TC Irene. Left two columns show the imaging and environmental channels; note the cooler brightness temperatures around 200 km on the 91 GHz channel profile corresponding to spiral band convection (scattering) and on the low frequency channels a warm ridge towards the core of the storm corresponding to the spiral band precipitation (absorption). The right column shows the sounding channels; the TC warm core anomaly can easily be observed in the 54 GHz channel frame.

45

### 3.3.5  Intensity Predictors

Current TC intensity estimates mainly use the warm core brightness temperature anomaly sensed at approximately 200 mb by the 55 GHz channel; AMSU channel 7, ATMS channel 8, and SSMI/S LAS channel 4. The warm core anomaly is defined by the difference between the maximum TC core brightness temperature and the average of the surrounding environment brightness temperature. The environmental average brightness temperature is defined as the brightness temperature in a ring outside any influence of the TC. Linear regressions were calculated between the warm core anomaly and the MSLP at different inner core and surrounding environmental radii.

Table 10 shows the warm core anomaly correlation coefficients against different surrounding environment radial distances. The ring with an inner radius of 700 km and outer radius of 750 km provided the best results and was selected as the optimal radial distance to use. The results also show a slight increase of the correlation coefficient at 1200 km but this radial distance is too large compared to the instrument swath. Other atmospheric phenomena can also affect the environmental brightness temperature at these ranges and results would be affected by them.

**Table 10.  Warm core anomaly correlation coefficients (r) vs radial distances for AMSU channel 7, ATMS channel 8 and SSMI/S LAS channel 4.**

| Radius [km] | 300 | 400 | 500 | 600 | 700 | 800 | 900 | 1000 | 1100 | 1200 |
|---|---|---|---|---|---|---|---|---|---|---|
| AMSU (r) | -.80 | -.83 | -.84 | -.85 | -.85 | -.85 | -.86 | -.85 | -.85 | -.86 |
| ATMS (r) | -.77 | -.78 | -.79 | -.79 | -.82 | -.79 | -.77 | -.75 | -.74 | -.74 |
| SSMI/S (r) | -.71 | -.74 | -.75 | -.75 | -.75 | -.75 | -.75 | -.75 | -.74 | -.75 |

These correlation coefficients used an inner TC core with a radius of 120 km. In order to also optimize the size of the TC core, various inner core radii were also tested using the environmental brightness temperature at the outer ring previously found. Table 11 shows the different TC warm core radii distances used to find an optimal warm core size.

**Table 11. Warm core anomaly vs TC core radii correlation coefficients (r) for AMSU channel 7, ATMS channel 8 and SSMI/S LAS channel 4.**

| Radius [km] | 50 | 100 | 150 | 200 | 250 | 300 | 350 | 400 | 450 | 500 |
|---|---|---|---|---|---|---|---|---|---|---|
| AMSU (r) | -.79 | -.85 | -.86 | -.85 | -.86 | -.86 | -.85 | -.85 | -.85 | -.85 |
| ATMS (r) | -.81 | -.81 | -.81 | -.81 | -.82 | -.82 | -.82 | -.82 | -.82 | -.82 |
| SSMI/S (r) | -.80 | -.76 | -.75 | -.74 | -.73 | -.73 | -.73 | -.73 | -.73 | -.73 |

Because we only care about the warmest brightness temperature pixel within the TC core FOVs, the core size might be considered trivial, but the results showed otherwise. The correlation coefficients are different for the three instruments at different radii, and decrease with radius for $r > 250$ km for all of the instruments. The smaller radius (50 km) does not represent the warm core size appropriately for the AMSU resolution of 57 km. In order to provide the algorithm with more than one pixel from which to find the warmest pixel, 250 km radius was chosen as the optimal warm core radius for all three instruments.

The objective of this study is to find passive microwave intensity predictors that can predict TC MSLP using the broad range of frequencies these microwave instruments offer. In addition to using the classical warm core anomaly, this study will also employ the following predictors:

- Temperature integrated radial area for both low and high frequency channels

- Temperature spread between low frequency and high frequency channels

- Maximum and minimum brightness temperature for low and high frequency channels

- Scattering corrected warm core anomaly

- TC latitude

A correction for FOV size growth at off nadir angles is also included for the ATMS and AMSU instruments as a predictor. Adding the above predictors and corrections to the stand-alone warm core anomaly method already in use is expected to improve previous results with correlation coefficients in the $\approx 0.90$ range found by Kidder et al. (1978), Velden and Smith (1982) Kidder et al. (2000), and Brueske and Velden (2003). The low and high frequency channels' response to precipitation is expected to respond to physical processes involved in the TC structure and thermodynamic development.

### 3.3.6 Temperature Integrated Radial Area

The temperature integrated radial area predictor is designed to measure the absorption and/or scattering of the upwelling passive microwave radiation by the TC in the low and high frequency channels, respectively. Figure 19 shows two TC Florence images derived from low and high frequency channels. Their corresponding radial brightness temperature profiles are also included. Note the overall warmer radial brightness temperature profile in the low frequency channel and the overall cooler brightness temperature profile in the high frequency channel compared to their respective average environmental brightness temperatures at 750 km.
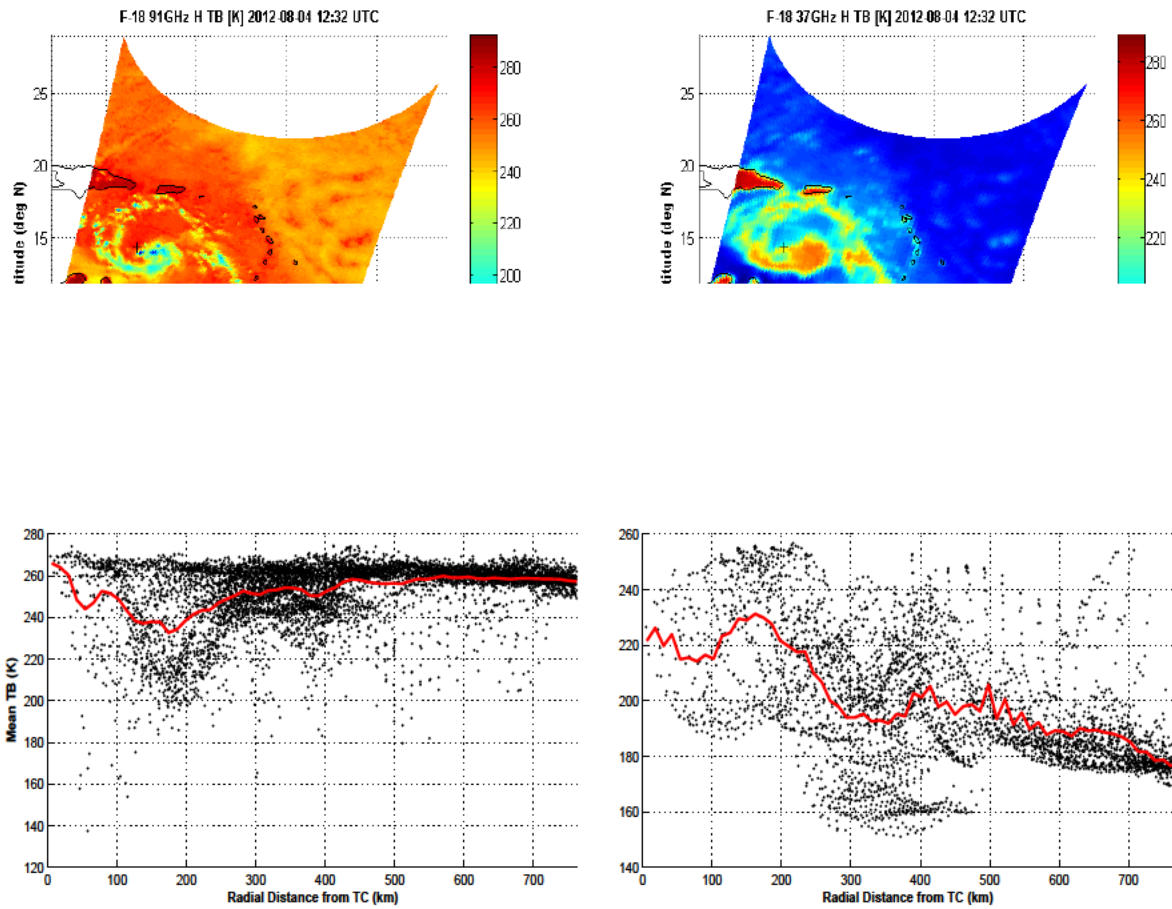
**Figure 19. SSMI/S TC Florence 37 GHz and 91 GHz images with corresponding TC radial brightness temperature profiles.** Bottom Right: Low frequency (37 GHz H) radial brightness temperature plot shows an overall warm temperature profile against the environmental average brightness temperature at 750 km away from the core of the storm. Bottom Left: High frequency (91GHz H) radial brightness temperature plot represents the scattering via the overall colder curve with respect to the average environmental brightness temperature at 750 km away from the core

The predictor is based on the assumption that as a TC undergoes development and strengthens, the relative humidity and feeder-band convection increases. The area under (at low frequencies) or above (at high frequencies) the brightness temperature profile consequently increases or decreases as the TC strengthens or weakens providing a proxy for intensification.

49

TC rain bands and high humidity values are represented by relatively warm temperature pixels in the scene at low frequencies. To measure the overall warming in the radial brightness temperature profile from the TC, the average temperature profile was normalized to the average environmental brightness temperature. The normalized low frequency brightness temperature profile is such that any positive values represent the warming associated with the absorption and any negative areas can be correlated to dry conditions where the ocean surface is exposed.

For the case of high frequency channels, the scattering signatures are due to ice particles and larger water drops. The TC radial brightness temperature profile is also normalized to the average environmental brightness temperature. Any portion of the curve that lies below the 0 K normalized temperature line is representative of the scattered radiation. Positive values can be neglected for this case because they represent non-scattering FOVs. Figure 20 shows radial profiles of both low and high frequency channels for TC Karen at 2229 UTC on 05 Oct 2013. The bottom row contains the normalized radial temperature profiles. Note the difference between the temperature gain in the low frequency channel vs the temperature depression in the high frequency channel at various radii out to 750 km.

The area under or above the 0 K is calculated using a trapezoidal method. For the case of the low frequencies, only the area above the 0 K was interrogated, while only the area below the 0 K line was used for the high frequency channels. To account for the increasing area of the concentric rings the radial distance is multiply by a factor of $2\pi r$. Figure 21 show the positive and negative area shaded for both the low and high frequency channels for the TC Karen radial profiles.
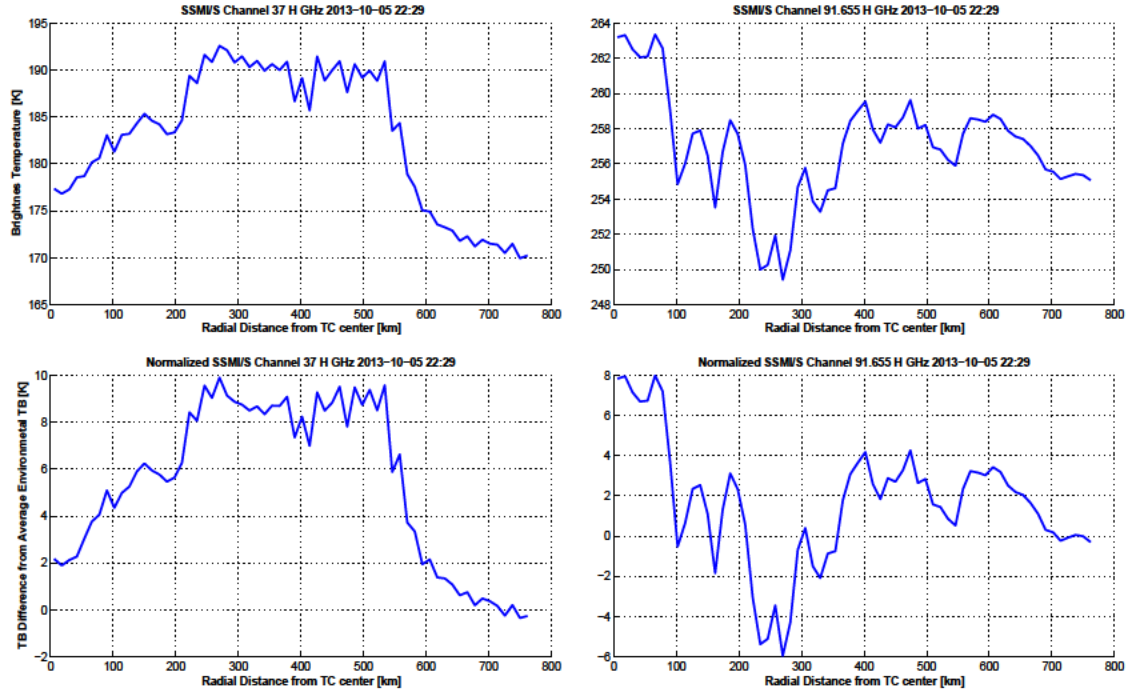
Figure 20. SSMI/S TC Karen Radial Average Brightness Temperature Profiles for both low and high frequency channels. Right column shows the normalized radial temperature profiles; brightness temperature gain or loss from the average environmental brightness temperature at 750 km represents a measure of absorption or scattering passive microwave radiation.
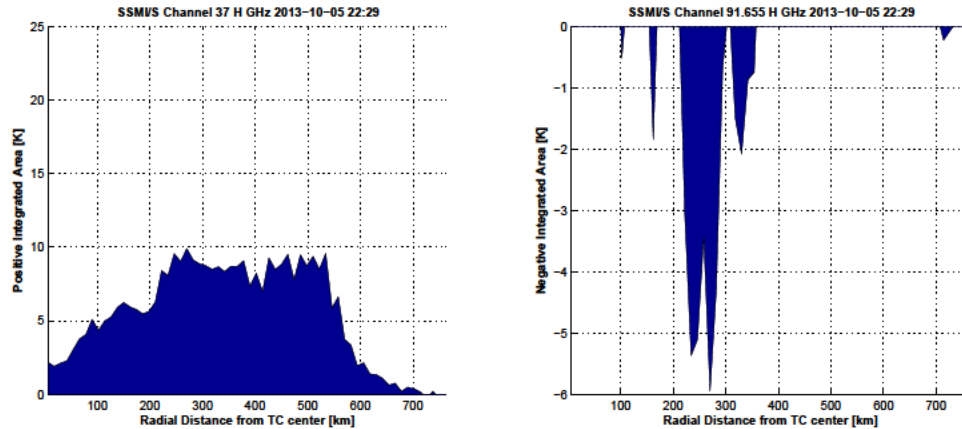


Figure 21. SSMI/S TC Karen Radial Average Brightness Temperature Integrated Area. Left: Positive Temperature Integrated Area for low frequency channel representing precipitation absorption. Right: Negative Temperature Integrated Area representing radiation scattering at high frequency channels. The two area calculations are derived from the normalized brightness temperature profiles and a factor of $2\pi r$ is applied to compensate for the concentric rings.

51

Positive Brightness Temperature Integrated Areas (BTIA) and negative BTIAs are calculated for the SSMI/S, ATMS, and AMSU low and high frequency channels. The resultant values are used as predictors to derive linear regressions with the MSLP.

### 3.3.7   Temperature Spread Between Low Frequency and High Frequency Channels

This predictor is also based on the radial brightness temperature profiles. The temperature spread is the magnitude of the difference between the peak absorption brightness temperature at low frequencies and the minimum scattering brightness temperature at high frequencies. The underlying principle of this predictor is that, as the TC increases in strength, the gap between the low and high frequency radial brightness temperature profiles increases. In most cases heavy precipitation will occur in areas with vigorous convection where ice particles are present, but not in all cases. In order to avoid situations where the TC's radial brightness temperature maximum and minimum are not co-located at the same radial distance or where the profile is not ideal, the normalized brightness temperature profiles are used. The maximum brightness temperature from anywhere in the low frequency radial brightness temperature profile and the minimum brightness temperature from anywhere in the high frequency radial profile is used. The two magnitudes are then added to derive the brightness temperature spread predictor. Figure 22 shows the average brightness temperature profile for TS Debby at 1450 UTC on 24 June 2012; both the peak brightness temperature and minimum brightness temperature occurred at the same radial distance from the storm center at the time of this satellite overpass.
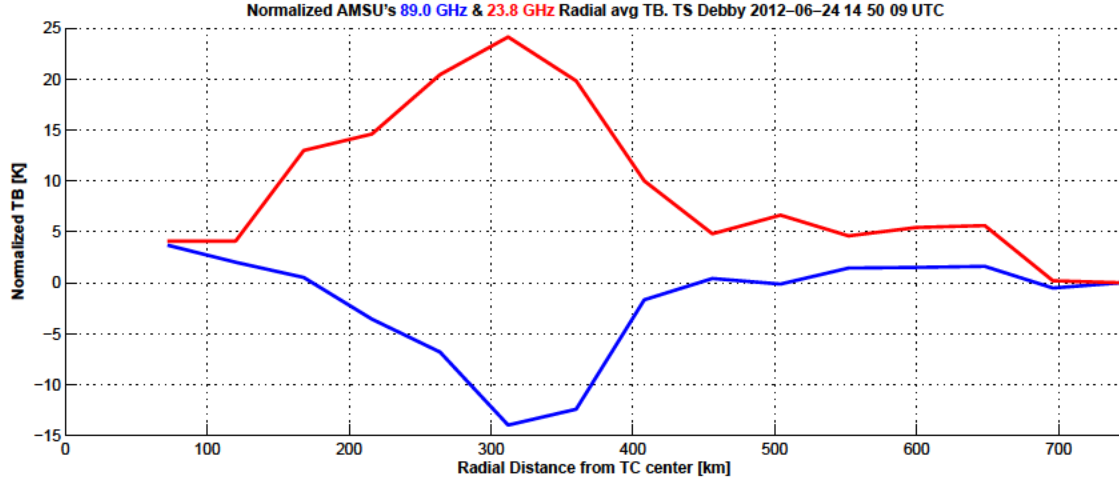
Figure 22. TS Debby's 23.8 GHz and 89.0 GHz radial brightness temperature profiles. Idealized example of the temperature spread between the peak low frequency brightness temperature and the high frequency minimum brightness temperature. The magnitude of the spread is then used as predictor for the MSLP.

The magnitude of the spread is then used as an intensity predictor for all three instruments and correlated to the MSLP using linear regression.

### 3.3.8 Maximum and Minimum Brightness Temperature in Low and High Frequency Channels

The maximum low frequency and minimum high frequency brightness temperatures were the next predictors tested. The objective of these predictors is to account individually for the absorption or the scattering that is occurring. The normalized radial brightness temperature profiles for the low and high frequencies are used for these predictors as well. The gain or loss from the environmental brightness temperature is computed as the maximum or minimum and then correlated to the MSLP via linear regression.

### 3.3.9   Scattering and Limb Corrected Warm Core Anomaly

The warm anomaly intensity predictor is the most common TC intensity predictor using passive microwave sounding frequencies. Previous research has found strong correlations between the warm core anomaly at 54-55 GHz and the MSLP. For this study, we also expect the warm core anomaly to be the leading predictor, as it has been validated and extensively studied by Kidder et al. (1978, 2000), Velden and Smith (1982), Demuth et al. (2003, 2006) and Brueske and Velden (2003). To maximize the quality of the sounding channel data, two corrections are made: limb correction and scattering correction. Limb correction was applied to all AMSU and ATMS channels as discussed previously. The scattering correction is used to attempt to reduce contamination of the warm core signature caused by hydrometeors scattering.

Sounding channels are susceptible to both absorption and scattering by hydrometeors, but the sounding channels of interest have weighting functions that peak in the upper troposphere where ice particles are mostly present, so the scattering effect is more pronounced in the sounding channels. Since liquid precipitation mainly occurs in the lower troposphere, the sounding channels are less susceptible to absorption effects. The two AMSU and ATMS low frequency window channels, 23.8 GHz and 31.4 GHz, are both susceptible to liquid water precipitation but a weak water vapor continuum absorption band residing around 22 GHz affects the 23.8 GHz channel's absorption by making it opaque more rapidly than the 31.4 GHz channel in a high relative humidity scene (Wacker 2005).

The algorithm used to correct the ATMS and AMSU temperature sounding channels uses an empirical model that utilizes the low frequency channels 1 and 2 (23.8 GHz and 31.4 GHz) versus high frequency channel (89.0 GHz) brightness temperatures. In order to isolate FOVs with scattering signatures, a theoretical no-scattering line was computed and fit to a scatter plot of the 89.0 GHz brightness temperature

vs a low frequency brightness temperature. Figure 23 shows these brightness temperature scatter plots for the entire training data set, one for the 89 GHz vs 23.8 GHz (left) and one for 89 GHz vs 31.4 GHz (right). The blue line was fit to the data and represents the expected brightness temperature relationship with no scattering.
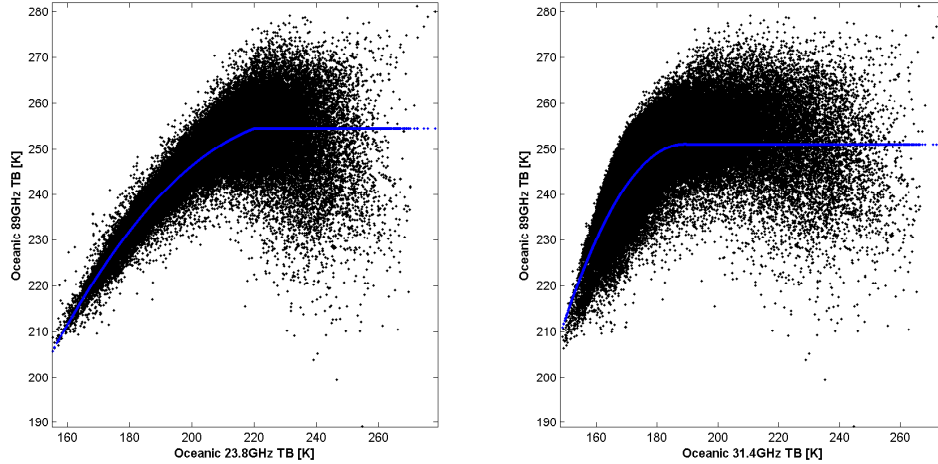


**Figure 23. AMSU Low and High Frequency Brightness Temperature Scatter Plots. High frequency vs low frequency channels are plotted to visualize a non-scattering vs scattering line. The statistical fitted line provides a threshold for scattered FOVs. The residuals (Temperature Depressions) from the FOVs below the line are computed and use to correct the channels for scattering.**

In Figure 23 land surface pixels are omitted and only pixels with ocean background are plotted. The y-axis shows all the FOVs from the 89 GHz channel; the low ocean surface emissivity for the horizontal polarized frequencies makes the clear ocean background appear as cold brightness temperatures. As clouds start to appear in the scene the 89 GHz brightness temperature warms up rapidly due to water vapor continuum absorption. Ice particles and large water drops are considered to be negligible or almost transparent in the low frequency channels, but this is not the case for the high frequency channels where these water particles are strong scatterers. Strong updrafts inside convective cells provide the dynamics for ice particle formation. Large water drops form via coalescence and are lofted into the upper troposphere. The upwelling microwave radiation is scattered by these particles and 89 GHz brightness temperatures will appear colder as a result. Figure 23 shows this scattering signature

as the 89 GHz brightness temperatures falling well below the fitted line.

Once scattering-affected pixels have been identified, the temperature depression between the fitted line and the pixels is obtained. This 89 GHz brightness temperatures depression is then correlated with sounding channels brightness temperatures. Figure 24 shows scatter plots of the sounding channels vs the 89 GHz brightness temperature depression. A least squares line is fit to the plot (blue) and the resultant regression coefficients are used to correct the sounding channels.
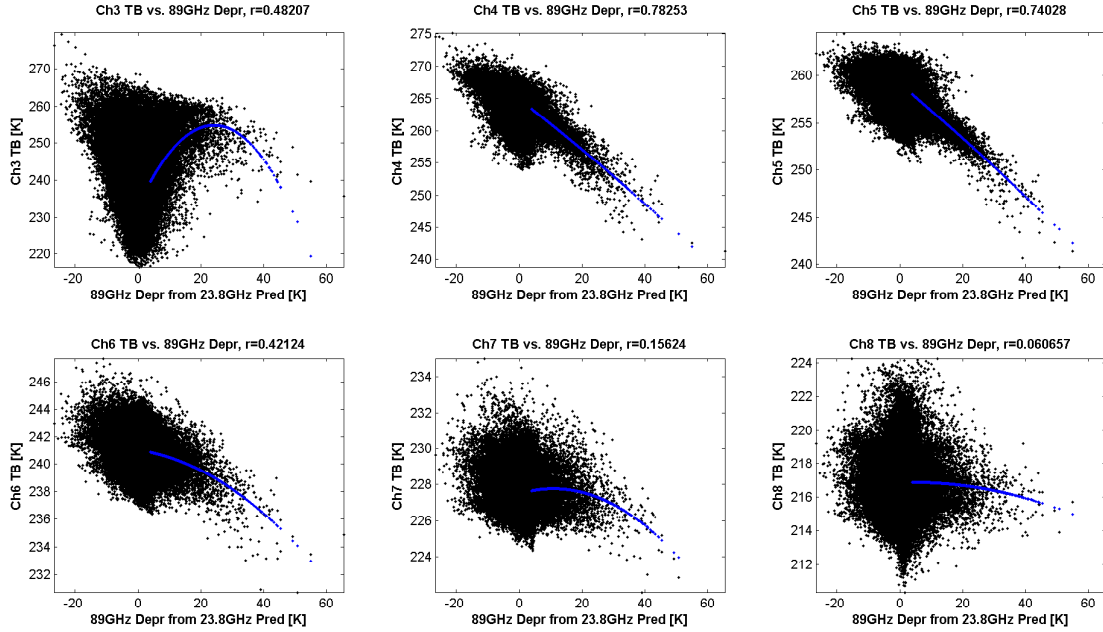


**Figure 24. AMSU Temperature Depression vs Sounding Channels Scatter Plots. A regression is computed between these channels to derive a regression equation to correct the sounding channels. The derived coefficients are applied to the corresponding channels to correct the scattering effects.**

The same process is repeated for the SSMI/S and ATMS sounding channels. The process for the SSMI/S takes an extra step because of the different spatial resolution between sets of SSMI/S channels. The environmental and imaging channels first have to be averaged to the LAS channel spatial resolution.

The SSMI/S environmental and the imaging channels are used as low and high frequency channels to correct for scattering effects. Environmental channels have a

native resolution of 25 km, whereas the imaging channels are 12.5 km. These channels have to be conformed to the LAS channel resolution of 37.5 km. Figure 25 shows the different FOV sizes centered on an imaging channel's latitude and longitude. The first step is to bring the imaging channels' resolution to the environmental channel using a linear interpolation between pixels. In order to match the resolution of the LAS channels, 3x3 groups of pixels are averaged with a weight according to the distance from the center beam location, in a way that pixels with matching coordinates weight more than pixels that are located further from the channel's beam center. The average process takes away some of the finer details of the higher resolution channels. but enables their scattering signatures to be used to correct the sounding channel brightness temperatures.
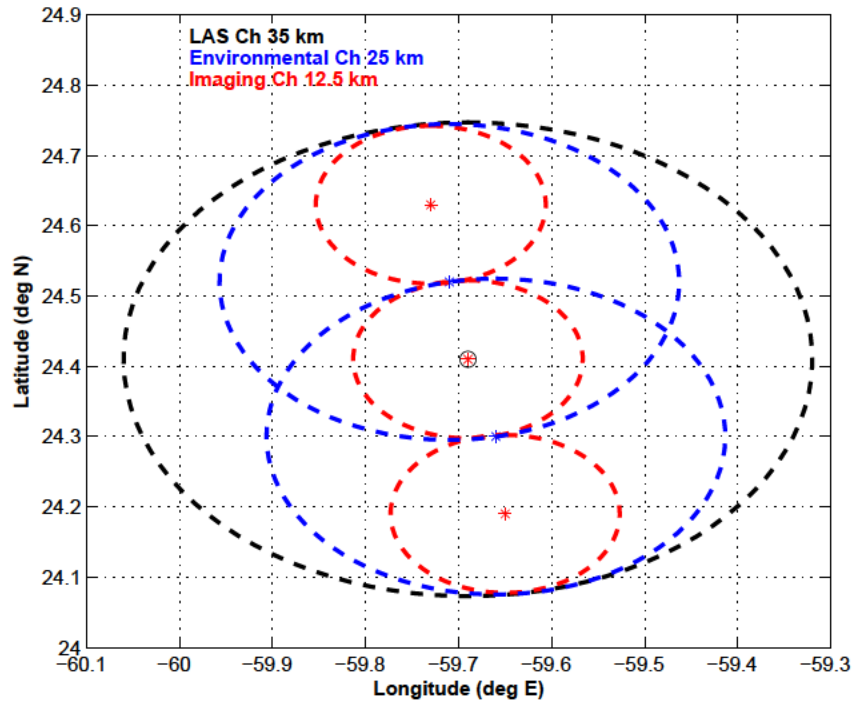


Figure 25. SSMI/S Spatial FOV Resolution. Imaging channel resolution is 12.5 km, Environmental channel are 25 km and LAS channel are 37.5 km. Convolution of the Imaging and Environmental channels to the LAS channels is performed to correct for scattering effects.
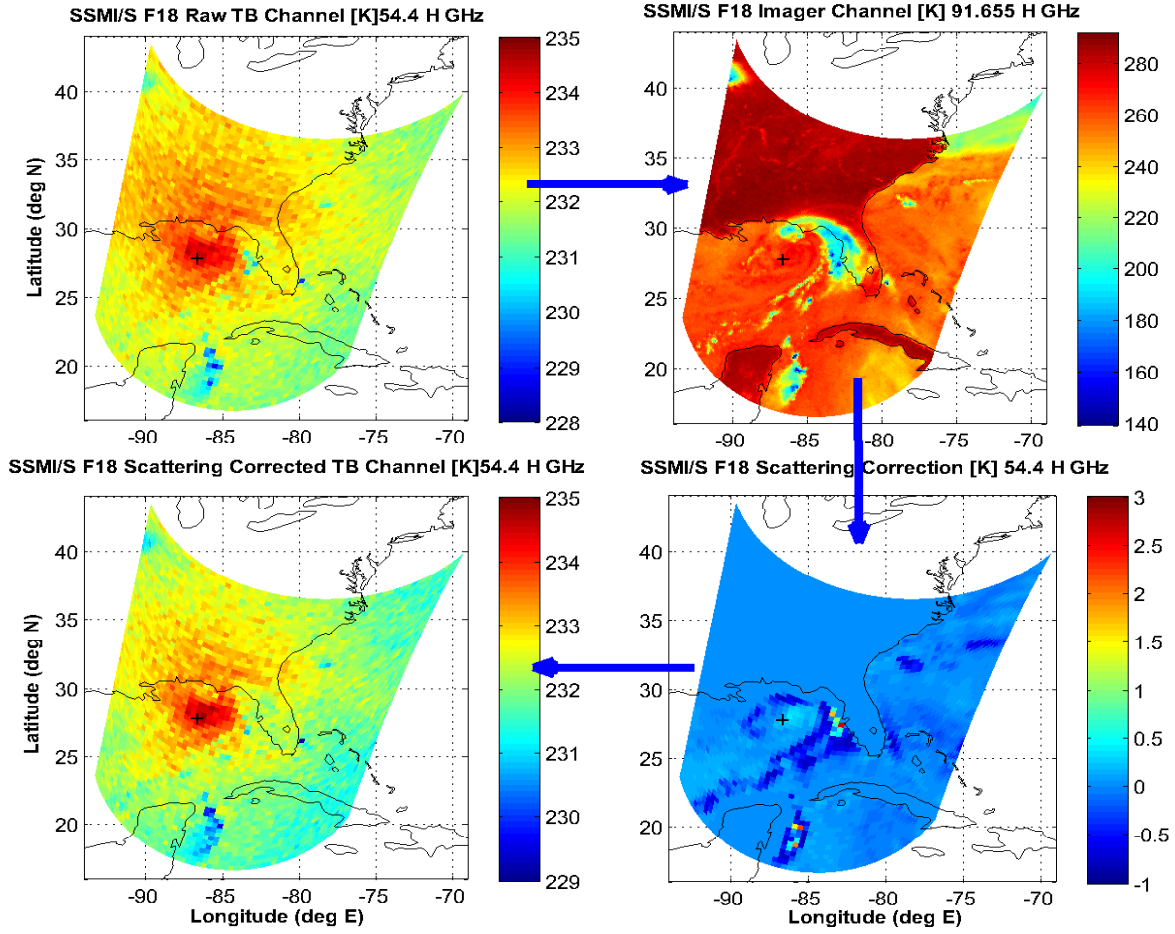
**Figure 26. Scattering Correction Sequence. The raw brightness temperatures (top left) are corrected using a statistical algorithm to find the correlation between the scattering signatures (top right) and their influence on the sounding channels. A brightness temperature depression is derived to compensate for scattering (bottom right), and applied to the sounding channel (bottom left). The end result is a slightly warmer TC core with slightly more noise**

Figure 26 shows the scattering correction process. The raw sounding brightness temperatures (top left) and the time matched high frequency imager channel (top right) that is highly susceptible to scattering are compared and analyze for scattering signatures. The algorithm derives the brightness temperature correction (bottom right) to apply on the sounding channel. The end result is a scattering corrected sounding channel (bottom left). The TC core in this image appears warmer as the

scattering affecting the raw sounding channel is reduced, effectively increasing the contrast between the warm anomaly and the environmental brightness temperature.

The scattering corrected sounding channels are next used to derive the scattering corrected warm core anomaly predictor. The warmest pixel in the warm core is found and then the surrounding environmental average brightness temperature is subtracted to obtain the scattering corrected warm core anomaly. Using a linear regression with the MSLP, a correlation coefficient is derived for each sounding channel of each instrument.

### 3.3.10   FOV Size Correction at Edge of Scan

The scan angle dependency of the FOV resolution introduces another necessary correction for the AMSU and ATMS instruments. The FOV toward the edge of the scanline for these two cross-track scanning instruments. Table 12 shows the difference in size of the sample area at nadir and at the edge of the scanline. This increase in area affects the brightness temperature sensed as the features in the off-nadir FOVs are averaged with more surrounding features the larger FOV area.

Table 12. ATMS and AMSU FOV size at nadir and edge of scan.

| Channel | | Nadir Resolution[km] | | Outermost FOV size [km] | | | |
| --- | --- | --- | --- | --- | --- | --- | --- |
| ATMS | AMSU | ATMS | AMSU | ATMS | AMSU | ATMS | AMSU |
| | | | | Cross-track | | Along-track | |
| 1-2 | 1-2 | 74.8 | 48.6 | 323.1 | 155.2 | 141.8 | 85.6 |
| 3-16 | 3-15 | 31.6 | 48.6 | 136.7 | 155.2 | 60 | 85.6 |
| 17-22 | | 15.8 | | 68.4 | | 30.0 | |

A 50 km diameter warm core in the outermost ATMS FOV would be averaged with the background in a 323.1 x 141.8 km area and would appear considerably cooler than the same warm core sensed at nadir at a resolution of 74.8 km. To compensate for any potential bias this introduces, a predictor was derived by subtracting 15.5 (AMSU) or 48.5 (ATMS) from the FOV position of the TC. The absolute value of this predictor and its square were both tested for correlation with the MSLP along with the other predictors.

### 3.3.11   TC Intensity Dependence on Latitude

Typically TCs form and begin their development at low latitudes and turn pole-ward near the end of their lives at near-peak intensity. This is not always the case but it can help explain TC intensity variations with latitude changes (DeMaria and Pickle 1988). TC development depends on both relative and planetary vorticity. Planetary vorticity or Coriolis effect increases with latitude and provides the storm with an ex-tra rotation term that can enhance TC rotation and help trap the latent heat needed for further intensification. Although latitude does not directly control TC intensity, there may be some residual error in MSLP estimates that correlate with latitude. Fig-ure 27 shows the 2011 NHC tracks for all storms; note the slight bias toward weaker intensity storms at lower latitudes and higher intensity storms at higher latitudes, (NHC accessed 2014a).

The TC intensity predictor analyses performed and explained in this section were designed in a way to derive predictors that compensate for each other. A predictor that does not correlate directly with the MSLP may at least explain the residual from a different predictor's correlation. That is the bases of the multivariate regression analysis. The next section explains how each predictor is used within a multivariate regression intensity estimation scheme.
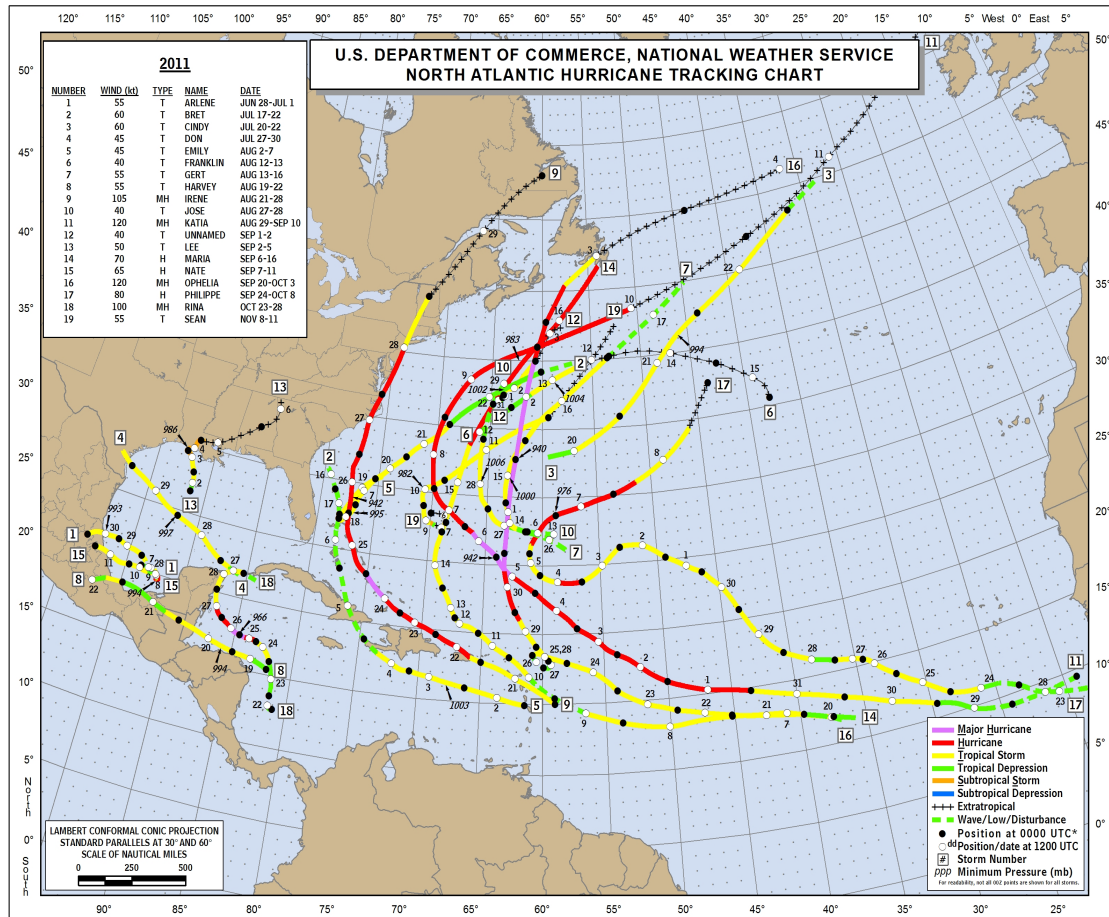
Figure 27. NOAA NHC 2011 TC Season Tracks. Stronger storms take time to develop and get organized. Notice that stronger storms take longer time to develop. All TC have a poleward movement. NHC (accessed 2014b).

## 3.4 Statistical Methods

This section discusses the statistical methods used to analyze the predictors discussed in the previous subsections. A brief overview is presented of multivariate linear regression, Root Mean Square Error (RMSE), and the cross-validation technique used to obtain the results.

### 3.4.1 Multivariate Linear Regression

The analysis portion of this research is driven by previous research that obtained positive results using the warm core anomaly as a predictor for TC MSLP. The low and high frequency channel predictors are included in this study to investigate possible correlations between passive microwave absorption and scattering signatures and TC MSLP.

For each of the predictors discussed in Section 3.3.5 simple linear regressions were computed. The linear regression estimate $\hat{y}$ is obtained by fitting (in this case) a least-square line to a scatter plot of the predicted variable. The slope of the line, $b$, represents the correlation between the predictor and the predictand (MSLP). The residuals ($e$) are computed for each point in the scatter plot and represent the distance from the fitted regression line to the predicted data points:

$$\hat{y} = b_o + bx \tag{18}$$

$$e_i = y_i - \hat{y}(x_i) \tag{19}$$

Combining equations 18 and 19 yields the regression equation which expresses the true value of the predictand as the sum of the predicted values (18) and the residuals (19):

$$y_i = \hat{y}_i + e_i = b_o + bx_i + e_i \tag{20}$$

Multivariate linear regression is an extension to simple linear regression. Instead of using a single predictor, an entire set of predictors can be used to find a regression equation that best fits all the data. Quadratic terms can be applied to each regression coefficient to tighten up the residuals. In this analysis the square of some predictors is used and proved to be better predictors than the linear predictors.

$$\hat{y} = b_o + b_1 x_1 + b_2 x_2 + ... + b_K x_K \tag{21}$$

$$\hat{y} = b_o + b_1 x_1 + b_2 x_1^2 + b_K x_K + b_K x_K^2 \tag{22}$$

In matrix form:

$$y = Xb + e \tag{23}$$

$$\hat{y} = \begin{bmatrix} \hat{y_1} \\ \hat{y_2} \\ . \\ . \\ \hat{y_n} \end{bmatrix} X = \begin{bmatrix} 1 & x_{11} & x_{12} & \cdot & x_{1n} \\ 1 & x_{21} & x_{22} & \cdot & x_{2n} \\ 1 & . & . & . & . \\ 1 & . & . & . & . \\ 1 & x_{n1} & x_{n2} & \cdot & x_{nn} \end{bmatrix} b = \begin{bmatrix} b_o \\ b_1 \\ . \\ . \\ b_n \end{bmatrix} \text{ and } e = \begin{bmatrix} e_1 \\ e_2 \\ . \\ . \\ e_n \end{bmatrix} \tag{24}$$

$$\hat{b} = (X'X)^{-1}X'y \tag{25}$$

$$\hat{y} = X\hat{b} \tag{26}$$

Equation 22 represents the best fit line to each of the predictors $(x)$, where each predictor has a respective regression coefficient and squared predictor. Fitting the data with all the predictors is not necessarily the best way to achieve the best cor-

relation coefficient. A careful selection of the predictors can increase the correlation coefficient and decrease the residuals. The order in which the predictors are used is important as well and is taken into account in the model presented next (Von Storch and Zwiers 1999), Wilks (2006).

### 3.4.2 Forward Selection Model

In order to optimize the results, careful analysis of the predictors must be accomplished. Forward selection is performed to analyze and derive the multivariate linear regression coefficients in the training data set. For this procedure four steps are performed:

- Compute simple linear regressions for each predictor. The predictor with the greatest regression coefficient is used as initial predictor in the model.

- Among the remaining predictors, find the one best correlated with the residuals from the initial predictor.

- Test the hypothesis that the inclusion of the second predictor does not significantly reduce the correlation coefficient.

- Repeat steps two and three if the inclusion of the second best predictor does increases the correlation coefficient significantly. Stop if the regression coefficient does not significantly improve.

The resultant regression coefficients are used to compute the RMSE between the predictand and the observations in the validation data set.

### 3.4.3 Root Mean Square Error

RMSE computes the average distance between the predicted MSLP and the observed MSLP in the data set. The distance computed represents the error between

the regression line and the actual observation. The RMSE provides a measure of confidence for the regression and evaluates the significance of the model by using a single average of the aggregate error which represents the predictive ability of the model. RMSE is computed using the following expression:

$$RMSE = \sqrt{\frac{1}{n}\sum_{i=1}^{n}(\hat{y}_i - y_i)^2} \tag{27}$$

For each of the instruments the RMSE is computed using the validation data set, then the RMSEs are objectively compared against each other. Lower RMSE values indicate higher accuracy.

## 3.5   Validation

This study employed a cross-validation method: All the predictors were carefully chosen and tested in the testing data set. The computation of the linear regression coefficients took place in the training data set. The validation set was used to apply the regression coefficients and compute the RMSE for each of the instruments.

By performing a cross validation, any dependence of the regression coefficient on the training data is minimized. The results are flexible enough to work on other data samples and yield reliable results representative of a diverse data sample (Wilks 2006).

# IV.  Analysis and Results

## 4.1    Chapter Overview

The analysis portion of this study consisted of evaluating the different predictors chosen and deriving their regression coefficients. The step wise regression equations derived for each instrument and its specific coefficients are presented and analyzed. Finally, the RMSE results are compared and discussed.

## 4.2    Intensity Predictor Analysis

Different intensity predictors are tested to evaluate and predict TC intensity using linear regressions vs the MSLP. These predictors were derived based on analysis of the testing data set.  The most promising predictors were selected for use in the training data set based on their success in the testing data set, how they physically relate to TC intensity estimation, and instrument specifications. Selected predictors are used to derive the regression equations in the training data set using a stepwise multiple regression. Table 13 shows the number of predictors used in the multivariate regression algorithm for each of the instruments.

**Table 13.  Number of predictors per satellite**

| Instrument | Predictors Analyzed |
| --- | --- |
| AMSU | 48 |
| ATMS | 52 |
| SSMI/S | 94 |

The reason for the larger number of predictors analyzed in the SSMI/S case is its large number of low frequency channels and its dual polarized imaging channels.

66

The regression equations derived for each instrument are presented next. Different numbers of predictors were used for each instrument determined by the incremental performance improvement provided by each predictor. The regression equations were derived using the training data set, then the validation data set was used to compare the performance of each instrument in terms of the RMSE of their MSLP estimates.

### 4.2.1 AMSU Analysis

AMSU's regression algorithm chose a sounding channel warm anomaly and FOV size predictor for the first and second iteration, while the third predictor takes into account precipitation and ice particle scattering. The three predictors chosen complement each other, and their sequence allows for an increase in the correlation coefficient after each iteration. The RMSE also decreases after each iteration but not at the same rate that the correlation coefficient increased. Figure 28 shows the regression line with the correlation coefficients and the RMSEs for each of the regression iterations.

Equation 28 shows the regression coefficients derived for the AMSU instrument. The predictors chosen are listed in Table 14, along with the relative contribution of each to the AMSU estimates. These relative contributions were computed by multiplying the regression coefficients by the standard deviation of each predictor.

$$
\begin{aligned}
MSLP = 1017.4mb &+ (-12.610mb/K \cdot Predictor_1) + \\
(-0.0322mb \cdot Predictor_2) &+ (-0.1462mb/K \cdot Predictor_3)
\end{aligned}
\tag{28}
$$
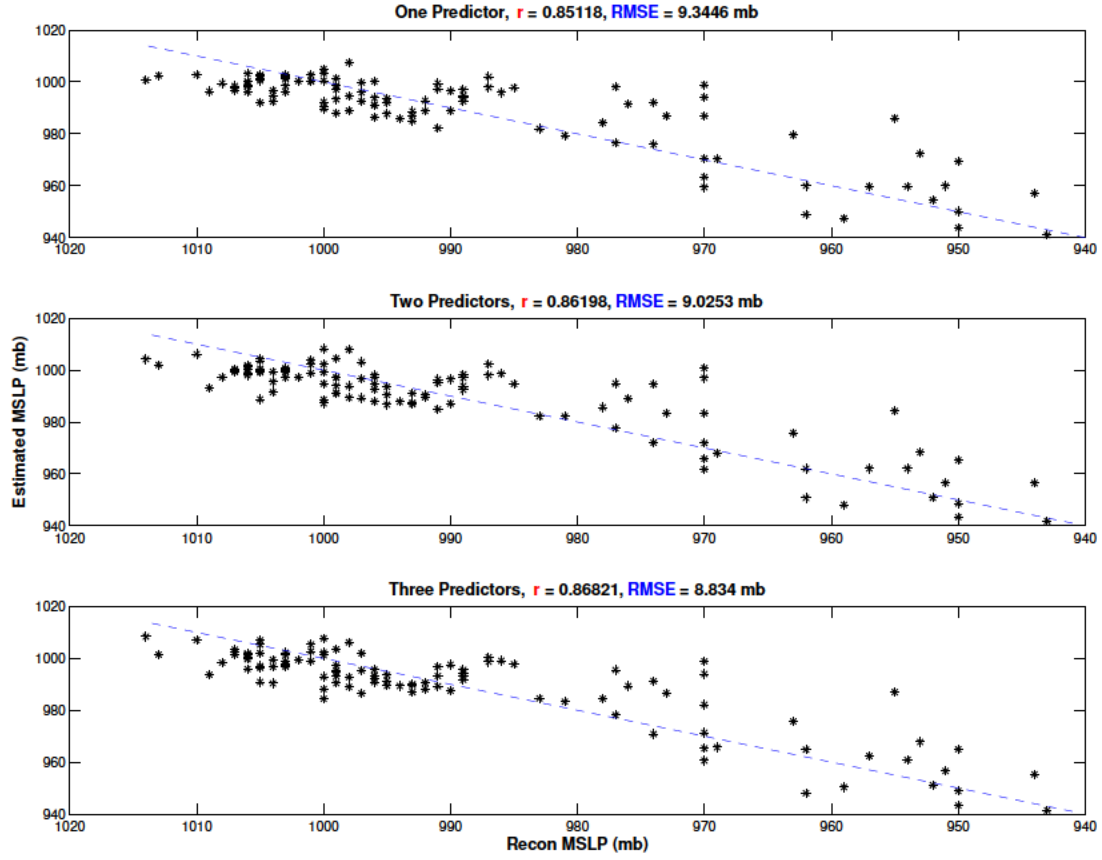
**Figure 28. Results for the three iterations performed on the AMSU training set. The regression coefficients and RMSEs get better after each iteration.**

**Table 14. AMSU regression equation predictors**

|               | Predictors                                                          | Std Dev  | Contribution [mb] |
| ------------- | ------------------------------------------------------------------- | -------- | ----------------- |
| $Predictor_1$ | 54.94 GHz Warm Anomaly                                              | 1.19 K   | 15.01             |
| $Predictor_2$ | (FOVs off-nadir )$^2$                                               | 76.53    | 2.69              |
| $Predictor_3$ | Temperature Spread: 23.8 GHz Peak TB + 89 GHz Min TB                | 13.78 K  | 2.01              |

As expected, AMSU's channel 7 (54.94 GHz) warm anomaly was chosen $Predictor_1$ in (28); its correlation with MSLP was the highest in the algorithm's first iteration.

The second highest predictor correlation coefficient was the scattering corrected 54.4 GHz warm anomaly squared. Figure 29 shows both the classical warm anomaly and the scattering corrected warm anomaly correlation coefficients for AMSU channels 6, 7 and 8. These predictors were among the top 10 predictors on the first model iteration, followed closely by the square of these predictors. Previous research has shown similar results using AMSU's sounding channels, with the channel 7 warm anomaly correlating best with the MSLP. The rest of the sounding channels' warm anomaly results are good indicators of the strong correlation between the magnitude of the warm core and the TC's MSLP.
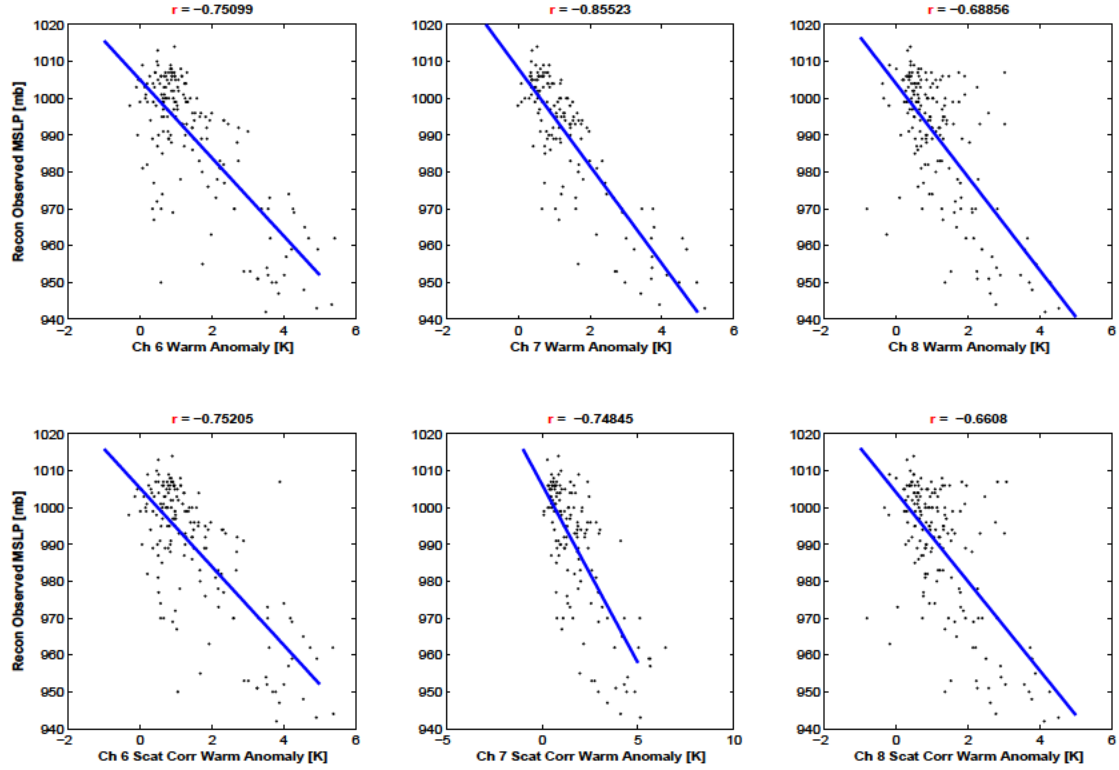


Figure 29. AMSU Sounding Channels Scatter Plot and Fitted Regression Equations. Upper Troposphere sounding channels are among the best predictors for TC intensity. These results verify previous work and validate the statistical model. Top row: raw sounding channels. Bottom row: scattering corrected sounding channels.

69

The remaining predictors chosen by the algorithm are determined by their correlation with the residuals of the prior iteration. $Predictor_2$ for AMSU is the FOV off-nadir distance squared. What this shows is that most of the residual error of the first iteration can be attributed to the scan angle dependency of the instrument, the main disadvantage for a cross-track scanning instrument. The AMSU FOV resolution increases from 48 km at nadir to 85.6 km at the edge of the scanline. This increase in FOV area reduces the sensor fidelity at the off nadir position. For the same TC warm core, the brightness temperature sensed would be cooler in an off-nadir FOV than it would be at nadir. $Predictor_2$ correlates with this error and effectively reduces the residuals from $Predictor_1$, increasing the correlation coefficient and reducing the RMSE in the algorithm. With the addition of $Predictor_2$ the algorithm decreases the errors at off-nadir angles and together, $Predictor_1$ and $Predictor_2$ provide a more accurate MSLP prediction, as seen in Figure 28 by the increase in the correlation coefficient and decrease in the RMSE after two iterations. Table 14 shows the contribution by each of the predictors. As expected $predictor_1$ contributes the most, followed by $Predictor_2$.

The third predictor chosen by the algorithm was the brightness temperature spread between AMSU channel 1 (23.8 GHz) and channel 15 (89 GHz). This predictor represents the combined effects of absorption and the upwelling radiation by precipitation and scattering of radiation by ice particles and large water drops. The predictor by itself does not correlate well with MSLP, yielding a regression coefficient of 0.35, but when used as the third predictor it reduces the RMSE by 5% and increases the correlation coefficient of the multivariate algorithm. This predictor reduced the residuals of the prior two iterations by taking into account the correlation of strong precipitation with TC intensity.

The AMSU algorithm used a sounding channel, the instrument FOV off-nadir

distance, and a composite predictor that combines precipitation effects on low and high frequency channels to derive the most accurate multivariate regression equation to predict TC intensity. Including additional predictors may increased the correlation coefficient with the training data, but further iterations could result in overfitting.

### 4.2.2 ATMS Analysis

Before starting the analysis of the ATMS regression equation and its predictors, It should be noted that the ATMS data set is considerably smaller than the AMSU and SSMI/S data sets, with less than three years operationally active and only one instrument flying; only two TC seasons were collected for this research. The analysis can be strongly biased toward outliers in the data sets due to the small sample size.

The ATMS regression equation contains interesting results. Figure 30 shows the results of each statistical algorithm iteration. Of high interest is the strong correlation coefficient and low RMSEs obtained. Equation 29 shows the regression equation and its coefficients after four iterations. Table 15 shows the predictors selected by algorithm and the contributions of each to the predictand.

$$MSLP = 1023.5mb + (-11.3280mb/K \cdot Predictor_1) +$$

$$(-5.1015 \times 10^{-7}mb/K \cdot km \cdot Predictor_2) + (-8.3678 \times 10^{-2}mb/K^2 \cdot Predictor_3) +$$

$$(-0.1509mb/K^2 \cdot Predictor_4)$$

$$(29)$$
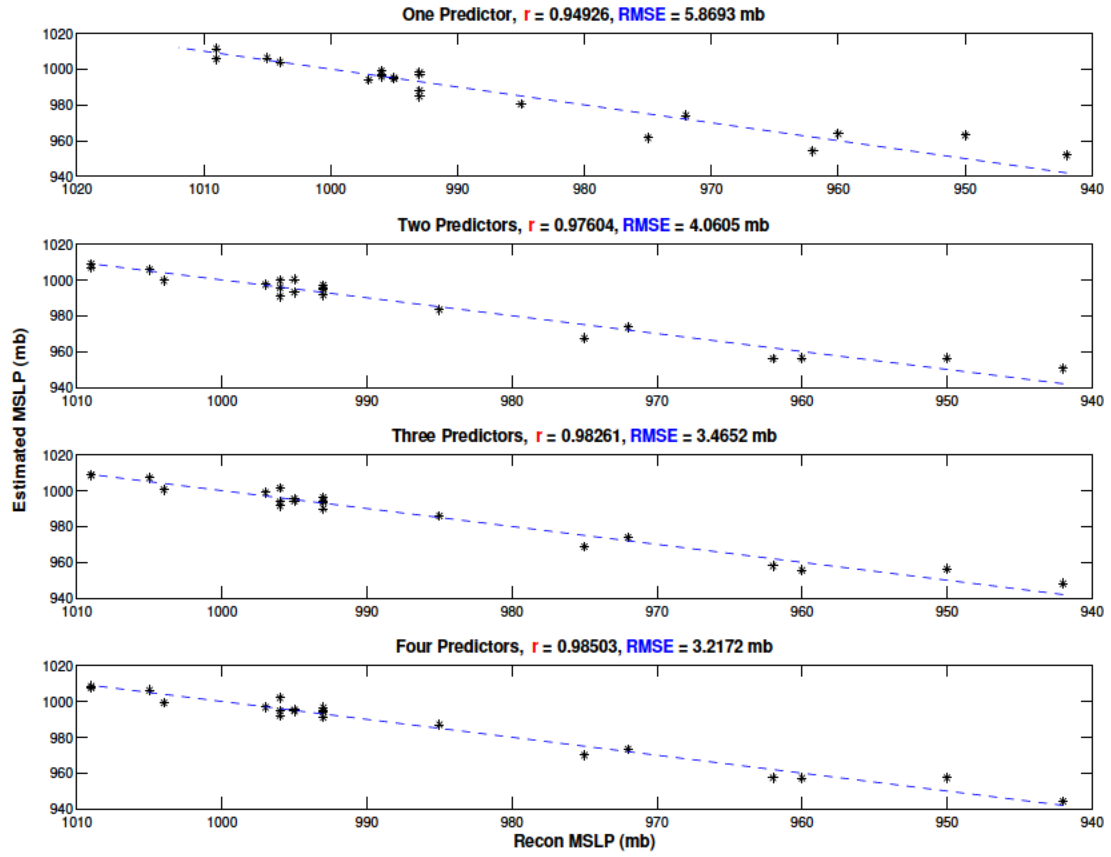
**Figure 30.** Results for the four iterations performed on the ATMS training set. The regression coefficients and RMSEs get better after each iteration.

**Table 15. ATMS regression equation predictors**

|  | Predictors | Std Dev | Contribution [mb] |
|---|---|---|---|
| $Predictor_1$ | 54.94 GHz Warm Anomaly | 1.21 K | 13.71 |
| $Predictor_2$ | 23.8 GHz Integrated Absorption | $8.91 \times 10^6$ K· km | 4.54 |
| $Predictor_3$ | 52.8 GHz Scattering Corrected (Warm Anomaly)$^2$ | 22.89 K$^2$ | 1.91 |
| $Predictor_4$ | 53.59 GHz Scattering Corrected (Warm Anomaly)$^2$ | 13.02 K$^2$ | 1.96 |

It is no surprise to see that $Predictor_1$ is the ATMS channel 8 (54.94 GHz) warm anomaly. This result is consisted with the strong correlation between warm core magnitude and MSLP. The adjacent sounding channels and their scattering corrected counterparts are also among the top 10 highest correlation coefficients on the first ATMS iteration. Only the best correlation was chosen but Figure 31 shows ATMS sounding channels 6, 7, 8 and 9 for both the raw brightness temperatures and scattering corrected brightness temperatures.
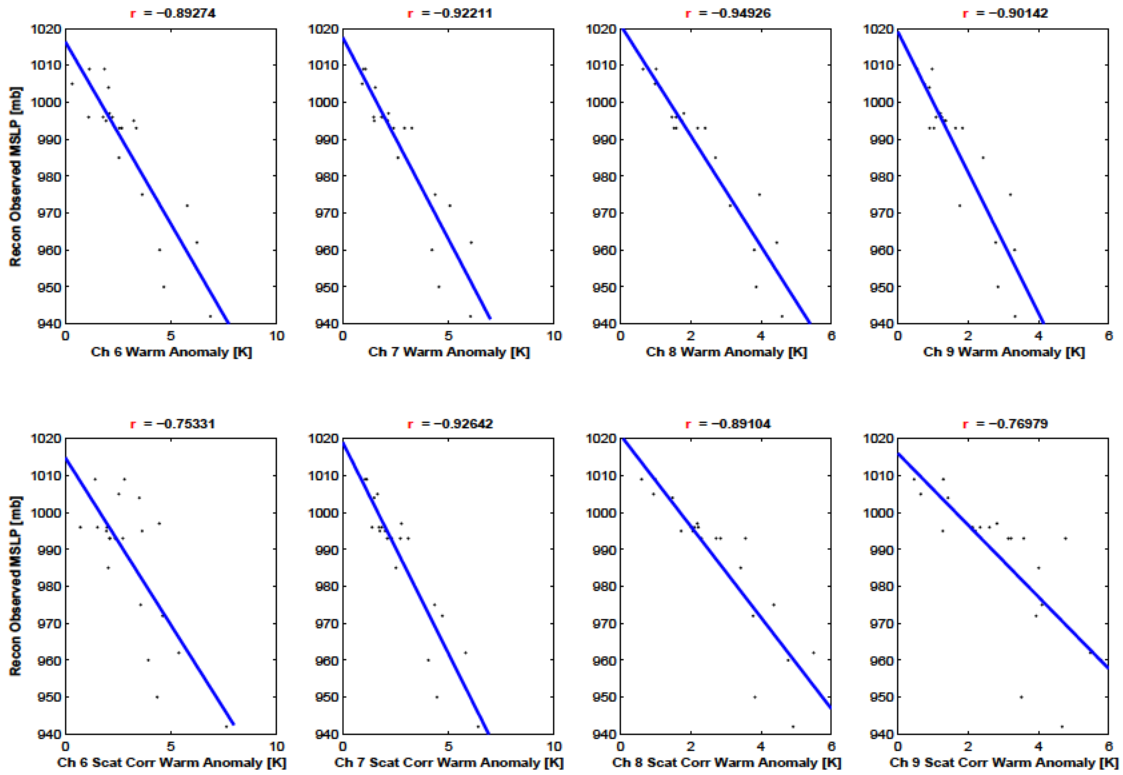


Figure 31. ATMS Sounding Channel Scatter Plot and Fitted Regression Equations. Upper Troposphere sounding channels are among the best predictors for TC intensity. Notice the similarity with the AMSU channels. Top row: raw sounding channels. Bottom row: scattering corrected sounding channels.

$Predictor_2$ is the positive brightness temperature integrated area from channel 1 (23.8GHz). This predictor measures precipitation absorption by integrating the

radial-average brightness temperature elevation from the surrounding environment, weighted by the area of the concentric ring represented by each bin. This predictor considerably increases the correlation coefficient in the second iteration and reduces the RMSE by almost 2 mb. A possible explanation for this predictor being number 2 is that the radial and azimuthal extent of heavy precipitation has a relatively good correlation with TC intensity. It is interesting to note that the FOV correction does not play a role for the ATMS which, like AMSU uses a cross-track scan strategy. A possible explanation is the higher resolution of ATMS compared to that of AMSU, which enable ATMS to resolve TC features better than the AMSU at off-nadir angles.

The third predictor chosen by the algorithm ($Predictor_3$) is the scattering-corrected warm anomaly squared for channel 5 (52.8GHz). The weighting function for this channel peaks in the lower troposphere, effectively sensing a lower level warm anomaly. Generally, lower warm anomalies are overshadowed by water vapor and precipitation absorption or scattering. Interestingly, this predictor was chosen following a predictor measuring precipitation absorption. This scattering corrected warm anomaly predictor appears to have some fidelity in sensing the warm anomaly at a lower altitude, and correct the residuals from the warm anomaly at 54.94 GHz and the brightness temperature integrated area.

$Predictor_4$ is the scattering-corrected warm anomaly squared for channel 6 (53.59 GHz). Similar to $Predictor_3$, this sounding channel's weighting function peaks lower in the troposphere. When used as a predictor by itself against MSLP, $Predictor_4$'s correlation coefficient is a respectable -0.89. However, since the algorithm does not select it until the fourth iteration its contribution to the model's correlation coefficient is relatively small, as can also be seen in Table 15.

### 4.2.3  SSMI/S Analysis

The previous two instruments, AMSU and ATMS, both have cross-track scan geometry and very similar frequencies. The SSMI/S instrument is different, with a conical scan geometry, and different resolution, and both horizontal and vertically polarized channels. The conical scanning allows the FOVs to maintain a constant resolution and uniform polarization along the scanline. The weighting functions of SSMI/S sounding channels peak at higher levels than the corresponding channels because of the 45° conical scanning angle.

The SSMI/S regression equation (30) provides interesting and unexpected results. The first two predictors selected by the algorithm are consistent with those of the ATMS, which has a similar resolution to the SSMI/S. Just as the AMSU and ATMS algorithm chose the 54.94 GHz warm anomaly as $Predictor_1$, the SSMI/S algorithm chose the 54.4 GHz warm anomaly. Figure 32 shows the results for each iteration and Table 16 lists the predictors chosen with the contribution to the predicted MSLP of each predictor.

$$
\begin{aligned}
MSLP = 1026.7mb + (-1.2673mb/K \cdot Predictor_1) + (-0.4225mb/K \cdot Predictor_2) + \\
(-2.9690mb/K \cdot Predictor_3) + (-12.3240mb/K \cdot Predictor_4) + \\
(-5.9713 \times 10^{-3}mb/K^2 \cdot Predictor_5)
\end{aligned}
$$

$$(30)$$
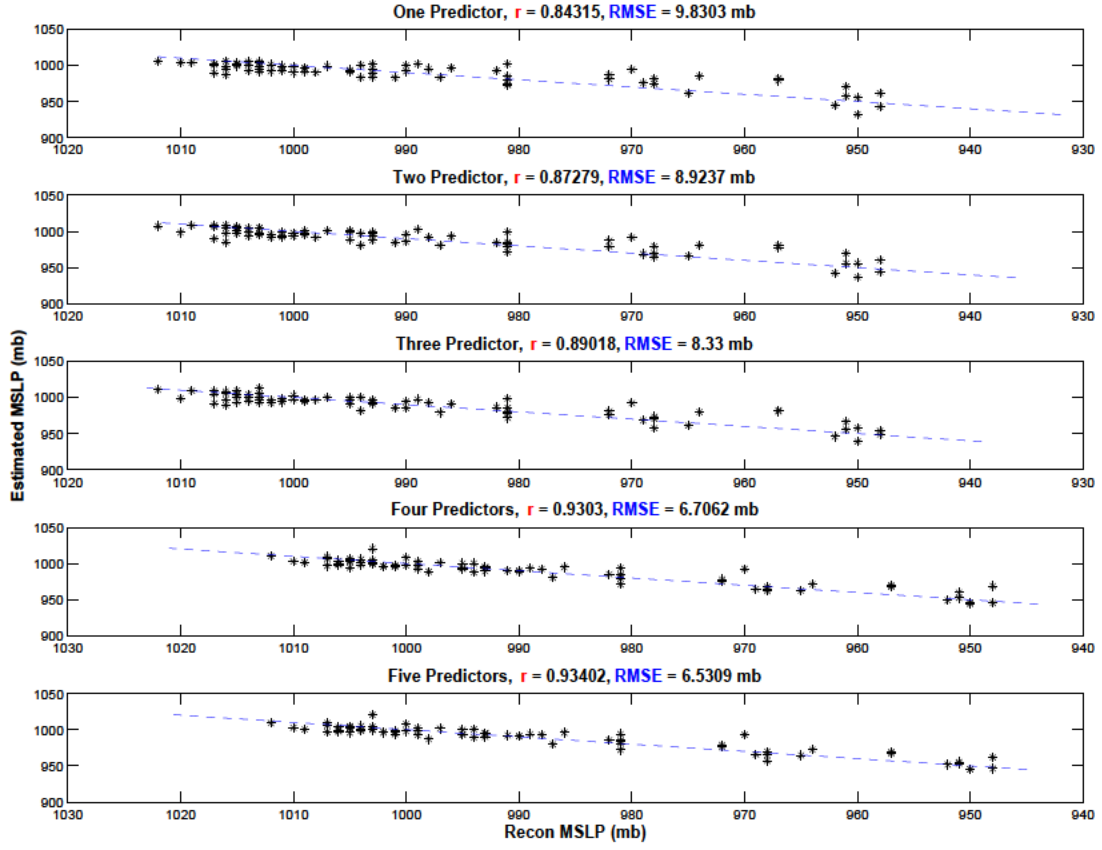
Figure 32. Results for the five iterations performed on the SSMI/S training set. The regression coefficients and RMSEs get better after each iteration.

Table 16. SSMI/S regression equation predictors

|  | Predictors | Std Dev | Contribution [mb] |
|---|---|---|---|
| $Predictor_1$ | 54.94 GHz Warm Anomaly | 1.61 K | 2.04 |
| $Predictor_2$ | 19 GHz V Absorption | 12.60 K | 5.36 |
| $Predictor_3$ | 52 GHz Warm Anomaly | 1.67 K | 4.97 |
| $Predictor_4$ | 55 GHz Warm Anomaly | 0.75 K | 9.35 |
| $Predictor_5$ | 22 GHz V (Absorption)$^2$ | 353.98 K$^2$ | 2.11 |

*Predictor₁* is the warm anomaly from the LAS channel 4 (54.4 GHz). With the 45° scan angle of the SSMI/S, one might have expected a lower frequency to better sense the warm anomaly in the upper troposphere because of the higher altitude peaks of the SSMI/S weighting function. Nevertheless, the fact that the channel 4 is the main predictor validates that SSMI/S can be used to estimate TC MSLP in a manner similar to AMSU and ATMS.

The second iteration improves the correlation coefficient significantly and drops the RMSE by almost 1 mb. $Predictor_2$ is environmental channel 2 (19 GHz V) peak absorption, providing an intensity proxy based on precipitation absorption. This predictor, as seen in Table 16, provides interestingly the second largest contribution to the predicted MSLP. The vertically polarized brightness temperature of the ocean surface is almost 20% warmer at an incidence angle of 45° than that of the horizontally polarized 19 GHz channel. Since precipitation absorption should make a more notable difference in the horizontally polarized channel brightness temperature, one might expect the 19 GHz H absorption to be a better intensity predictor than 19 GHz V. However, the correlation difference between the two channels is indicating that polarization is relatively unimportant.

$Predictor_3$ is the SSMI/S LAS channel 2 (52 GHz) warm anomaly. This channel's weighting function peaks lower in the atmosphere than the channel 4 weighting function. After five iterations $Predictor_3$ actually becomes the third highest contributor after $Predictor_4$, another warm anomaly predictor. The algorithm ultimately chose three different warm anomaly predictors that sense a spread of the atmospheric levels.

As noted earlier, $Predictor_4$ makes the largest contributions to the SSMI/S TC intensity estimation algorithm. Channel 5 (55GHz) and Channel 4 both have similar weighting functions, but channel 5 peaks higher in the troposphere or lower stratosphere. Figure 33 shows the correlation coefficients for each SSMI/S sounding channel

with MSLP. Channel 5 has less overall variability but some strong outliers. This could be the reason why it did not emerge as a predictor until late in the iteration process. As the previous iterations corrected residuals they also enhanced the predictability of MSLP by $Predictor_4$.

$Predictor_5$ is a low frequency channel (22 GHz V) absorption value squared. This indicates the algorithm is taking into account the imager channels' information about precipitation absorption, and also accounting for some of the non linear residuals. $Predictor_5$'s contribution is modest (2.11 mb), but it does continue to reduce the RMSE for SSMI/S.
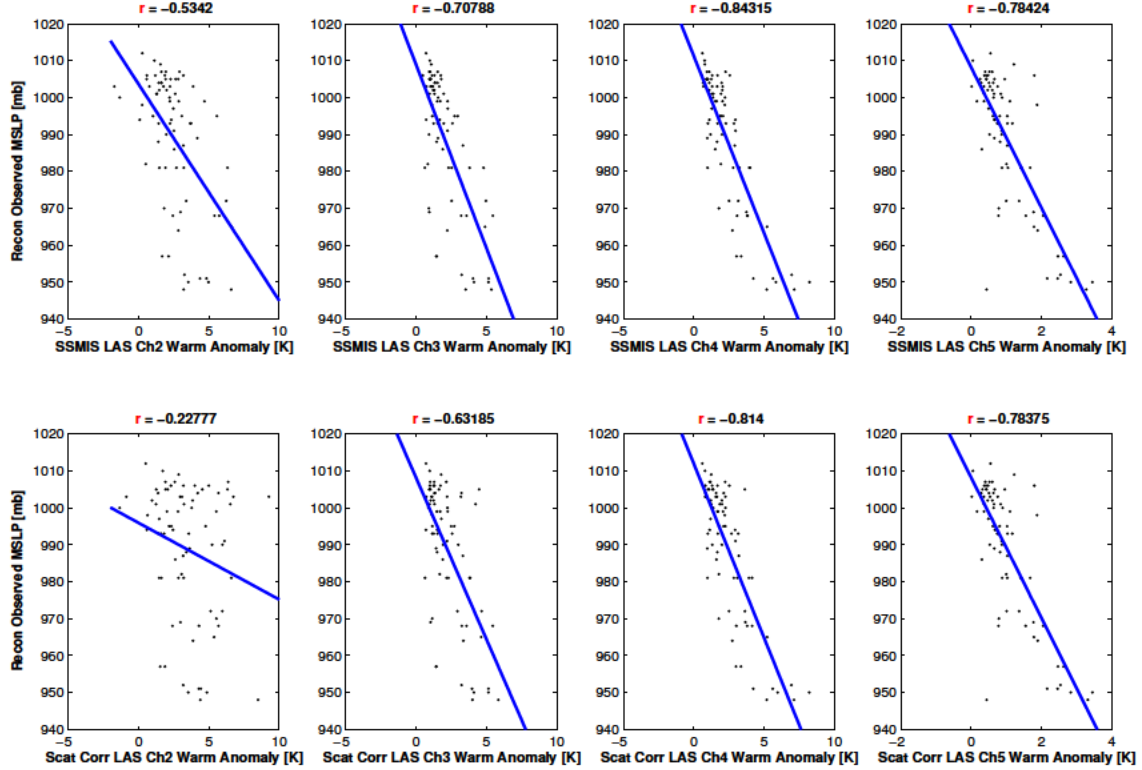


Figure 33. SSMI/S Sounding Channels Scatter Plot and Fitted Regression Equations. Upper Troposphere sounding channels are among the best SSMI/S predictors for TC intensity. Because of the conical scan geometry the channels' weighting functions differ from the AMSU and ATMS instruments. Top row: raw sounding channels. Bottom row: scattering corrected sounding channels.

## 4.3 Analysis Review

The main predictor for all three instruments is the warm anomaly at the 54.94 GHz channel for ATMS and AMSU, and the 55 GHz channel for the SSMI/S. Subsequent iterations increased the model's correlation coefficient and lowered the RMSE for each of the instruments. The addition of imager channels predictors increased the correlation coefficient and decreased the RMSE for all three instruments.

Sounding channel results were presented for all three instruments as their correlation coefficients were considerably higher than any other predictor on the first iteration. This result confirms the strong correlation between the classical warm anomaly (or scattering-corrected warm anomaly) in the upper troposphere and TC MSLP. The next section focuses on the RMSE results obtained after applying the regression coefficients derived in the training data set to the validation data set.

## 4.4 Validation Results

The regression coefficients from equations (28), (29) and (30) were all applied to predictors from the validation data set. A correlation coefficient and RMSE were obtained for each instrument. We expect RMSE results for the validation data set not to be as good as for the training data results due to possible overfitting of the regression relation to the training data.

Each instrument's results are presented with both a regression plot and a normalized residual plot. The scatter plot helps to visualize the multiple regression's ability to fit the data. The normalized residual scatter plot in the lower portion of the figure has vertical dividing lines indicating the different TC intensity categories. The RMSE is represented by dashed horizontal red lines and the normalized fitted line is blue. Both plots can be used together to assess how well the regression relation fits the observed TC intensities.

### 4.4.1 SSMI/S

The SSMI/S showed a correlation coefficient of 0.93 and 6.5 mb RMSE in the training data using 5 predictors. This equation, when used with the validation data set, yielded a correlation coefficient of 0.89 and RMSE of 7.7 mb. Figure 34 depicts the scatter plot of estimated MSLP vs observed MSLP. The normalized regression equation and its residuals are shown at the bottom of the figure. The data set is heavily influenced by the higher number TD and TS. The number of strong storms is relatively low. This observation is important to note because of the chosen predictors for the SSMI/S instrument and their specific response to TC dynamics. A strong warm anomaly is not expected to develop until after the transition from TS to HU, based on results from Velden and Smith (1982), but precipitation scenes are abundant during TD and TS. Thus the abundance of TD and TS cases in the training data set may have biased the set of predictors chosen toward the absorption channels.

The fraction of storms within the RMSE is higher in the TS and HU phase than in the TD phase. There are two possible explanations for this observation. The first is the higher number of TS relative to TDs or HUs, which may bias the algorithm toward predictors that perform best in that category. The second explanation is the maturity of the warm anomaly. A more pronounced warm anomaly may lower the RMSE and provide a more accurate MSLP estimate for strong storms. Both explanations may contribute to the overall result, but the fact that the warm anomaly is the number one predictor likely explains the better performance of the SSMI/S algorithm for TS and HU. The second best predictor was the 19 GHz precipitation absorption. This predictor considerably increased the correlation coefficient and potentially helps explain the higher confidence of the algorithm for TS. At this stage of the TC, precipitation occurs in most of the instrument FOVs near storm center. Absorption is more prevalent, while scattering effects are not well established yet. Thus the low frequency

response to TC intensity is higher and compensates for a weak warm anomaly or the lack of one.
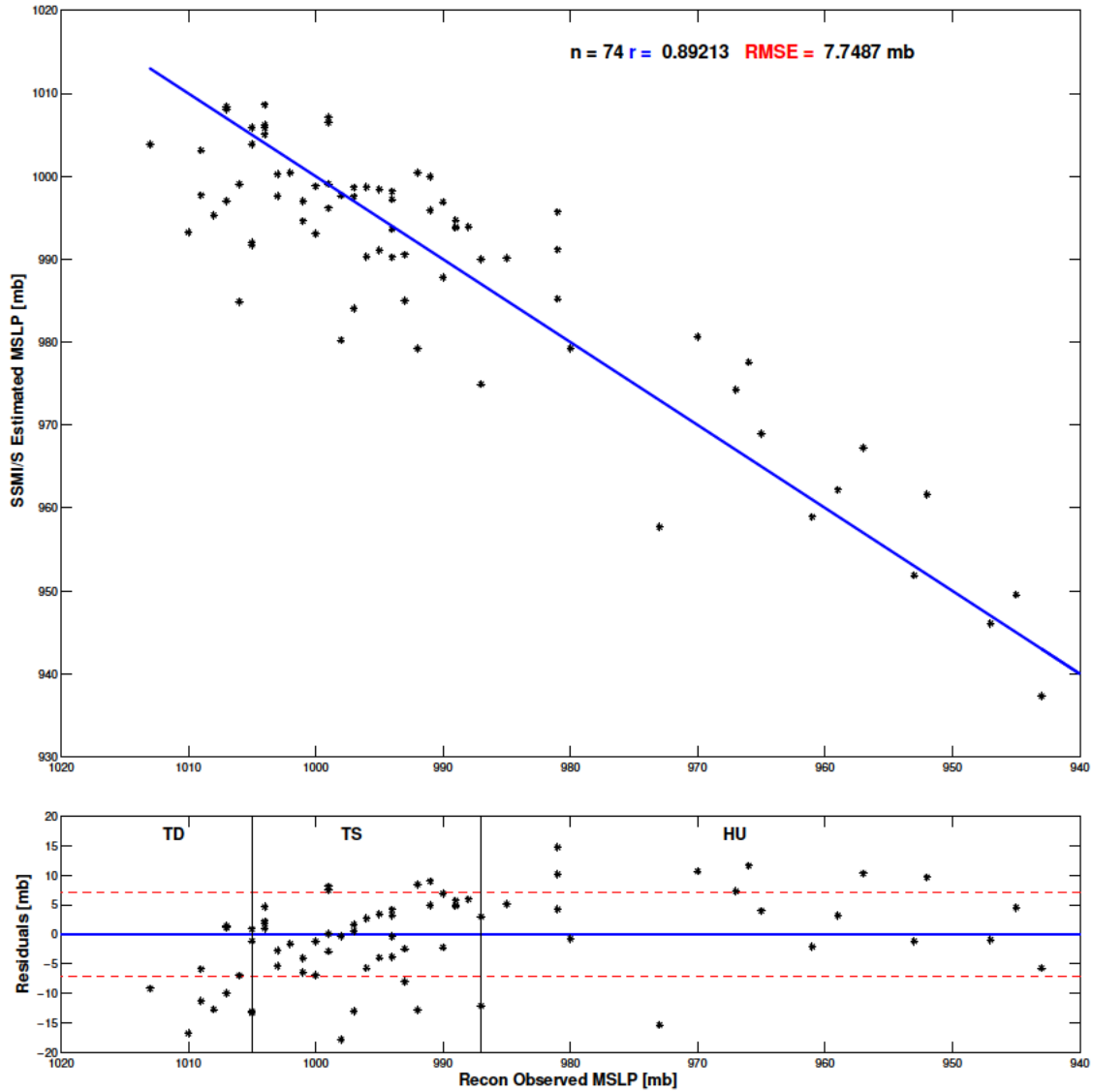


Figure 34. SSMI/S Validation Results. Scatter plot (top) shows the validation set regression equation results for the SSMI/S. The normalized residual plot (bottom) represents the models prediction confidence per storm category; red dashed lines represent the RMSE.

### 4.4.2  ATMS

The ATMS is the newest of the three instruments and its limited sample size impacted the validation results. The training set regression results were good, with a correlation coefficient of 0.98 and RMSE of 3.2 mb. However, predictors from the validation data set with the regression equation from the training data set, a noticeable decrease in the correlation coefficient takes place. The validation data set yields a correlation of 0.73 and RMSE of 12.8 mb. Figure 35 shows the scatter plot and the residual plot for the ATMS. The first thing to note is the poor result for HU intensity TCs and small data set.

The ATMS results are somewhat consistent with the SSMI/S for weak TCs; most of these storms (TD and TS) fall within the RMSE values. Given the better results obtained in the training data set, possible explanations for the poor validation results are overfitting the training data or corrupted files which yield strong outliers. Regardless, the small sample of cases available from the ATMS negatively affected the results.

### 4.4.3  AMSU

The AMSU training data set produced a correlation coefficient of 0.86 and an RMSE of 8.8 mb, which are consistent with previous results of Kidder et al. (1978) and Velden and Smith (1982) where correlation coefficients in the 0.90 range and RMSEs as low as 6.0 mb were found. The validation set in this study resulted in a correlation coefficient of 0.86 and RMSE of 9.3 mb. Regression and residual plots are shown in Figure 36.

The correlation coefficient obtained in this study does not improve on previous results, but does shows consistent intensity estimation quality across all TC stages. Even though the results did not improve, this study was able to demonstrate corre-

lation coefficient increase with the addition of the imager channels. AMSU results are consistent with the other two instruments in that higher prediction confidence is observed for low intensity TCs, especially TSs. The same reasoning provided for the SSMI/S is valid for the AMSU; the sample size is greater for TD and TS categories. The warm anomaly predictor performs better as the TC develops and gains intensity.



Figure 35. ATMS Validation Results. Scatter plot (top) shows the validation set regression equation results for the ATMS. The normalized residual plot (bottom) represents the models prediction confidence per storm category; red dashed lines represent the RMSE.
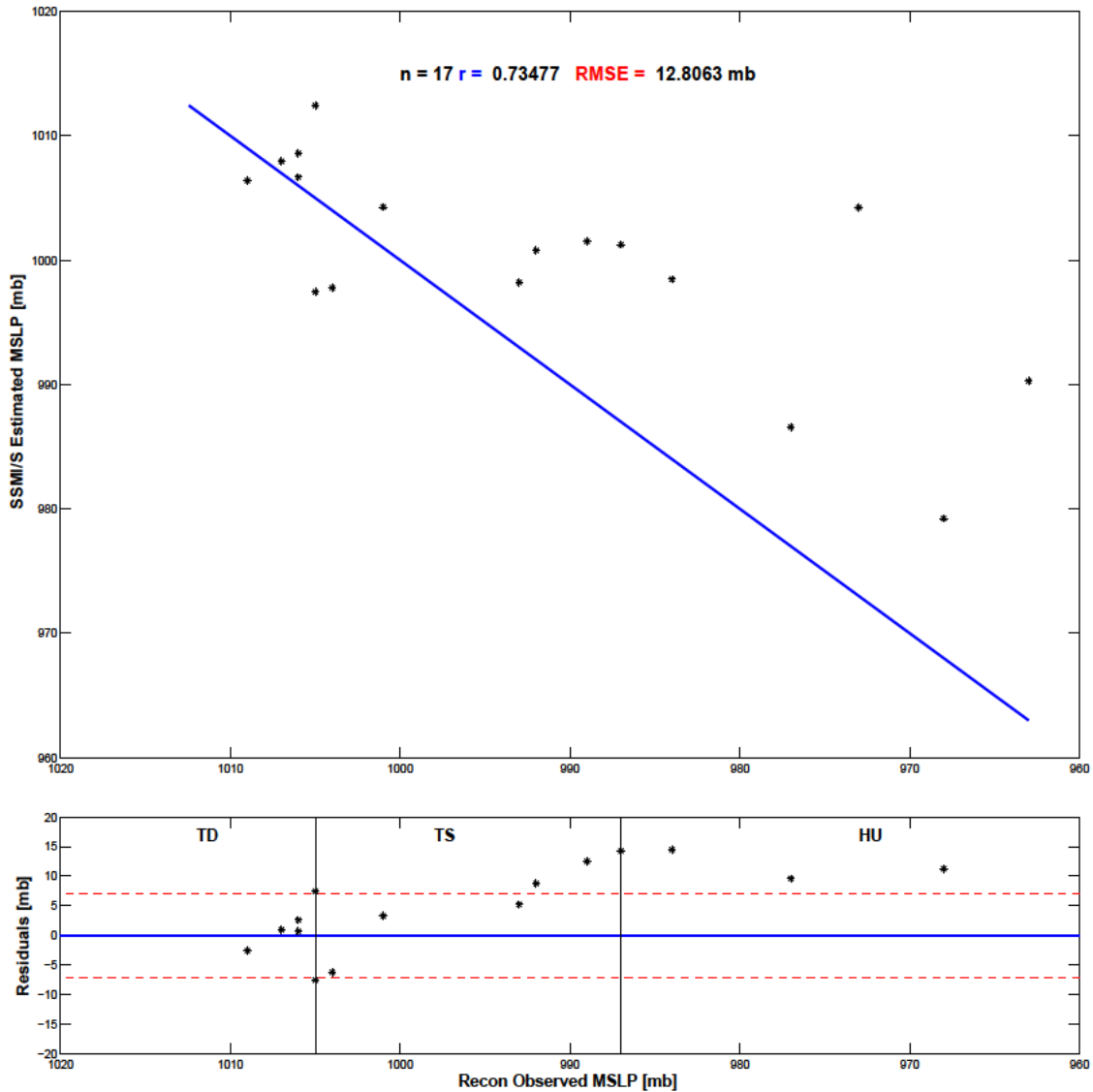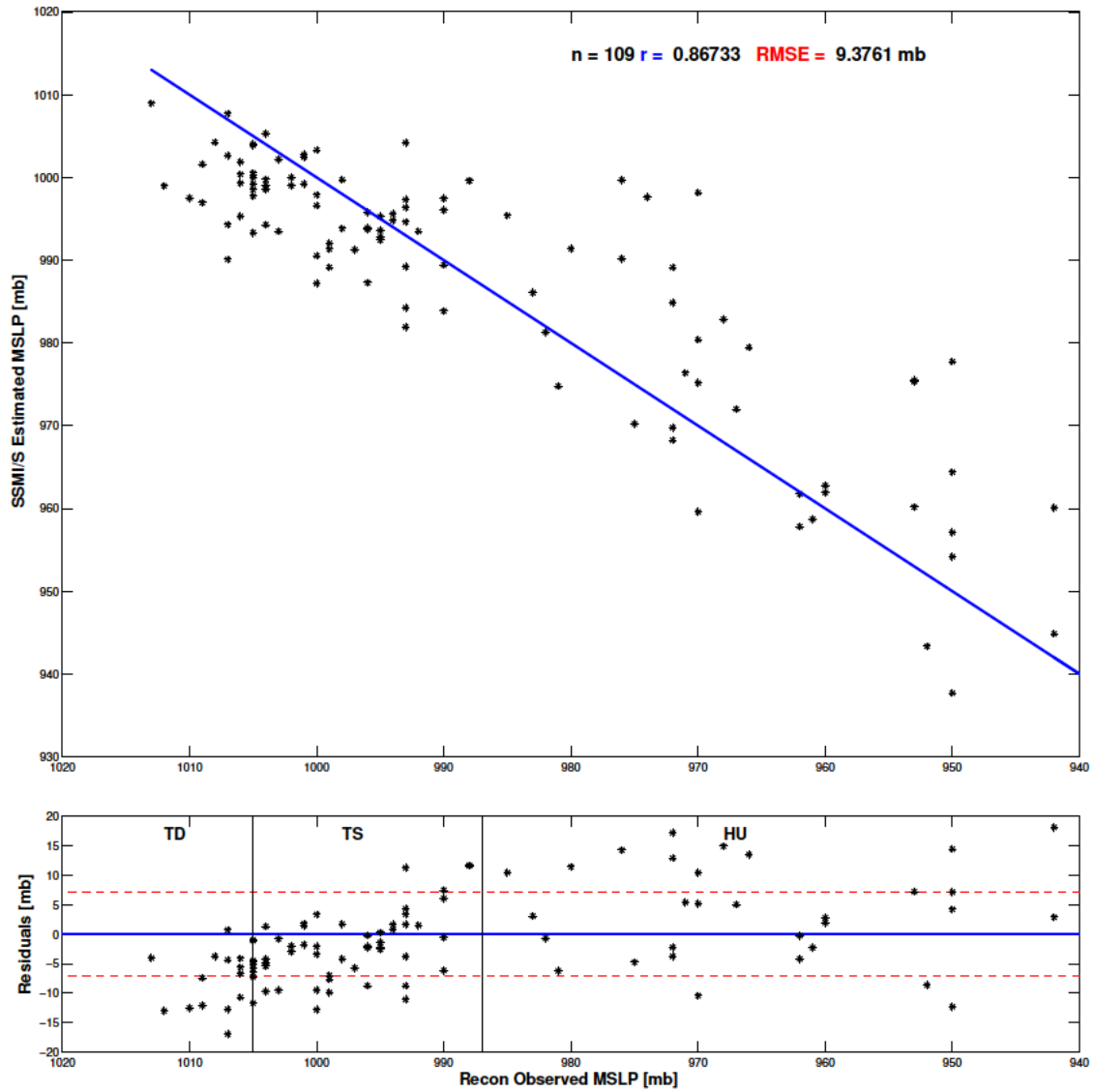
83

Figure 36.   AMSU Validation Results.   Scatter plot (top) shows the validation set regression equation results for the AMSU. The normalized residual plot (bottom) represents the models prediction confidence per storm category; red dashed lines represent the RMSE.

## 4.5    Results Review

The SSMI/S estimated TC intensity with the best RMSE, 7.7 mb. AMSU and ATMS followed with 9.3 mb and 12.8 mb, respectively. The analysis of the regression plots and corresponding residual plots for all three instruments showed instrument tendencies at different TC categories. The SSMI/S showed more prediction consistency throughout all stages of TC development, while the other two instruments showed large residuals for high intensity TCs. In general, the SSMI/S provided better results for TC intensity estimation using this algorithm.

The results are somewhat surprising in light of the fact that two of the three SSMI/S instruments on orbit are producing degraded data due to sensor problems. The ATMS results are considerably affected by the limited data sample, which is believed to have affected its regression coefficient and RMSE in the validation. Strong outliers in the HU category need further investigation to provide an explanation for the large difference between the training and validation data set.

# V. Conclusion

## 5.1 Chapter Overview

This chapter presents a summary of this research and recommendations for future work. Section 5.2 summarizes the conclusions of the analysis. Section 5.3 provides recommendations for further research on this topic.

## 5.2 Summary

Two important considerations affected the SSMI/S and ATMS results. First, DMSP F16 and F17 are both experiencing operational issues with their SSMI/S microwave radiometers and second, the sample size for the ATMS was limited. Both DMSP F16 and F17 are currently experiencing SSMI/S problems that affect their brightness temperatures. The brightness temperature deviation from the actual brightness temperature is believe to be consistent across the channels and scanlines, so in an attempt to correct for this error, a brightness temperature correction is added to bad channels, essentially correcting the error. The ATMS has been operational for a little over three years, with only 2 full TC seasons completed. The small sample size of ATMS observations affected the results negatively by under-fitting the model, creating a strong bias toward the regression equation's native data sample.

### 5.2.1 Predictor Analysis

The intensity predictors used were selected based on passive microwave frequency response to TC physical properties. In addition to using the classical warm anomaly at the 55 GHz, as has been used since the emergence of the MSU by Kidder et al. (1978), other predictors were tested, analyzed, and derived using the entire spectrum of the instruments microwave channels. The response of a given channel to water vapor

absorption, precipitation absorption, and scattering associated with ice particles or larger water drops, all were taken into account to derive over 200 individual predictors to estimate TC intensity. Instruments field of view geometry effects were included as predictors as well. Also, atmospheric contributions (ice particles) added noise to sounding channels via scattering, and using a precipitation correction technique used by Wacker (2005), these channels were corrected.

The AMSU, SSMI/S, and ATMS predictors derived from low and high frequency channels helped to improve the correlation coefficient and RMSE achieved using only the upper tropospheric warm anomaly. The SSMI/S and ATMS instruments benefited the most from these predictors as their second regression predictors were the low frequency absorption and the integrated absorption, respectively. In the case of the AMSU, the second predictor was the FOV correction squared, followed by the brightness temperature spread between the absorption and scattering signatures.

Even though the best performing predictor for each instrument was the upper troposphere sounding channel, the addition of the low and high frequency channels improve the estimate accuracy. The results show higher accuracy for TD and TS either because of dynamic or structure difference in weaker storms or because there is a smaller range of MSLP in these categories.

Not all the predictors performed as the theory suggested or provided useful information to estimate TC intensity. However, the statistical algorithm used is designed to test all the predictors and utilize the predictors that increase the accuracy of the regression equation by iterating to minimize the residuals and decrease the RMSE.

### 5.2.2  Statistical Algorithm

The statistical method used is multivariate regression using a stepwise forward model. The multivariate regression allowed the usage of all the predictors found

and fitted a regression equation on the data to estimate a predictand, in this case the MSLP. The stepwise forward model finds the best predictor, then reduces the regression's residuals by iteratively finding predictors with the highest correlation to the residuals.

The algorithm confirmed previous research by selecting the 55 GHz warm anomaly as the best predictor for all three instruments on the first iteration. These channels' weighting functions peak at approximately 200 mb and most accurately measure the UTWA that is known to be highly correlated with TC MSLP. The rest of the predictors selected by the algorithm in subsequent iterations effectively increased the correlation coefficients for all three instruments. The addition of the low frequency and high frequency derived predictors proved to increase the accuracy of the regression equation by decreasing the RMSE. This Algorithm does not consider any physical relation in the sequence of predictors; predictors are chosen based on correlation and do not provide a physical reason for their rank within the algorithm. This does not necessarily negate the physical background behind the predictors since iterations converge rapidly to the best few predictors.

Since regression is susceptible to overfitting to the training data set, the correlation coefficients and RMSE found for the training data sets were better than the results found during validation on a different data set using the training regression coefficients. When comparing values from training results (Figures 28, 30, and 32) with their respective validation results (Figures 34, 35 and 36), one can see the lower RMSE and higher correlation coefficients on the training results. The ATMS instrument was the most affected by the cross-validation with possible explanations attributed to outlier storms and the small sample size.

### 5.2.3 Comparison of Results

TC intensity estimates derived from the SSMI/S and the ATMS have shown to be comparable to AMSU derived estimates. The addition of predictors derived from low and high frequency channels and instruments FOV geometry increase intensity estimation accuracy by 10% for the SSMI/S, 3% for the AMSU and 4% for the ATMS, based on a first iteration using only the classical warm anomaly as a predictor. Despite the uncertainties in the SSMI/S instruments regarding the sensor issues and the small sample size of the ATMS, their results are promising and are valid candidates for further research in this topic.

### 5.3 Recommended Future Work

This study has shown interesting results using passive microwave radiometers and exploiting low and high frequency channels to characterize TC intensity. As previously mentioned, more work in this topic can further the research and better the results. The ATMS is a fairly new instrument and its results were affected by the small sample data size. Adding additional TC seasons to the ATMS data set would increase confidence in its regression equation and minimize the strong bias towards the training data set. The work does not have to be limited to the Atlantic ocean basin. The addition of the other ocean basins would increased the sample data size, not only of the ATMS, but for the AMSU and SSMI/S as well. A case by case study of the outliers affecting the regression equations, especially in the AMSU and ATMS cases which showed large residuals in TCs with low MSLPs, would help explained the large errors. Further research can also be done to evaluate an absorption/scattering-only technique for conical-scanning imaging instruments like the Advanced Microwave Scanning Radiometer (AMSR-2). Finally, automating the algorithm and operational implementation would be the desired end-state of this research.

# References

Air Force Weather Agency, accessed 2014: Joint Typhoon Warning Center Marks 50 Years of Service. [Available online at http://www.afweather.af.mil/news/story. asp?id=123177909].

Bell, W., S. English, B. Candy, F. Hilton, S. Swadley, and G. Kelly, 2006: An initial evaluation of ssmis radiances for radiance assimilation applications. *IEEE Micro-Rad, 2006*, 207–211, doi:10.1109/MICRAD.2006.1677090.

Blake, S. E., C. W. Landsea, and E. J. Gibney, 2011: The deadliest, costliest, and most intense united states tropical cyclones from 1851 to 2010 (and other frequently requested hurricane facts). [ noaa thechnical memorandum nws nh-6], 49 pp.

Brueske, K. F., and C. S. Velden, 2003: Satellite based tropical cyclone intensity estimation using the noaa-klm series advanced microwave sounding unit (amsu). *Mon. Wea. Rev.*, **131**, 687–697.

CLASS, accessed 2014: NOAA Comprehensive Large Array-Data Stewardship System website. [Available online at http://www.nsof.class.noaa.gov/saa/products/ welcome].

Cooperative Institute for Research in the Atmosphere , accessed 2014: CIRA. [Available online at http://amsu.cira.colostate.edu/].

DeMaria, M., and J. D. Pickle, 1988: A simplified system of equations for simulation of tropical cyclones. *J. Atmos. Sci.*, **45**, 1542–1554.

Demuth, J. L., M. DeMaria, and J. A. Knaff, 2006: Improvement of advanced microwave sounding unit tropical cyclone intensity and size estimation algorithms. *J. Appl. Meteor. Climatol.*, **45**, 1573–1581.

Demuth, J. L., M. DeMaria, J. A. Knaff, and T. H. Vonder-Haar, 2003: Evaluation of advanced microwave sounding unit tropical-cyclone intensity and size estimation algorithms. *J. Appl. Meteor. Climatol.*, **43**, 282–296.

Emanuel, K. A., 1986: An air sea interaction theory for tropical cyclones. part i: Steady-state maintenance. *J. Atmos. Sci.*, **43**, 585–604.

Emanuel, K. A., 2003: Tropical cyclones. *Annual Review Earth Planet Science*, **31**, 75–104.

Frank, W. M., and P. E. Roundy, 2006: The role of tropical waves in tropical cyclogenesis. *Mon. Wea. Rev.*, **134**, 2397–2417.

Goldberg, M. D., D. S. Crosby, and L. Zhou, 2000: The limb adjustment of amsu-a observations: Methodology and validation. *J. Appl. Meteor.*, **40**, 70–83.

Goodberlet, M. A., C. T. Swift, and J. Wilkerson, 1990: Ocean surface wind speed measurements of the special sensor microwave/imager (ssm/i). *Geoscience and Remote Sensing, IEEE Transactions on*, **28 (5)**, 823–828, doi:10.1109/36.58969.

Gunn, K. L. S., and T. W. R. East, 1954: The microwave properties of precipitation particles. *Quart. J. Roy. Meteor. Soc.*, **80**, 522–543.

Hart, R., 2006: Hurricanes: A primer on formation, structure, intensity change and frequency. Report, George C. Marshall Institute, 11 pp. [Available : http://marshall.org/wp-content/uploads/2013/08/Hart-Hurricanes-A-Primer-on-Formation-Structure-Intensity-Change-and-Frequency.pdf].

Hawkins, J. D., F. J. Turk, T. F. Lee, and K. Richardson, 2008: Observations of tropical cyclones with the special sensor microwave imager/sounder. **46**, 901–912, doi:10.1109/TGRS.2008.915753.

Holton, J. R., and G. J. Hakim, 2012: *Introduction to Dynamic Meteorology.* 5th ed., Academic Press, 552 pp.

Katsaros, K. B., L. Mitnik, and P. Black, 2014: Microwave instruments for observing tropical cyclones. *Typhoon Impact and Crisis Management*, D. L. Tang, and G. Sui, Eds., Advances in Natural and Technological Hazards Research, Vol. 40, Springer Berlin Heidelberg, 5–61, doi:10.1007/978-3-642-40695-9_2, URL http://dx.doi.org/10.1007/978-3-642-40695-9_2.

Kidder, S. Q., M. D. Goldberg, R. M. Zehr, M. DeMaria, J. F. W. Purdom, C. S. Velden, N. C. Grody, and S. J. Kuusselson, 2000: Satellite analysis of tropical cyclones using the advance microwave sounding unit (amsu). *Bull. Amer. Meteor. Soc.*, **81**, 1241–1259.

Kidder, S. Q., W. M. Gray, and T. H. Vonder Haar, 1978: Estimating tropical cyclone central pressure and outer winds from satellite microwave data. *Mon. Wea. Rev.*, **106**, 1458–1464.

Kidder, S. Q., and T. H. Vonder-Haar, 1995: *Satellite Meteorology: An Introduction.* 1st ed., Academic Press, 467 pp.

Liu, Q., and F. Weng, 2007: Uses of noaa-16 and -18 satellite measurements for verifying the limb-correction algorith. *J. Appl. Meteor. Climatol.*, **46**, 544–548, doi:10.1175/JAM2476.1.

NESDIS, accessed 2014: NOAA KLM USER's GUIDE. [Available online at http://www.nhc.noaa.gov/data/#recarch].

NHC, accessed 2014a: NOAA, National Hurricane Center. [Available online at http://www.nhc.noaa.gov/data/tracks/tracks-at-2011.png].

NHC, accessed 2014b: NOAA National Hurricane Center Data archive . [Available online at http://www.nhc.noaa.gov/data/#hurdat].

NHC, accessed 2014c: NOAA National Hurricane Center Data archive . [Available online at http://http://www.ncdc.noaa.gov/oa/pod-guide/ncdc/docs/klm/index. htm].

NRL Tropical Cyclone Page, accessed 2014: Naval Research Lab Tropical Cyclone Page. [Available online at http://www.nrlmry.navy.mil/TC.html].

Petty, G. W., 2006: *A First Course In Atmospheric Radiation*. 2nd ed., Sundog Publishing, 452 pp.

U.S. Department of Commerce, N., 2014: National hurricane center operations plan. Operations Plan FCM-P12-2014, 167 pp.

Velden, C. S., and W. L. Smith, 1982: Monitoring tropical cyclone evolution with noaa satellite microwave observations. *J. Climate Appl. Meteor.*, **22**, 714–724.

Von Storch, H., and F. W. Zwiers, 1999: *Statistical Analysis in Climate Research*. 2nd ed., Cambridge University Press, 496 pp.

Wacker, R. S., 2005: Correcting for precipitation effects in satellite-based passive microwave tropical cyclone intensity estimates. Ph.D. thesis, University of Wisconsin-Madison, 160 pp.

Wallace, J. M., and P. V. Hobbs, 2006: *Atmospheric Science, An Introductory Survey*. 2nd ed., Academic Press, 504 pp.

Weng, F., X. Zou, X. Wang, S. Yang, and M. D. Goldberg, 2012: Introduction to suomi national polar-orbiting partnership advanced technology microwave sounder for numerical weather prediction and tropical cyclone applications. *J. Geophys. Res.*, **117 (D19)**, n/a–n/a, doi:10.1029/2012JD018144, URL http://dx.doi.org/10.1029/2012JD018144.

Wilks, D. S., 2006: *Statistical Methods in the Atmospheric Sciences*. 2nd ed., Academic Press, 648 pp.

## Vita

Capt David C. Moreno was born in Houston, Texas and raised in Aguascalientes, Mexico, where he lived and went to school until he was 16 years old. He and his family emigrated to Homestead, Florida in 2001, where he graduated from South Dade Sr. High School in 2004. He then attended Miami Dade Community College, earning an Associate of Arts degree in 2007. That same year he transferred to Florida State University, where he graduated Cum-Laude with a Bachelor of Science Degree in Meteorology and a minor in Mathematics in 2009.

Capt Moreno was commissioned a Second Lieutenant in the United States Air Force after attending Office Training School at Maxwell AFB, Alabama in February 2010. His first assignment as a weather officer was to the 17th Operational Weather Squadron at Hickam AFB, Hawaii where he quickly earned certification as a weather forecaster. During his time at the 17th, he served in many leadership roles, starting as the Zone Supervisor of the North West Pacific Region, then Theater Meteorological Supervisor of the Pacific Air Forces Area of Responsibility. In his last year at the 17th, he became the Assistant Operations Flight Commander in charge of weather operations for the West Pacific region.

In November 2012 he was selected to enter the Graduate School of Engineering and Management at the Air Force Institute of Technology at Wright-Patterson AFB, Ohio, to obtain a Master's Degree in Applied Physics with a specialization in Atmospheric Science. Upon graduation, he will be assigned to the 45th Weather Squadron at Patrick AFB, FL.

## REPORT DOCUMENTATION PAGE

**Form Approved**
**OMB No. 0704–0188**

**1. REPORT DATE** *(DD–MM–YYYY)*
26–3–2015

**2. REPORT TYPE**
Master's Thesis

**3. DATES COVERED** *(From — To)*
May 2013 — Mar 2015

**4. TITLE AND SUBTITLE**

Tropical Cyclone Intensity and Position Analysis Using Passive Microwave Imager and Sounder Data

**5a. CONTRACT NUMBER**

**5b. GRANT NUMBER**

**5c. PROGRAM ELEMENT NUMBER**

**6. AUTHOR(S)**

Moreno David C., Captain, USAF

**5d. PROJECT NUMBER**

**5e. TASK NUMBER**

**5f. WORK UNIT NUMBER**

**7. PERFORMING ORGANIZATION NAME(S) AND ADDRESS(ES)**

Air Force Institute of Technology
Graduate School of Engineering and Management (AFIT/EN)
2950 Hobson Way
WPAFB OH 45433-7765

**8. PERFORMING ORGANIZATION REPORT NUMBER**

AFIT-ENP-MS-15-M-093

**9. SPONSORING / MONITORING AGENCY NAME(S) AND ADDRESS(ES)**

Joint Typhoon Warning Center
Attn: Robert J. Falvey 425 Luapele Road
Pearl Harbor, HI 96860-3103
COMM 808-474-3946, FAX 808-471-5676
Email: robert.falvey.1@us.af.mil

**10. SPONSOR/MONITOR'S ACRONYM(S)**

JTWC

**11. SPONSOR/MONITOR'S REPORT NUMBER(S)**

**12. DISTRIBUTION / AVAILABILITY STATEMENT**

DISTRIBUTION STATEMENT A:
APPROVED FOR PUBLIC RELEASE; DISTRIBUTION UNLIMITED.

**13. SUPPLEMENTARY NOTES**

This material is declared a work of the U.S. Government and is not subject to copyright protection in the United States.

**14. ABSTRACT**

Satellite based Tropical Cyclone (TC) intensity and location estimates are critical for TC warning centers and global Numerical Weather Prediction (NWP) Models due to the lack of in-situ observations of mean sea-level pressure (MSLP) and winds. Passive microwave instruments on polar-orbiting weather satellites are useful for estimating the intensity and location of TCs because upwelling microwave radiation can generally penetrate clouds. Currently, operational TC prediction centers rely on intensity estimates derived from Polar-orbiting Operational Environmental Satellite (POES) Advanced Microwave Sounding Unit (AMSU-A) brightness temperatures. This study compares the performance of a variety of TC intensity estimation techniques using both the imaging and sounding channels from AMSU-A, the Defense Meteorological Satellite Program (DMSP) Special Sensor Microwave Imager and Sounder (SSMI/S), and the Suomi-National Polar-orbiting Partnership (S-NPP) Advanced Technology Microwave Sounder (ATMS) for a sample of 28 North Atlantic storms from the 2011 through 2013 TC seasons. Using a stepwise multivariate regression statistical model the SSMI/S, AMSU and ATMS achieve correlation coefficients of 0.89, 0.86, and 0.73 respectively with TC MSLP and root mean square error (RMSE), of 7.7, 9.3 and 12.8 mb, respectively.

**15. SUBJECT TERMS**

Tropical Cyclone Intensity Estimates, SSMI/S, AMSU, ATMS, Remote Sensing, Satellite Meteorology, Tropical Meteorology, Tropical Cyclone Forecasting, Hurricanes

| 16. SECURITY CLASSIFICATION OF: | | | 17. LIMITATION OF ABSTRACT | 18. NUMBER OF PAGES | 19a. NAME OF RESPONSIBLE PERSON |
|---|---|---|---|---|---|
| a. REPORT | b. ABSTRACT | c. THIS PAGE | | | Lt Col Robert S. Wacker, AFIT/ENP |
| U | U | U | UU | 108 | 19b. TELEPHONE NUMBER *(include area code)* (937) 255-3636, x4609; robert.wacker@afit.edu |

**Standard Form 298 (Rev. 8–98)**
Prescribed by ANSI Std. Z39.18